Measurement of lifetimes for heavy flavour mesons using semileptonic *B* decays at LHCb

THÈSE N^O 8631 (2018)

PRÉSENTÉE LE 8 JUIN 2018
À LA FACULTÉ DES SCIENCES DE BASE
LABORATOIRE DE PHYSIQUE DES HAUTES ÉNERGIES 3
PROGRAMME DOCTORAL EN PHYSIQUE

ÉCOLE POLYTECHNIQUE FÉDÉRALE DE LAUSANNE

POUR L'OBTENTION DU GRADE DE DOCTEUR ÈS SCIENCES

PAR

Brice Emile MAURIN

acceptée sur proposition du jury:

Dr F. Courbin, président du jury
Prof. T. Nakada, directeur de thèse
Prof. M. Merk, rapporteur
Prof. D. Tonelli, rapporteur
Dr K. Kirch , rapporteur

ÉCOLE POLYTECHNIQUE
FÉDÉRALE DE LAUSANNE

Suisse
2018

No one knows what the future holds.
That's why its potential is infinite.
— Okabe Rintarou (Steins;Gate)

To my family, my friends and to all science lovers…

Acknowledgements

Acknowledgements

corrected parts of this thesis. Another big thanks to the jury members for interesting remarks and useful discussions.

Thanks to all old and new members of the PolyJapan committee, for the friendships and for giving me the opportunity to organise so many incredible events on the EPFL campus. A special thought to my friends in Neuchâtel and all around the world.

A large hug to my dear Shomira, who gave me more emotional support than I could have hoped for. And a final word to my parents and my sister, who have always been there for me: merci de m'avoir soutenu pendant toutes ces années. Je promets de ne pas *trop* vous déranger durant votre retraite !

Lausanne, Mars 2017   Brice

Abstract

This thesis work presents lifetime measurements of heavy-flavour mesons made with semileptonic B^0 and B_s^0 decays based on 3 fb^{-1} of data collected with the LHCb detector in proton-proton collisions at centre-of-mass energies of 7 and 8 TeV. The study of meson lifetimes is important to constrain phenomenological models for hadronic interactions based on the Standard Model of particle physics. Better understanding of hadronic interactions is essential for making precise predictions, which can then be confronted to experimental data in order to look for signs of physics beyond the Standard Model.

We measure the differences between the decay widths of the B_s^0 and B^0 mesons, $\Delta(B)$, and between that of the D_s^- and D^- mesons, $\Delta(D)$, by analysing approximately 410 000 $B_s^0 \to D_s^{(*)-} \mu^+ \nu_\mu$ and 110 000 $B^0 \to D^{(*)-} \mu^+ \nu_\mu$ decays, which are partially reconstructed in the same $K^+ K^- \pi^- \mu^+$ final state. We measure

$$\Delta(B) = -0.0115 \pm 0.0053 \,(\text{stat}) \pm 0.0041 \,(\text{syst}) \,\text{ps}^{-1}$$

and

$$\Delta(D) = 1.0131 \pm 0.0117 \,(\text{stat}) \pm 0.0065 \,(\text{syst}) \,\text{ps}^{-1}.$$

Using the obtained values of $\Delta(D)$ and $\Delta(B)$ and the B^0 and D^- lifetimes as external inputs, we obtain a measurement of the flavour-specific B_s^0 lifetime,

$$\tau_s^{\text{fs}} = 1.547 \pm 0.013 \,(\text{stat}) \pm 0.010 \,(\text{syst}) \pm 0.004 (\tau_{B^0}) \,\text{ps},$$

and of the D_s^- lifetime,

$$\tau_{D_s^-} = 0.5064 \pm 0.0030 \,(\text{stat}) \pm 0.0017 \,(\text{syst}) \pm 0.0017 (\tau_{D^-}) \,\text{ps},$$

where the last uncertainties originate from the limited knowledge of the B^0 and D^- lifetimes, respectively. Both results are compatible with, and improve upon, previous determinations.

A feasibility study of a D^0 lifetime measurement is performed, by measuring the difference between the decay widths of the D^0 and D^- mesons, $\Delta(D)'$. We reconstruct approximately 2.2×10^6 $B^0 \to D^{*-}(\to \overline{D}^0 (\to K^+\pi^-)\pi^-)\mu^+\nu_\mu$ and 1.6×10^6 $B^0 \to D^{(*)-}(\to K^+\pi^-\pi^-(X))\mu^+\nu_\mu$ decays. We measure

$$\Delta(D)' = 1.4644 \pm 0.0043 \,(\text{stat}) \pm 0.0132 \,(\text{syst}) \,\text{ps}^{-1}$$

Abstract

and with the D^- lifetime as external input, we get an estimate of the D^0 lifetime,

$$\tau_{D^0} = 0.4122 \pm 0.0007\,(\text{stat}) \pm 0.0022\,(\text{syst}) \pm 0.0011(\tau_{D^-})\,\text{ps}.$$

This result is compatible with, but less precise than, current precision and thus validates the method. We discuss possible improvements with larger simulation samples and data sets.

Keywords: LHC, LHCb, particle physics, B physics, lifetime, semileptonic decay.

Zusammenfassung

In dieser Arbeit werden verschiedene Lebensdauermessungen von Mesonen mittels semi-leptonischer B^0- und B_s^0- Zerfällen präsentiert. Die verwendeten Daten mit einer integrierten Luminosität von 3 fb^{-1} wurden mittels Proton-Proton Kollisionen bei einer Schwerpunkts-energie von 7 und 8 TeV, mit dem LHCb Experiment aufgezeichnet.

Die Untersuchung der Lebensdauer von Mesonen spielt eine wichtige Rolle für die Einschrän-kung von Parametern aus phänomenologischen Modellen, welche auf dem Standard Model der Teilchenphysik basieren. Diese können dann weiteren experimentellen Daten gegen-übergestellte werden und somit zur Untersuchung auf Anzeichen für Physik außerhalb des Standard Models verwendet werden.

Wir messen die Unterschiede zwischen den Zerfallsbreiten von B_s^0- und B^0-Mesonen ($\Delta(B)$) sowie von D_s^-- und D^--Mesonen, $\Delta(D)$. Wir studieren 410 000 $B_s^0 \to D_s^{(*)-} \mu^+ \nu_\mu$ und 110 000 $B^0 \to D^{(*)-} \mu^+ \nu_\mu$ Zerfälle, die im gleichen $K^+ K^- \pi^- \mu^+$ Endzustand rekonstruiert werden. Wir messen

$$\Delta(B) = -0.0115 \pm 0.0053 \,(\text{stat}) \pm 0.0041 \,(\text{syst}) \,\text{ps}^{-1}$$

und

$$\Delta(D) = 1.0131 \pm 0.0117 \,(\text{stat}) \pm 0.0065 \,(\text{syst}) \,\text{ps}^{-1}.$$

Mit den gemessenen Werten von $\Delta(D)$ und $\Delta(B)$ und den bekannten Werten der B^0- und D^--Lebensdauern können wir die effektive B_s^0-Lebensdauer messen und erhalten

$$\tau_s^{\text{fs}} = 1.547 \pm 0.013 \,(\text{stat}) \pm 0.010 \,(\text{syst}) \pm 0.004 (\tau_{B^0}) \,\text{ps},$$

und für die D_s^--Lebensdauer

$$\tau_{D_s^-} = 0.5064 \pm 0.0030 \,(\text{stat}) \pm 0.0017 \,(\text{syst}) \pm 0.0017 (\tau_{D^-}) \,\text{ps}.$$

Die letzten Unsicherheiten rühren von der begrenzten Kenntnis der B^0- bzw. D^--Lebensdauern her. Beide Ergebnisse sind kompatibel mit den bisherigen Resultaten und verbessern diese.

Des Weiteren wird eine Machbarkeitsstudie einer D^0-Lebensdauermessung durchgeführt, indem der Unterschied zwischen den Zerfallsbreiten der D^0- und D^--Mesonen $(\Delta(D)')$ ge-messen wird. Dafür rekonstruieren wir etwa 2.2×10^6 $B^0 \to D^{*-}(\to \overline{D}^0(\to K^+ \pi^-)\pi^-)\mu^+ \nu_\mu$ und

Zusammenfassung

1.6×10^6 $B^0 \rightarrow D^{(*)-}(\rightarrow K^+\pi^-\pi^-(X))\mu^+\nu_\mu$ Zerfälle und messen

$$\Delta(D)' = 1.4644 \pm 0.0043\,(\text{stat}) \pm 0.0132\,(\text{syst})\,\text{ps}^{-1}.$$

Zusammen mit der bekannten D^--Lebensdauer erhalten wir eine Schätzung für die D^0-Lebensdauer

$$\tau_{D^0} = 0.4122 \pm 0.0007\,(\text{stat}) \pm 0.0022\,(\text{syst}) \pm 0.0011(\tau_{D^-})\,\text{ps}.$$

Dieses Ergebnis ist kompatibel mit der aktuelle Genauigkeit, jedoch weniger genau. Außerdem werden mögliche Verbesserungen durch größere Daten- und Simulationssätze diskutiert.

Stichwörter: LHC, LHCb, Teilchenphysik, B-Physik, Lebensdauer, semi-leptonische Zerfall.

Résumé

Cette thèse présente des mesures de temps de vie de mésons lourds, en utilisant 3 fb^{-1} de données de mésons B^0 et B_s^0 se désintégrant semileptoniquement, collectées par le détecteur LHCb dans des collisions proton-proton à une énergie de centre de masse de 7 et 8 TeV. L'étude des temps de vie des mésons est importante pour contraindre des modèles phénoménologiques, basés sur le Modèle Standard de la physique des particules, qui peuvent par la suite être confrontés à d'autres mesures expérimentales avec une sensibilité accrue aux sources de physique au-delà du Modèle Standard.

Nous mesurons les différences entre les largeurs de désintégration (l'inverse du temps de vie) des mésons B_s^0 et B^0, $\Delta(B)$, et des mésons D_s^- et D^-, $\Delta(D)$, en analysant environ 410 000 désintégrations $B_s^0 \to D_s^{(*)-} \mu^+ \nu_\mu$ et 110 000 $B^0 \to D^{(*)-} \mu^+ \nu_\mu$, qui sont partiellement reconstruites dans le même état final, $K^+ K^- \pi^- \mu^+$. On mesure

$$\Delta(B) = -0.0115 \pm 0.0053\,(\text{stat}) \pm 0.0041\,(\text{syst})\,\text{ps}^{-1}$$

et

$$\Delta(D) = 1.0131 \pm 0.0117\,(\text{stat}) \pm 0.0065\,(\text{syst})\,\text{ps}^{-1}.$$

En utilisant les temps de vie connus du B^0 et du D^-, on obtient une mesure de la valeur du temps de vie effectif du B_s^0,

$$\tau_s^{\text{fs}} = 1.547 \pm 0.013\,(\text{stat}) \pm 0.010\,(\text{syst}) \pm 0.004(\tau_{B^0})\,\text{ps},$$

et du temps de vie du D_s^-,

$$\tau_{D_s^-} = 0.5064 \pm 0.0030\,(\text{stat}) \pm 0.0017\,(\text{syst}) \pm 0.0017(\tau_{D^-})\,\text{ps},$$

où les dernières incertitudes sont dues à la connaissance limitée des temps de vie du B^0 et du D^-, respectivement. Les deux résultats sont compatibles avec les valeurs précédemment mesurées, et les améliorent.

Une étude sur la faisabilité d'une mesure du temps de vie du D^0 est également décrite, en mesurant la différence entre les largeurs de désintégration des mésons D^0 et D^-, $\Delta(D)'$. On reconstruit environ 2.2 millions de désintégrations $B^0 \to D^{*-}(\to \overline{D}^0(\to K^+\pi^-)\pi^-)\mu^+\nu_\mu$ et 1.6 million de $B^0 \to D^{(*)-}(\to K^+\pi^-\pi^-(X))\mu^+\nu_\mu$. Le résultat final est

$$\Delta(D)' = 1.4644 \pm 0.0043\,(\text{stat}) \pm 0.0132\,(\text{syst})\,\text{ps}^{-1}.$$

Résumé

En utilisant une nouvelle fois le temps de vie connu du D^-, on obtient une estimation du temps de vie du D^0,

$$\tau_{D^0} = 0.4122 \pm 0.0007\,(\text{stat}) \pm 0.0022\,(\text{syst}) \pm 0.0011(\tau_{D^-})\,\text{ps}.$$

Ce résultat est compatible avec les valeurs précédemment mesurées, bien que moins précis, et valide donc la méthode. Des possibilités d'amélioration avec de plus grands échantillons de simulations et davantage de données sont discutées.

Mots-clés : LHC, LHCb, physique des particules, physique du B, temps de vie, désintégration semileptonique.

Contents

Contents

List of Figures

List of Tables

Context and outline

The goal of physics has always been to give a precise and complete picture of the physical processes observed in Nature. The non-gravitational part of the universe can be well described by the Standard Model of particle physics (SM), a theory explaining observed phenomena with a mathematical model of particles and fundamental forces. At the Large Hadron Collider at CERN, beams of protons are collided at high energy to produce large amounts of rare particles; these particles decay and their products are studied by particle detectors. The work presented in this thesis is done in the context of the LHCb experiment, with data collected by the detector during 2010–2012 at 7 and 8 TeV centre-of-mass energies.

This thesis is organised as follows. Chapter 1 gives an overview of the SM of particle physics, with a focus on lifetimes and their definition in this model. Chapter 2 describes the LHCb detector, along with all its subdetectors. The main part of the thesis, Chapter 3, describes the measurement of the B_s^0 and D_s^- lifetimes using semileptonic decays, where the differences between the B_s^0 and B^0, and between the D_s^- and D^- decay widths, are probed. The results from this study improve upon previous determinations, which led to a publication in Physical Review Letters [1]; I also had the opportunity to present them at the Lake Louise Winter Institute (Canada) in February 2017. In Chapter 4, a feasibility study is performed on the extraction of the difference between the D^0 and D^- decay widths, using the same method as in Chapter 3. Finally, a summary is given in Chapter 5.

During my PhD, I also had the opportunity to work for the Upgrade of the LHCb detector, by doing R&D on Silicon Photomultipliers, as briefly explained in Section 2.4. I have also been a teaching assistant for general physics courses and overviewed lab work sessions on nuclear physics for Bachelor students, alongside assisting with Masterclasses for high school students. I have also been following courses on advanced particle physics, statistics and teaching.

1 The Standard Model of particle physics

1.1 The Standard Model

The *Standard Model of particle physics* (SM) is a theory describing building blocks of matter and how they interact [2, 3]. The known elementary particles are summarised in Figure 1.1. Elementary particles can be separated into two families: *fermions* with half-integer spin and *bosons* with integer spin.

Fermions follow the Fermi-Dirac statistics and thus obey the Pauli exclusion principle. Among fermions, we distinguish 6 *quarks*: up (u), charm (c) and top/truth (t) with electric charge $+2/3$ and down (d), strange (s) and bottom/beauty (b) with charge $-1/3$; but also 6 *leptons*: electron (e^-), muon (μ^-) and tau (τ^-) with charge -1 and their associated neutral neutrinos, the electron neutrino (ν_e), muon neutrino (ν_μ) and tau neutrino (ν_τ). These twelve particles can also be classified as three generations of fermions as shown in Figure 1.1. Each fermion f also has an associated antiparticle $\overline{f}$ with C-conjugated internal quantum numbers. While leptons can be found as free particles, quarks are confined inside non-elementary particles called *hadrons*, which have an integer electric charge. Hadrons can be *mesons* (composed of one quark and one anti-quark) or *baryons* (three quarks). It was recently shown that hadrons with four (tetraquark) or five (pentaquark) quarks also exist [4–6], and are sometimes referred to as exotic mesons and baryons, respectively. The hadrons found in nature are the neutron n (quark-content: udd) and the proton p (uud).

The interactions of these fermions are mediated by gauge bosons with an integer spin. We distinguish four different interactions:

- The strong interaction occurs between quarks and is responsible for the quarks being confined into hadrons. It is mediated by eight massless bosons called *gluons* (g).

- The electromagnetic interaction is responsible for the attraction and repulsion of particles with opposite-sign and same-sign electric charge, respectively. It is mediated by the massless photon γ and has an infinite range.

- The weak interaction occurs between all fermions. It is mediated by the massive bosons W^-, W^+ and Z^0. As the masses of these bosons are high (80.4 GeV/c^2 for $W^\pm$ and

3

Standard Model of Elementary Particles
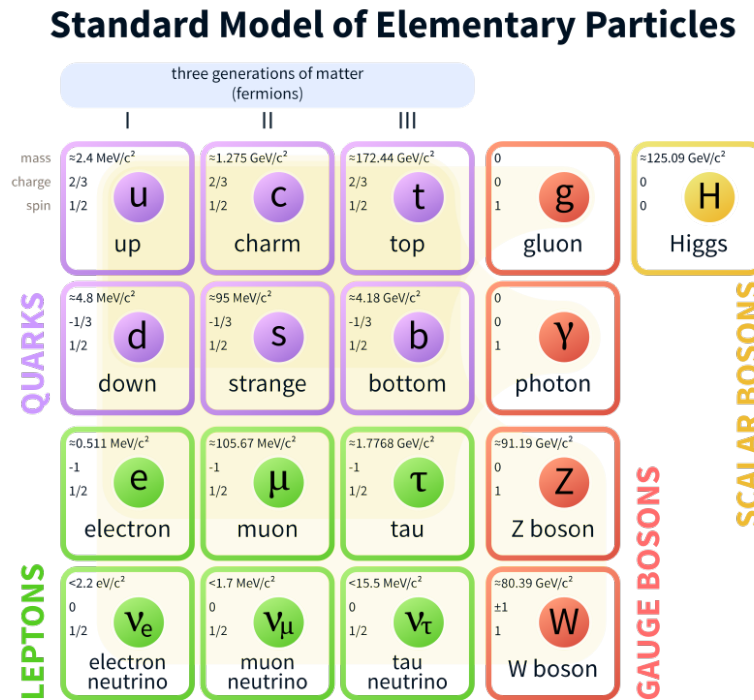
Figure 1.1 – The particles of the Standard Model and some of their properties. [7]

91.2 GeV/c^2 for Z^0), this interaction is short-ranged. The weak interaction is well-known through the beta-decay $n \rightarrow pe^-\overline{\nu_e}$. It is important in the history of particle physics as it allows the violation of some conservation laws through decays forbidden by the strong and/or electromagnetic interactions.

- The gravitational interaction has an effect on all particles. It may be mediated by a massless boson called graviton, hence having an infinite range [8]. Despite being the most visible interaction at macroscopic scale, its strength is very much lower than the other interactions. Gravity is currently explained by general relativity, which is not compatible with quantum mechanics, hence the reason why gravity is not included in the SM.

One can rank these fundamental interactions by their relative strength. By considering the interactions between two protons of an atomic nuclei, the relative magnitudes with respect to the gravitational interaction are 10^{24} for the weak interaction, 10^{35} for the electromagnetic interaction and 10^{37} for the strong interaction.

To complete the list of elementary particles, a scalar (zero-spin) boson needs to be considered: the *Higgs boson* (H). Predicted in 1964 as a result of spontaneous symmetry breaking [9–11], it was finally discovered by two LHC experiments, ATLAS and CMS, in 2012 [12, 13]. Peter Higgs and François Englert received the Nobel Prize in Physics in 2013, almost fifty years after their prediction.

The SM corresponds well with the data taken in particle physics experiments, but it is still

incomplete. For example, the observation of neutrino oscillations [14] implies that neutrinos are massive, while they are massless in the SM. There is no quantum field theory of gravity, and experimental data still fails to show the existence of particles predicted by many theories going beyond the Standard Model.

In next section, we will focus on a specific field of particle physics, which is the time evolution of heavy-flavoured hadrons. The explanations will concentrate on what is strictly necessary to understand the measurements performed in this thesis. For a good overview of flavour physics, see for example Ref. [15].

1.2 Time-evolution of heavy hadrons

1.2.1 Neutral mesons oscillations

This section follows developments done in Refs. [16, 17]. A state that is a superposition of a neutral meson M^0 and its antiparticle $\overline{M^0}$ can be written at a time $t = 0$ as

$$|\phi(0)\rangle = a(0)|M^0\rangle + b(0)|\overline{M^0}\rangle. \tag{1.1}$$

The time evolution of this state needs to be considered with all the possible decay final states f_i included and is thus written as

$$|\phi(t)\rangle = a(t)|M^0\rangle + b(t)|\overline{M^0}\rangle + \sum_i c_i(t)|f_i\rangle, \tag{1.2}$$

where $c_i(0) = 0$ for all i. Computing the time-evolution of this state in all generality is complicated, but if we are not interested in computing all the $c_i(t)$ and if we consider times t much larger than the scale of strong interactions, the time-evolution can be described by an effective Hamiltonian H. The Schrödinger equation reads:

$$i\hbar\partial_t \begin{pmatrix} a(t) \\ b(t) \end{pmatrix} = \boldsymbol{H} \begin{pmatrix} a(t) \\ b(t) \end{pmatrix} = \begin{pmatrix} \boldsymbol{H_{11}} & \boldsymbol{H_{12}} \\ \boldsymbol{H_{21}} & \boldsymbol{H_{22}} \end{pmatrix} \begin{pmatrix} a(t) \\ b(t) \end{pmatrix} = \left(\boldsymbol{M} - \frac{i}{2}\hbar\boldsymbol{\Gamma} \right) \begin{pmatrix} a(t) \\ b(t) \end{pmatrix}, \tag{1.3}$$

where $\boldsymbol{M}$ and $\boldsymbol{\Gamma}$ are two Hermitian matrices linked with transitions via off-shell and on-shell intermediate states, respectively. The diagonal elements are linked to $M^0 \to M^0$ and $\overline{M^0} \to \overline{M^0}$ transitions (same flavour), while the off-diagonal elements are linked to $M^0 \leftrightarrow \overline{M^0}$ (different flavours).

The effective Hamiltonian $\boldsymbol{H}$ has two eigenvalues of well-defined mass and lifetime, called the heavy and light mass eigenstates, and represented for B mesons by the subscript H and L, respectively. Assuming CPT conservation, the eigenstates can be written:

$$|M_L\rangle = p|M^0\rangle + q|\overline{M^0}\rangle \text{ and} \tag{1.4}$$

$$|M_H\rangle = p|M^0\rangle - q|\overline{M^0}\rangle, \tag{1.5}$$

with $|q|^2 + |p|^2 = 1$. The real and imaginary parts of the eigenvalues $\lambda_{L,H}$ correspond to the eigenstate mass and decay width, respectively. We also define the mass and decay width

differences as

$$\Delta m \equiv m_H - m_L = \Re(\lambda_H - \lambda_L) \text{ and} \tag{1.6}$$

$$\Delta\Gamma \equiv \Gamma_H - \Gamma_L = -2\Im(\lambda_H - \lambda_L). \tag{1.7}$$

If $|q/p| = 1$, we say there is no CP violation in the mixing and Δm and $\Delta\Gamma$ correspond to the absolute values of the off-diagonal element of the matrices, $\Delta m = 2|\mathbf{M_{12}}|$ and $\Delta\Gamma = 2|\mathbf{\Gamma_{12}}|$. In this case, the evolution of a pure $|M^0\rangle$ or $|\overline{M^0}\rangle$ initial state is given by

$$|M^0(t)\rangle = g_+(t)|M^0\rangle + \frac{q}{p}g_-(t)|\overline{M^0}\rangle, \tag{1.8}$$

$$|\overline{M^0}(t)\rangle = g_+(t)|\overline{M^0}\rangle + \frac{p}{q}g_-(t)|M^0\rangle, \tag{1.9}$$

where $g_\pm(t) = 1/2(\exp(-i\lambda_H t) \pm \exp(-i\lambda_L t))$ and the time-dependent probabilities that the state oscillates $(-)$ or not $(+)$ are proportional to

$$|g_\pm(t)|^2 = \frac{e^{-\Gamma t}}{2}\left[\cosh\left(\frac{\Delta\Gamma}{2}t\right) \pm \cos(\Delta m t)\right], \tag{1.10}$$

where $\Gamma = (\Gamma_H + \Gamma_L)/2$ is the average decay width. The average lifetime τ is defined as $1/\Gamma$.

1.2.2 B and D mesons lifetime

In this thesis, we will measure differences between the decay widths of B and D mesons. For charged mesons (D_s^-, D^-) the decay width is well-defined; but for neutral mesons (B_s^0, B^0, D^0), two different decay times characterise the two eigenstates.

If no distinction is made in a measurement between the initial B^0 and $\overline{B^0}$ or B_s^0 and $\overline{B_s^0}$ states, they are called untagged. In this case, the decay rate for untagged B mesons is the sum of the decay rates for B mesons going to a final state f and for $\overline{B}$ going to the CP-conjugate final state $\overline{f}$. This rate is written as

$$\Gamma(t) = \Gamma(B(t) \to f) + \Gamma(\overline{B}(t) \to \overline{f}). \tag{1.11}$$

Furthermore, we will consider in this thesis flavour-specific decays, i.e. decays where the final state f $(\overline{f})$ can only be attained by B $(\overline{B})$. Because of the oscillation of neutral B mesons, an initially pure B sample can access both the f and $\overline{f}$ final states. From equation (1.10), if we start with the same amount of B and $\overline{B}$, we can write the time-dependent decay rate $\Gamma(t)$ as

$$\Gamma(t) \propto e^{-\Gamma_H t} + e^{-\Gamma_L t}. \tag{1.12}$$

For the B^0 meson, $\Delta\Gamma/\Gamma$ is expected to be smaller than 0.01 and we can reduce the decay rate to a single exponential with average decay width $\Gamma(B^0)$ and lifetime $\tau(B^0)$. For the D^0 meson, it is also possible to simplify to a single exponential decay. However, for B_s^0, $\Delta\Gamma/\Gamma$ is around 0.13 and fitting a decay-time distribution with a single exponential gives a so-called effective lifetime, which is different from the average lifetime. In flavour-specific decays, the contributions of heavy and light eigenstates are equal, leading to a measurement of an

	Mass [MeV/c^2]	Avg. lifetime [ps]	Δm [ps^{-1}]	$\Delta \Gamma$ [ps^{-1}]
B^0	5279.63 ± 0.15	1.520 ± 0.004	0.5064 ± 0.0019	$(26.7^{+5.8}_{-6.5}) \times 10^{-4}$ [18]
B_s^0	5366.89 ± 0.19	1.505 ± 0.005	17.757 ± 0.021	0.086 ± 0.006
D^0	1864.83 ± 0.05	0.4101 ± 0.0015	$0.0095^{+0.0041}_{-0.0044}$	0.0053 ± 0.0044
D^-	1869.59 ± 0.09	1.040 ± 0.007	–	–
D_s^-	1968.28 ± 0.10	0.500 ± 0.007	–	–

Table 1.1 – Physical properties of D and B mesons relevant to this thesis. Values come from world averages [19]. The value of $\Delta \Gamma$ for B^0 corresponds to the SM expectation.

effective *flavour-specific* lifetime. Let us consider a fit with a single exponential with a decay width Γ_{fs}. Although we would like to find Γ_{fs} such that

$$e^{-\Gamma_{\text{fs}} t} = \frac{1}{2} \left(e^{-\Gamma_H t} + e^{-\Gamma_L t} \right),$$
(1.13)

this is impossible as a sum of exponentials is not an exponential. As $\Delta \Gamma / \Gamma$ is small, we can get a good approximation of the effective lifetime by computing the mean value of the right-hand side using the corresponding probability density function. The effective lifetime is thus

$$\tau^{\text{fs}} \equiv \frac{1}{\Gamma^{\text{fs}}} = \frac{1}{N} \int_0^\infty t \cdot \frac{1}{2} \left(e^{-\Gamma_H t} + e^{-\Gamma_L t} \right) dt,$$
(1.14)

with the normalisation $N = \int_0^\infty \frac{1}{2} \exp(-\Gamma_H t) + \exp(-\Gamma_L t) dt$. After integration and using $\Gamma_H = \Gamma + \Delta \Gamma / 2$ and $\Gamma_L = \Gamma - \Delta \Gamma / 2$, we obtain

$$\tau^{\text{fs}} = \frac{\Gamma_H^{-2} + \Gamma_L^{-2}}{\Gamma_H^{-1} + \Gamma_L^{-1}} = \frac{1}{\Gamma} \frac{\left(1 + \frac{\Delta \Gamma}{2\Gamma}\right)^{-2} + \left(1 - \frac{\Delta \Gamma}{2\Gamma}\right)^{-2}}{\left(1 + \frac{\Delta \Gamma}{2\Gamma}\right)^{-1} + \left(1 - \frac{\Delta \Gamma}{2\Gamma}\right)^{-1}}.$$
(1.15)

Finally, the effective flavour-specific lifetime can be written as

$$\tau^{\text{fs}} = \frac{1}{\Gamma} \left[\frac{1 + \left(\frac{\Delta \Gamma}{2\Gamma}\right)^2}{1 - \left(\frac{\Delta \Gamma}{2\Gamma}\right)^2} \right].$$
(1.16)

The currently known values of the average lifetimes and masses, as well as Δm and $\Delta \Gamma$ for neutral mesons are summarised in Table 1.1.

HQE predictions

Lifetimes of hadrons containing heavy quarks, which decay via weak interaction, can be estimated using a method known as Heavy Quark Expansion (HQE). This framework describes a way to write the decay rates of inclusive decays and can also be used to measure other quantities, such as CKM matrix elements. A summary of HQE calculations used for lifetimes measurements and predictions of lifetimes ratios can be found in Ref. [20].

The HQE shows that a decay rate of a B meson (or D meson) going to a final state X, $\Gamma(B \to X)$,

can be expanded as a sum in powers of $(1/m_b)$, with m_b the mass of the b quark, i.e.

$$\Gamma = \Gamma_0 + \frac{\Lambda^2}{m_b^2}\Gamma_2 + \frac{\Lambda^3}{m_b^3}\Gamma_3 + \frac{\Lambda^4}{m_b^4}\Gamma_4 + \mathcal{O}\left(\frac{\Lambda^5}{m_b^5}\right), \tag{1.17}$$

where Λ/m_b is the expansion parameter. The value of Λ is not simply the QCD scale Λ_{QCD}, but instead needs to be calculated for each order. At order 2, Λ is below 1 GeV; while at the third order, it is larger than 1 GeV. A possible drawback might thus be that this expansion does not converge well enough at higher powers of $1/m_b$, and this is even more likely for D mesons since their expansion is in powers of $1/m_c$, which is larger than $1/m_b$. However, for the lifetimes ratio, no sizeable difference between HQE predictions and experimental data has been seen so far.

These predictions are extremely useful when computing ratios of lifetimes, as many parameters disappear along with their uncertainties. In particular, the expression for the ratio of lifetimes of two hadrons H_A and H_B is

$$\frac{\tau(H_A)}{\tau(H_B)} = \frac{\Gamma_B}{\Gamma_A} = 1 + \frac{\Gamma_B - \Gamma_A}{\Gamma_A} = 1 + \frac{\mu_\pi^2(H_A) - \mu_\pi^2(H_B)}{2m_b^2} + \frac{c_G}{c_3}\frac{\mu_G^2(H_A) - \mu_G^2(H_B)}{2m_b^2} + \mathcal{O}\left(\frac{\Lambda^3}{m_b^3}\right), \tag{1.18}$$

with the matrix elements of the kinetic operator μ_π and of the chromo-magnetic operator μ_G, defined by the Heavy Quark Effective Theory [21], and where c_3 and c_G are Wilson coefficients. The definitions of these operators can be found in Ref. [21]. In particular, the ratio of the (average) B_s^0 and B^0 lifetime can be computed very precisely [20]:

$$\left[\frac{\tau(B_s^0)}{\tau(B^0)}\right]^{\text{HQE}} = 1.001 \pm 0.002. \tag{1.19}$$

The computations for the charm-meson lifetimes are less advanced and it is also less clear if HQE can indeed be applied to lifetimes of D mesons. Currently, the leading results [20] are

$$\left[\frac{\tau(D^-)}{\tau(D^0)}\right]^{\text{HQE}} = 2.2 \pm 0.4, \tag{1.20}$$

$$\left[\frac{\tau(D_s^-)}{\tau(D^0)}\right]^{\text{HQE}} = 1.19 \pm 0.13, \tag{1.21}$$

where the main uncertainties are on the computation of the hadronic matrix elements. We note that these predictions are compatible with the experimental values from Table 1.1, but suffer from significantly large uncertainties.

Measurements of the B_s^0 lifetime are particularly interesting, as there is currently a small tension between the ratio $\tau(B_s^0)/\tau(B^0)$ from HQE and its experimental value of 0.990 ± 0.004. The large uncertainties in the predictions for charm meson lifetimes weaken the constraining power of precision measurements, but improved experimental inputs may stimulate advances on the theory side.

2 LHC and the LHCb detector

2.1 CERN and the LHC

2.1.1 CERN

CERN, the European Organisation for Nuclear Research, is the largest particle physics laboratory in the world. It was established in 1954 by a convention signed by twelve founding states. CERN regularly accepts new members, and now counts among its Member States 22 countries, while many others are associated with the organisation through a different status. Several achievements have been made since the creation of the laboratory. The increasing size of accelerators and reachable energies has allowed scientists to understand better the intrinsic nature of matter and the way it interacts. Among other successes, we can list:

- the first evidence of weak neutral currents by the Gargamelle bubble chamber in 1973 [22, 23], proving the existence of a neutral mediator of the weak fundamental force;

- the discovery of the W and Z bosons, by the UA1 and UA2 experiments in 1983, validating the electroweak theory [24–27]. A Nobel Prize was awarded the following year;

- the proof of existence of exactly three standard neutrino species by the ALEPH, DELPHI, OPAL and L3 experiments at the Large Electron-Positron collider in 1989 [28–31];

- the discovery of the Higgs boson by the ATLAS and CMS experiments at the Large Hadron Collider in 2012 [12, 13].

In addition to these validations of the SM, CERN has always developed many technologies necessary to build accelerators and detectors with better performance. The World Wide Web was also invented at CERN in 1990.

2.1.2 The Large Hadron Collider

The Large Hadron Collider (LHC) is the world's most powerful hadron collider. It was built between 1998 and 2008 in a 27 km tunnel previously used by the Large Electron-Positron

collider (LEP), shut down in 2000. This tunnel is situated between Switzerland and France near CERN's HQ in Geneva. Several experiments are located around the machine, around four crossing points where the hadrons travelling in each beam pipe can collide. The LHC was mainly designed for proton-proton collisions, but can also use beams of heavy ions for runs of proton-lead, lead-lead and xenon-xenon collisions and maybe other ions in the future.

The LHC was built to provide centre-of-mass energies up to $\sqrt{s}$=14 TeV (7 TeV per beam) in pp collisions. Unfortunately, a few days after the commencement of operations at the LHC in 2008, an electrical incident occurred. Many magnets had to be repaired or replaced and tests restarted in 2009, with data-taking in 2010–2011 at $\sqrt{s} = 7$ TeV and in 2012 at $\sqrt{s} = 8$ TeV (Run I) and currently at $\sqrt{s} = 13$ TeV in 2015–2018 (Run II).

The number of collision events N per second is given by

$$N = L \times \sigma_{\text{event}}, \tag{2.1}$$

where σ_{event} is the cross-section for a given interaction and L is the machine *luminosity*. Luminosity is an indicator of the performance of the machine and depends on the number of particles in the beam, the revolution frequency and the spot sizes of the beams at the collision points. The design luminosity of the LHC is 10^{34} cm^{-2} s^{-1} and is planned to be increased in 2025 for the High Luminosity LHC up to a factor 10 [32]. The integral of the luminosity over time is called *integrated luminosity* and is often expressed in inverse femtobarns (1 fb^{-1} = 10^{39} cm^{-2}).

The LHC accelerator complex

Even though the LHC can accelerate protons up to an energy of 6.5 TeV, the beam first needs to be preaccelerated by other machines. CERN's accelerator complex is a group of machines accelerating particles to increasingly higher energies, each machine boosting the energy of the beam and sending it to the next one. Most accelerators also send beams to other experiments, working with beams of lower energies than at the LHC. The accelerator complex is represented in Figure 2.1. This complex and most of its infrastructure are controlled from the CERN Control Centre in Prévessin (France).

The proton source is a bottle of hydrogen gas. Electrons are removed from the atoms with an electric field and the protons are first accelerated by Linac 2 to an energy of 50 MeV. The beam then goes through the Proton Synchrotron Booster (up to 1.4 GeV), the Proton Synchrotron (up to 25 GeV) and is injected into the Super Proton Synchrotron (SPS) until it reaches the energy of 450 GeV. The protons are then finally sent to the two beam pipes of the LHC. Approximately 20 minutes are necessary until the beam reaches the maximum energy of 6.5 TeV. If no problem occurs, beams can circulate for hours inside the pipes and collide at four points corresponding to the four large LHC experiments described in the next section. Heavy ions can also be accelerated in the LHC. In this case, they enter Linac 3, are accelerated in the Low Energy Ion Ring, before being sent to the Proton Synchrotron and following the same path as the protons, at lower energy.
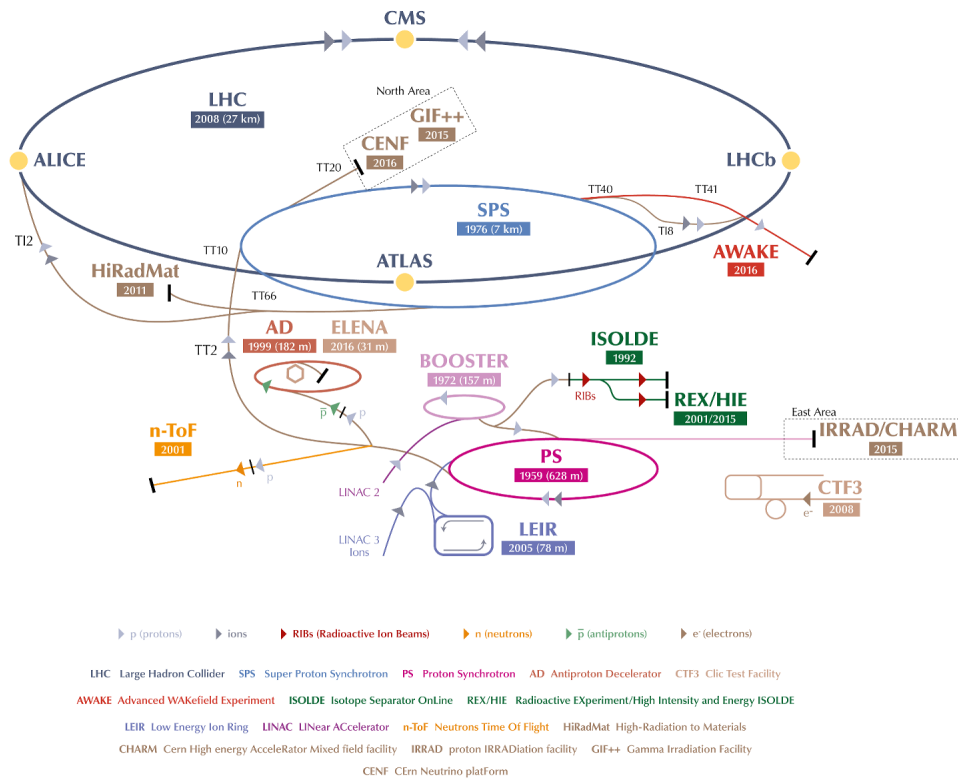
Figure 2.1 – The CERN accelerator complex. [33]

The LHC experiments

Seven experiments around the LHC have detectors to analyse the particles produced by the collisions of protons or heavy ions. The four large experiments (ATLAS, CMS, ALICE and LHCb) are placed at the four collision points.

- **ATLAS** and **CMS** are two general-purpose experiments with a broad physics program, ranging from the Higgs boson to extra dimensions and the nature of dark matter. Even though their goals are similar, their design is different and allows cross-confirmation of measurements and discoveries.

- **ALICE** is a heavy-ion detector, studying collisions of heavy ions to study a state of matter called quark-gluon plasma.

- **LHCb** is an experiment dedicated to study the differences between matter and antimatter and is described in details in Section 2.2.

- **TOTEM** is a small experiment around CMS interaction point dedicated to study forward particles, which are deviated by a small angle by the collision.

- **LHCf** is a small experiment around the ATLAS detector and studies forward particles as a source to simulate cosmic rays, i.e. charged particles reaching Earth from outer space.

- **MoEDAL** is a small experiment near LHCb searching for a hypothetical magnetic monopole.

2.2   The LHCb experiment

The LHCb experiment is exploiting the forward production of *b* and *c* quark pairs to measure rare decays of *b* and *c* hadrons and perform precise measurements of the violation of the *CP* symmetry. The experiment is operated by the LHCb collaboration, a collaboration of over 800 scientists from 74 different institutes of 16 countries and with the support of about 400 technicians and engineers.

The LHCb detector [34] is a single-arm forward detector, sketched in Figure 2.2 along with its subdetectors. It covers angles from around 10 mrad to 300 (250) mrad in the magnet bending (non-bending) plane. This particular geometry is due to the fact that most *b* and *c* hadrons are produced with a small angle with respect to the *pp* collision line. The LHCb detector is composed of many subdetectors. First, a tracking system is composed of a vertex detector called the *VErtex LOcator* (VELO) and a silicon microstrip detector called the *Tracker Turicensis* (TT), both located upstream of the *dipole magnet*; downstream are situated the *Inner Tracker* (IT), just around the beam pipe, and the *Outer Tracker* (OT), around the IT, forming together three T stations (T1, T2 & T3 on the figure). A particle identification system is made of two *Ring Imaging CHerenkov detectors* (RICH), an *Electromagnetic CALorimeter* (ECAL), completed by a *Scintillator Pad Detector* (SPD) and *Pre-Shower* (PS), an *Hadronic CALorimeter* (HCAL) and five *muon chambers* (M1 to M5). All subdetectors, as well as the trigger system and data collection are described in details in the following.
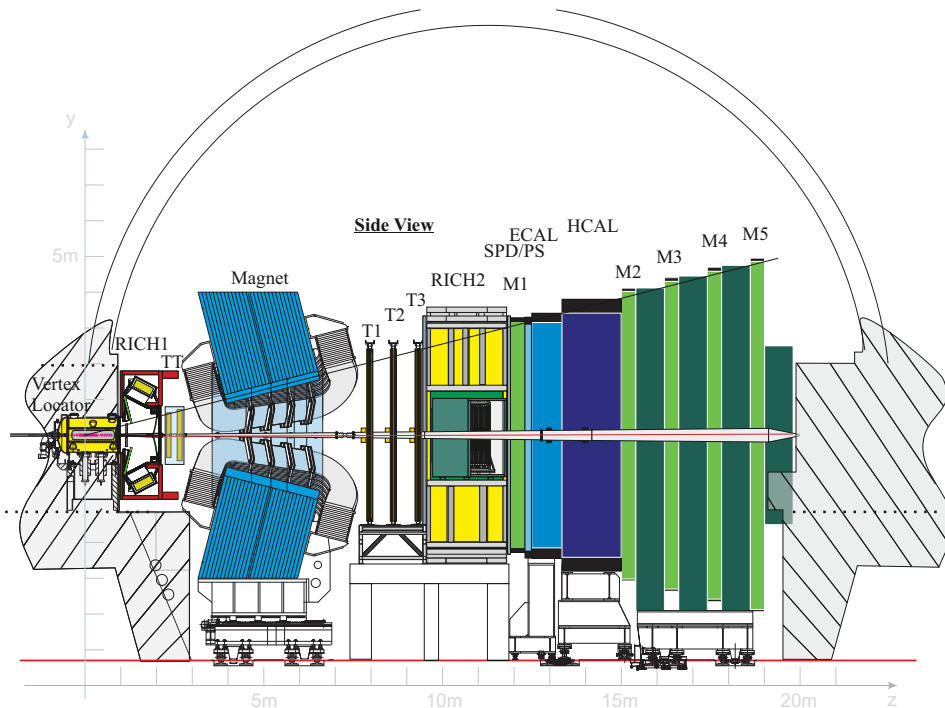
Figure 2.2 – A side-view of the LHCb detector. The subdetectors are described in the text. [34]
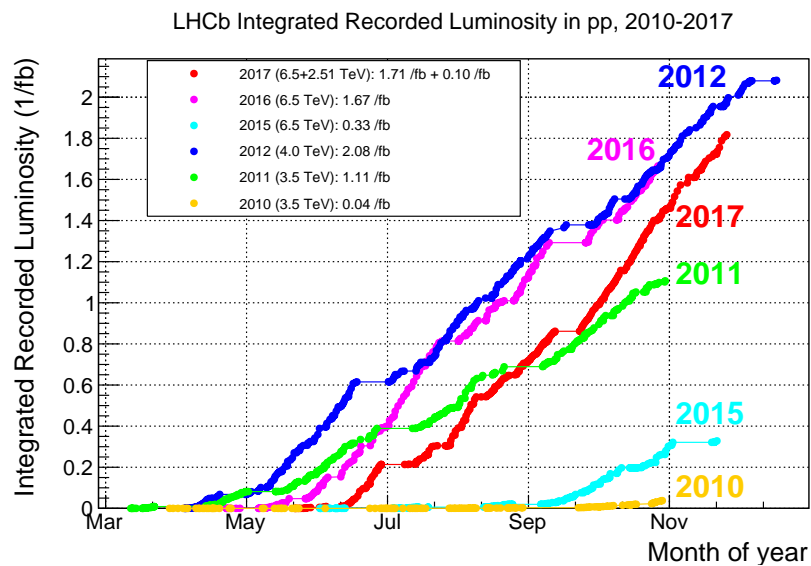
Figure 2.3 – Integrated luminosity recorded by LHCb between 2010 and 2017. The corresponding energy of the proton beam is specified in the legend. [35]
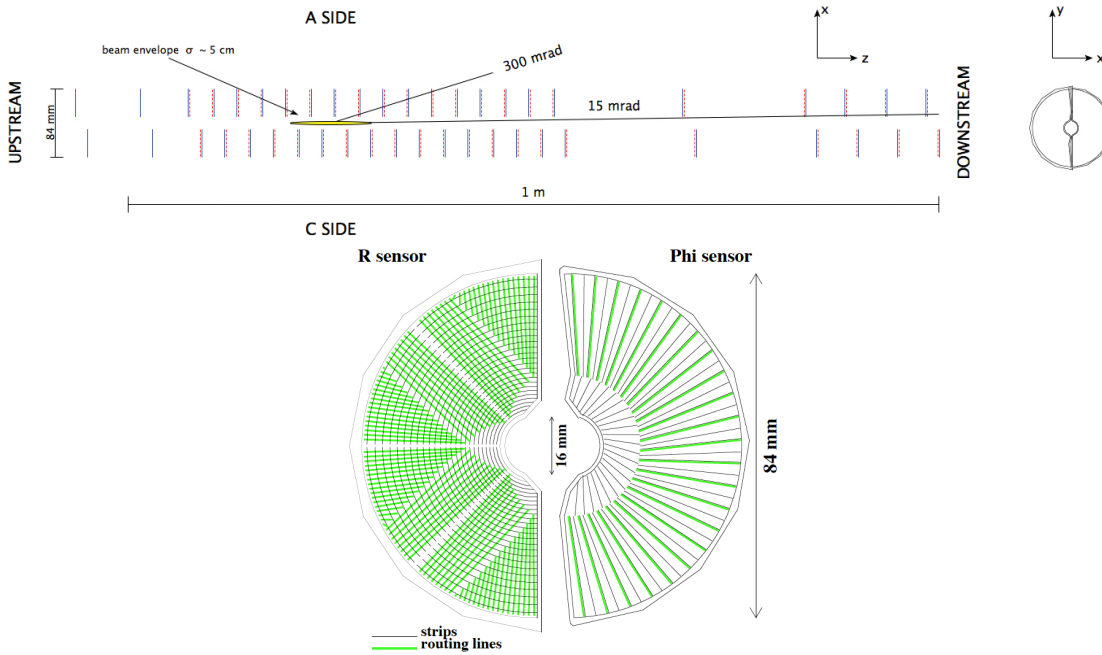
Figure 2.4 – (top) A cross-section on the VELO in the xz and xy planes. The sensors to measure r and ϕ are shown in blue and red, respectively. (bottom) A representation of these two kinds of sensors. The routing lines avoid the regions closer to the beam. [37]

The experiment is currently operating at a luminosity of 4×10^{32} cm^{-2}s^{-1}, which is 25 times lower than the luminosity delivered by the LHC to ATLAS and CMS. However, a clever luminosity levelling system allows starting with beams displaced with respect to each other and gradually centred as the beam intensity reduces, allowing for an almost constant luminosity throughout data taking. The integrated luminosity collected per year by the LHCb experiment from the start of data-taking in 2010 is reported in Figure 2.3.

2.2.1 Tracking system

The Vertex Locator (VELO)

The VELO [36] is a silicon microstrip detector positioned around the interaction region. It provides measurements of track coordinates, which are used to compute primary interaction vertices and secondary vertices, the point where the original b or c hadron decays. The VELO contains almost one hundred silicon sensors arranged along the beam direction (Figure 2.4) and located at only 7 mm from the beam. It is designed such that all tracks within the LHCb acceptance cross at least three of these sensors. This small distance can be achieved only when beams are stable, as LHC needs a larger aperture during injection phase. For this reason, the detector is made of two retractable halves. The VELO contains 21 modules in each half. Each silicon module is approximately semi-circular and contains sensors to measure the components r and ϕ of polar coordinates. It is made of n-on-n silicon detectors and are very sensitive to radiation due to their proximity of the beams.
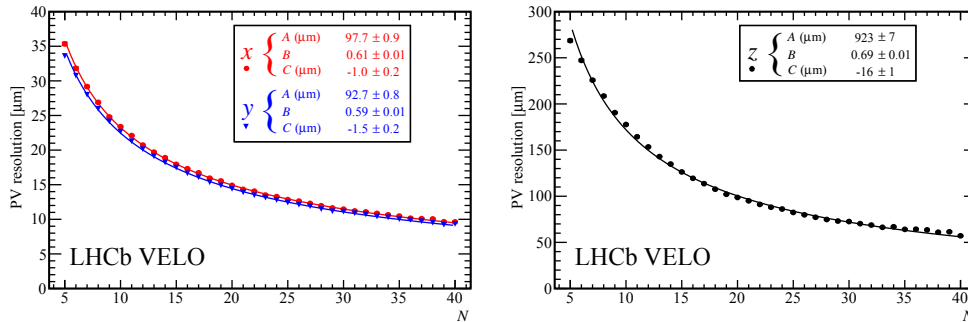
Figure 2.5 – Primary vertex (PV) resolution of events with exactly one PV in 2011 data as a function of the number of tracks forming the vertex. (left) x, y transverse and (right) z longitudinal resolution are shown in red, blue and black respectively. The resolution is fitted with $\sigma = A/N^B + C$ and value of fit parameters are given. [37]

During 2010–2012 data-taking (Run I), the track finding efficiency of the VELO has been determined to be typically above 98 %, by probing very clear J/ψ decays [37]. The vertex resolution depends on the number of tracks forming said vertex, as shown in Figure 2.5, but is about 13 (71) μm in the transverse (longitudinal) plane with 25 tracks. Impact parameter resolution of 12 μm in the transverse plane is found for tracks with high momentum; while for lower momenta, this resolution is larger as multiple scattering in the material increases and reaches 35 μm for particles with transverse momentum of 1 GeV/c.

The Tracker Turicensis (TT)

The TT [38] is also a silicon microstrip detector located just before the LHCb magnet. The TT consists of four detection layers, the second and third rotated by a stereo angle of +5° and −5° with respect to the first and fourth layers. The first two layers cover an area of 1.6 m^2 and the last two, about 2.2 m^2.

The active area is covered by silicon microstrip detectors, each strip with pitch of 198 μm and length up to 33 cm. The detector contains about 900 silicon sensors in total. Sensors are produced by Hamamatsu Photonics, are 500 μm thick, and cover an area of 9.64 cm x 9.44 cm. It results in a hit resolution of ∼ 50 μm. The total detector amounts to around 180k readout channels.

The Inner Tracker (IT)

After the magnet, three tracking stations are found, made of the IT and the Outer Tracker presented thereafter. The IT [39] is another silicon microstrip detector and together with the TT, forms the Silicon Tracker (ST). The IT covers the innermost region, where the particle density is particularly high. It covers an area approximately 120 cm wide and 40 cm high and uses four detection layers, with ±5° stereo angle for the layers in the middle, as for the TT.

The total sensitive surface of about 4.2 m^2 is covered by p^+-on-n silicon sensors of dimensions 320 μm x 110 mm x 78 mm and a strip pitch of 198 μm. It also results in a hit resolution of
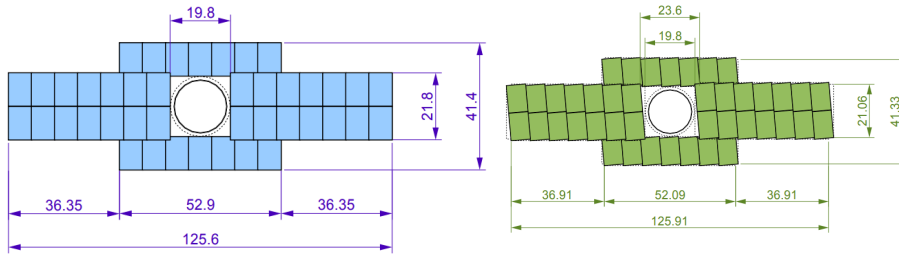
Figure 2.6 – Layout of horizontal (left) and ±5° layers (right) in T2 for the IT, with dimensions given in cm. All tracking stations of the Silicon Tracker have a similar layout, with different dimensions. [39]

about 50 μm. Readout strips of up to 22 cm are used.

The Outer Tracker (OT)

The OT [40] is a gaseous straw tube detector, situated around the IT. It is a drift-time detector used for the tracking of charged particles in a large acceptance. The size of each OT station is chosen to fully cover the total LHCb acceptance (±300 mrad horizontally and ±250 mrad vertically). Modules are arranged in three stations and four layers as for the ST. The OT however uses modules of different sizes, shorter near the middle covered by the IT.

Each module contains two layers of drift tubes with a diameter of 4.9 mm. A mixture of argon and CO_2 is used to guarantee a drift time below 50 ns, allowing for a resolution of 200 μm in the drift direction.

During 2010–2012 data taking, the performance of the OT has been measured [41], showing a reliable and stable subdetector. Typically, 99.5% of the channels were active. It shows a single-hit efficiency of 99.2% near the centre of the straw and confirms the 200 μm design resolution. Radiation damage had no visible effect on the OT.

2.2.2 Particle identification system

Ring Imaging CHerenkov detectors (RICH)

The RICH detectors [42] use the light produced by Cherenkov radiation, when a particle travels faster than the speed of light in a medium, for particle identification. When passing through the gas, the particle will emit a cone of light which is detected with sensors. The opening angle of the cone is directly linked to the velocity of the particle. With the information on the trajectory given by the tracking system it is thus possible to calculate the mass and charge of the particle. This method is primarily used for the identification of charged hadrons (K, π, p). In LHCb, two RICH detectors cover a large range of momenta. Both use a combination of spherical and flat mirrors to focus the Cherenkov light. Hybrid Photon Detectors are used to detect the focused light in the range 200–600 nm.

RICH 1 is located before the magnet, between the VELO and the TT. It covers the low-momentum range of ~1–60 GeV/c using aerogel and C_4F_{10} as gas and covers the full LHCb
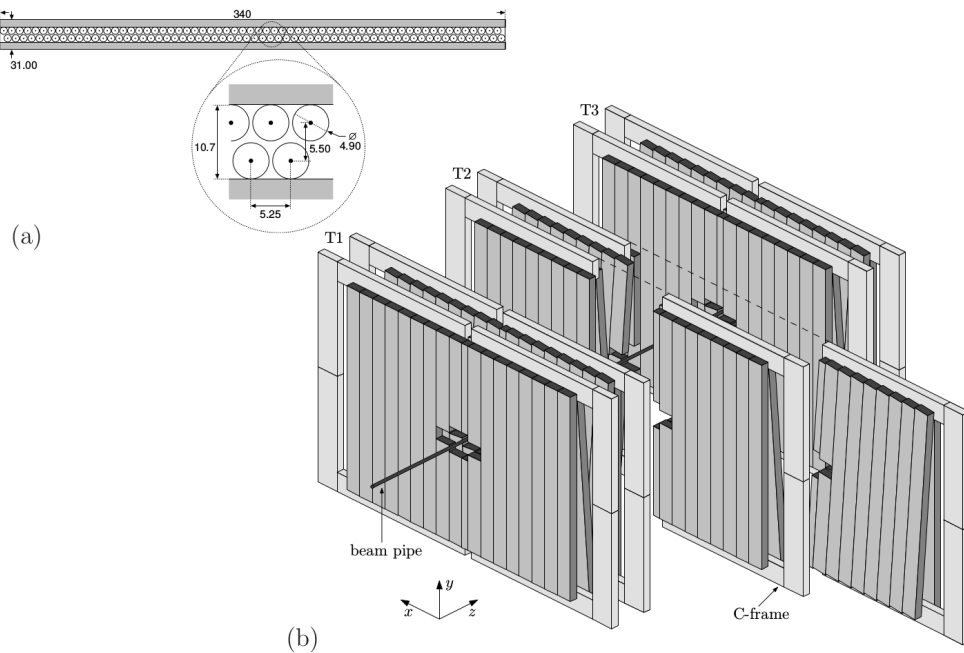
Figure 2.7 – (a) Module cross-section of the OT with dimensions of the straw tubes in mm and (b) arrangement of modules into the T stations. The cross-shaped hole is space for the IT and the beam pipe. [41]

acceptance from ±25 mrad to ±300 (±250) mrad in the horizontal (vertical) plane. The optical layout is vertical as shown in Figure 2.8.

RICH 2 is located after the magnet, between the tracking and the muon stations. It covers a high momentum range from ~15 to beyond 100 GeV/c using CF$_4$ as gas and covers a limited part of the acceptance, from ±15 mrad to ±120 (±100) mrad in the horizontal (vertical) plane. Unlike RICH 1, the optical layout is horizontal, as shown in Figure 2.8.

The RICH detectors allow a very good separation between kaons, pions and protons. By averaging over the full range 2–100 GeV/c, the kaon efficiency can reach 95% for 10% of pion misidentification, or by sacrificing some statistics, 85% of efficiency for 3% of misidentification [43]. These numbers are dependent on the track momentum.

The calorimeters (ECAL and HCAL)

Calorimeters [44] are designed to stop most particles passing through the detector and to measure their energies. They provide identification of charged, but also neutral particles, such as photons, neutrons or π^0's. Calorimeters also provide a fast measurement of transverse energies of these candidates. The calorimeters cover the full LHCb acceptance. In all calorimeters, the scintillator tiles are produced from a mixture of plastics and the reemitted light is transported through fibres to be read by photo multiplier tubes.

The electromagnetic calorimeter (ECAL) measures the energy of light particles, such as electrons and photons. After the ECAL, the Pre Shower (PS) ensures a good separation between
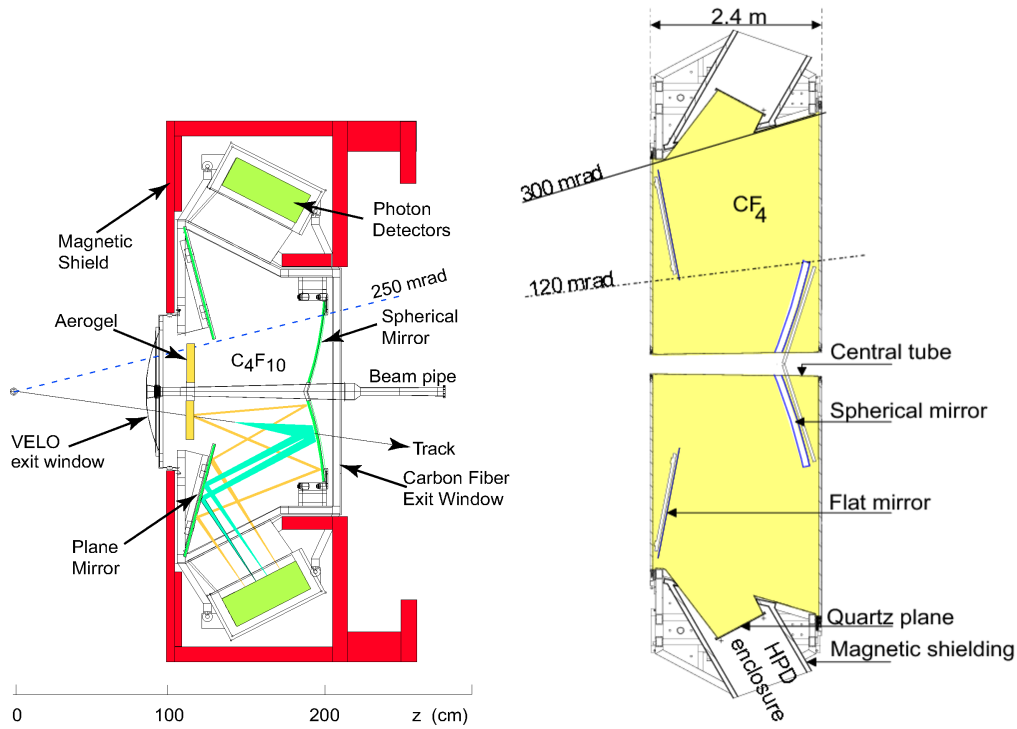
Figure 2.8 – Side view schematic layout of RICH1 (left) and top view schematic layout of RICH 2 (right). [34]

electrons and pions thanks to its longitudinal separation with the ECAL, and the Scintillating Pad Detector (SPD), in front of the PS, selects charged particles to discriminate between electrons and photons. The ECAL uses a shashlik technology, a sandwich-like structure with different layers of scintillator and lead. The design energy resolution is $\sigma_E/E = 10\%/\sqrt{E} \oplus 1\%$, with E in GeV.

The hadronic calorimeter (HCAL) measures the energy of hadrons, such as kaons, pions or neutrons. It is made of tiles of iron and scintillating material. A total of 86 000 tiles are positioned parallel to the beam axis. In the beam direction, the separation between scintillator and absorber corresponds to the mean interaction length in steel, while the tiles are separated by 1 cm of iron in the lateral direction. The energy resolution is estimated by simulations to be $\sigma_E/E = (69 \pm 5)\%/\sqrt{E} \oplus (9 \pm 2)\%$, with E in GeV.

The muon system

The muon system [45] is a gaseous detector. The system is made of 5 rectangular stations or chambers (M1–M5) covering the full LHCb acceptance and shown in Figure 2.9. Station M1 is placed between RICH 2 and the calorimeters, while stations M2–M5 are placed downstream of the calorimeters, at the very end of the detector, and are separated by 80 cm of iron absorbers. The detectors used are multi-wire proportional chambers, except for the inner region of M1, where triple-Gas Electron Multiplier detectors are used.
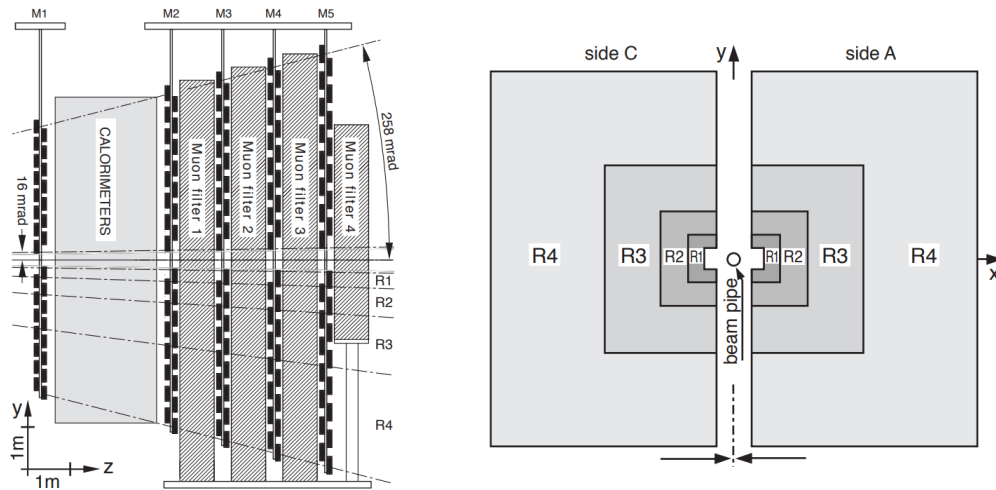
Figure 2.9 – Side view of the muon chambers (left) and cross-section view with four regions (R1–R4) with channel size increasing with the ratio 1:2:4:8 (right). [46]

The muon system identifies muons going through the detector and gives a fast estimate of their transverse momentum for the trigger. Muons play a major role for many measurements, as they are the easiest leptons to identify and play a crucial role in semileptonic b decays. A muon needs a momentum of about 6 GeV/c to cross all muon chambers and the calorimeters in-between; muons with momentum below 3 GeV/c may not even reach more than one muon chamber. Each muon station has a hit efficiency above 99%. For muons with momentum above 3 GeV/c, the muon efficiency is in the range 95–98% for a pion and kaon misidentification rate of 1% [46].

2.2.3 Trigger system

The collision rate at LHCb is very high, at the level of the bunch crossing rate of 40 MHz. However, most of these events do not hold much relevance from the physics point of view and the trigger system aims at reducing the event rate at 5 kHz, before storing them on disk. The trigger is structured into two sequential decision levels: the hardware-based Level 0 (L0) trigger and the software-based High Level Trigger (HLT). The flow of the trigger is summarised in Figure 2.10.

The L0 trigger operates synchronously with the bunch crossing frequency. It uses only hardware information to reduce the event rate to 1 MHz, which is the maximum readout rate with the current electronic readout. The L0 trigger reconstructs the energy of hadrons, electrons and photons in the calorimeters and muons in the muon chambers. It also estimates the number of primary pp interactions with the VELO and the number of tracks with the number of hits in the SPD. Hadron candidates require a high transverse energy (E_T) in the HCAL; photon and electron candidates, high-E_T in the ECAL and hits in the PS, as well as an additional hit in the SPD for the photons. The muon trigger looks for the two muons with the largest transverse momentum, from which muon and dimuon candidates are extracted.
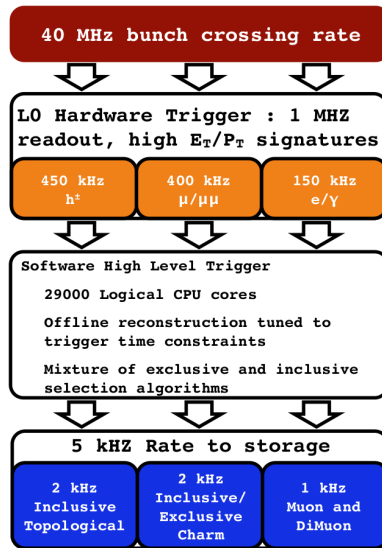
Figure 2.10 – Summary of the trigger flow and approximate rates at each step for Run I (2010–2012 data taking). [48]

The HLT operates after the hardware stage and further reduces the rate. During Run I, the rate was reduced from 1 MHz to 5 kHz. The HLT is split in two levels: HLT1 with fast but partial event reconstruction and HLT2 with full event reconstruction, although a simplified and faster version than the offline version. At the HLT1 level, additional information from the VELO and tracking stations is used to complete the information from the L0 trigger and tracks are selected mainly based on their transverse momentum (p_T) and impact parameter (IP) with respect to the primary vertex. The HLT2 uses full event information to select exclusive and inclusive decays following specific topologies.

For 2015–2018 data-taking at $\sqrt{s} = 13$ TeV, the HLT software was upgraded to allow an output rate of ~ 14 kHz. Selected events in HLT1 are buffered on local disks, allowing HLT2 to be performed when computing time is available, using the last version of calibration and alignment. This greatly minimises the differences between online and offline reconstructions. [47]

2.2.4 Event reconstruction and simulation

In order to reconstruct detected events and to simulate them with Monte Carlo (MC) events, a software framework is used, commonly referred to as the LHCb software. Different applications are responsible of various tasks: event generation, detector simulation, event reconstruction, etc.

Simulated events are first generated with GAUSS [49]. In GAUSS, pp collisions are generated using PYTHIA [50, 51] with a specific LHCb configuration. Then, the decays of hadronic particles are described by EVTGEN [52], in which final-state radiation is generated using PHOTOS [53]. The interaction of the various particles with the detector material and magnetic field, as well as further decays of particles in the detector are implemented with the GEANT4 [54,

55] toolkit. The output of GAUSS enters a digitisation phase through BOOLE [56] in order to simulate the behaviour of the electronics of each subdetector. This step is the last one specific to simulated events and BOOLE output has a similar form as data collected by LHCb.

Simulated events and data are then reconstructed using the same algorithms. The event is fully reconstructed by using track information and signal from calorimeters with BRUNEL [57], and MOORE [58] reproduces the decision of the HLT trigger. Finally, DAVINCI [59] is the analysis package used to study the contents of LHCb events.

2.3   The LHCb Upgrade

The LHCb detector will be upgraded in 2019–2020, during a long shutdown of the LHC. The objective is to allow the detector to take data at higher luminosity and with a full detector readout at 40 MHz. The target luminosity is 1–2×10^{33} cm^{-2}s^{-1}, i.e. up to 5 times higher than now, in order to collect up to 50 fb^{-1} during five years of data taking.

This requires a great number of changes, as the current detector could not cope with such a high rate. It requires a full rebuilding of the front-end electronics and moving to a fully software-based trigger. It also includes many changes in the subdetectors:

- The VELO will be replaced by tracking layers based on $50 \times 50 \, \mu$m pixels, ensuring a better hit resolution and simpler track reconstruction. Its internal radius will be smaller to allow detection closer to the pipe, and detector material will be significantly reduced. The impact parameter resolution is expected to be improved by 40%.

- To replace the TT, a new Upstream Tracker (UT) will be installed. It is made of silicon microstrip detectors and will be closer to the pipe with respect to the current tracker; it will also have a better hit resolution.

- The downstream tracking stations will be replaced by a Scintillating Fibre (SciFi) tracker. The SciFi tracker is made of 12 detection planes of dimensions of about 6×5 m. Each detector plane is composed of mats of six layers of compactly arranged scintillating fibres. The fibres are 2.5 m long and will be positioned vertically. In the middle of the fibre length, mirrors are glued in order to collect more light to be sent to the end of the fibres. The scintillating light is read out by Silicon PhotoMultipliers (SiPM) packaged in arrays of 128 channels of $250 \times 1625 \, \mu$m. Each channel is made of 104 avalanche photo-diode pixels of $50 \times 50 \, \mu$m. The SiPMs will be cooled at -40°C to decrease noise. EPFL has been playing a main role in the development and construction of the SciFi tracker. I had the opportunity to work on the SiPMs of the SciFi tracker during my thesis, as explained in Section 2.4.

- The RICH will be modified to handle the much higher occupancy, mainly by changing the mirrors of RICH1.

- The calorimeters and muon chambers will not change much, except the replacement of the front-end electronics and the removal of stations used only by the hardware trigger
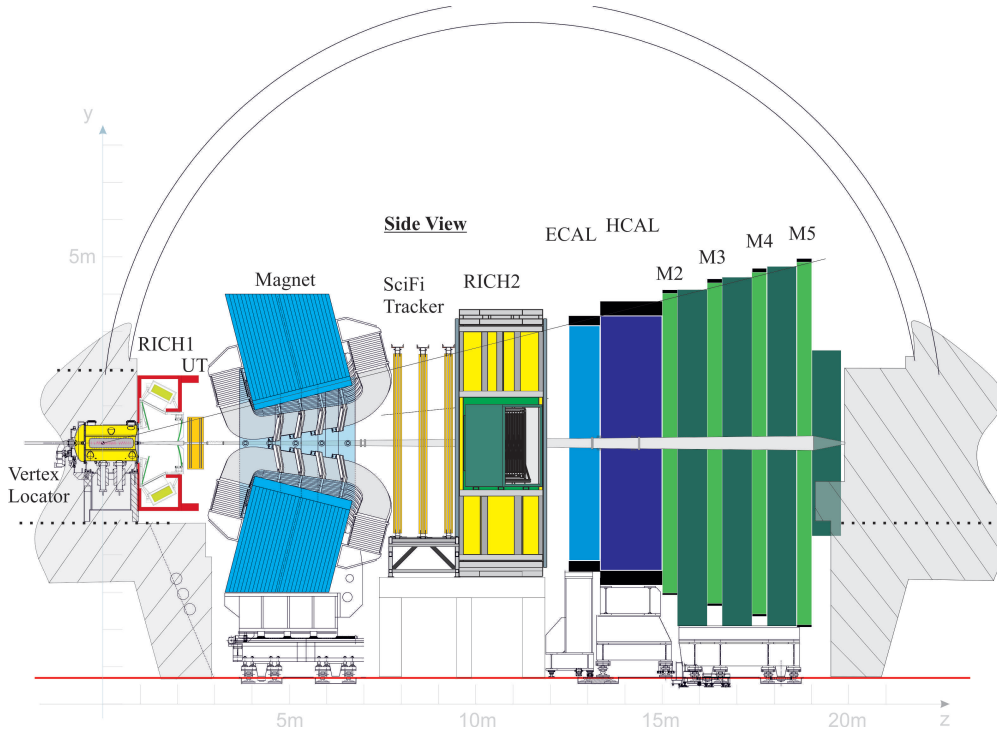
Figure 2.11 – A side-view of the upgraded LHCb detector. To compare with Fig. 2.2. [60]

during Run I and II.

Figure 2.11 shows a sketch of the upgraded detector. Details of the upgrade of the different subdetectors can be found in the different Technical Design Reports [60–64]. Another upgrade is already foreseen in order to use the opportunities of the High Luminosity LHC [65]. This upgrade is planned for 2030.

2.4 SiPM characterisation for the SciFi tracker

In the context of the LHCb SciFi tracker, R&D was necessary in order to select the SiPMs to be used for the Upgrade. I have measured the properties of different products from two manufacturers: KETEK GmbH (Germany) and Hamamatsu Photonics (Japan). Here I will mainly discuss the methods used to assess the performance of the different detectors. The results date back to 2014–2015 and several iterations with the manufacturers have followed since then. Finally, Hamamatsu detectors developed in collaboration with Hamamatsu and CERN have been selected for the SciFi tracker. The detailed characteristics of these detectors can be found in Ref. [66].

An SiPM is a photon detector composed of avalanche photo-diode pixels operating in Geiger mode. We use 128-channels arrays of SiPM mounted on a flexible cable (Figure 2.12). The channels are ~250 μm wide and composed of about one hundred pixels connected in parallel. I will briefly explain thereafter the main characteristics defining the performance of an SiPM
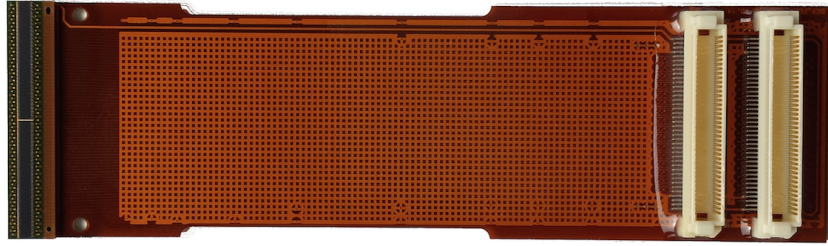
Figure 2.12 – Hamamatsu detector mounted on a flexible cable. The green part on the left is the detector itself, with the dark part being the active area. Version of the 2014–2015 iteration.

detector and the methods used to characterise them.

2.4.1 Characterisation methods

I-V **scan and breakdown voltage** The current passing through an SiPM increases significantly above a given voltage called breakdown voltage V_{bias}, which is the voltage necessary to start an avalanche in the photodiodes. This parameter is crucial to compute the overvoltage ΔV, the difference between the operating and breakdown voltages, which characterises the SiPM performance. Knowing the breakdown voltage of each channel is therefore necessary to apply the same overvoltage to each of them and have a uniform detector response over all channels.

One method to measure V_{bias} consists of scanning the bias voltage V and measuring the current I (*I-V* scan). To obtain V_{bias}, $I\frac{dV}{dI}$ is plotted and a straight line is fitted in the linear region slightly after the sharp increase in current, as can be seen in Figure 2.13. The intersection of the line with zero gives the value of V_{bias} with a precision of ~100 mV. V_{bias} can also be obtained in a more reliable and faster way by measuring the gains of the detector at different ΔV and extrapolating them linearly to zero.

The breakdown voltage also varies linearly with the temperature in the range of interest (-50°C to room temperature). The linear temperature coefficient is determined by measuring the breakdown voltage at different temperatures and will be used to adjust V_{bias} at -40°C, the operating temperature for the SiPMs used in the SciFi tracker. SiPMs with a small temperature coefficient are preferred to ensure that temperature variations have only a small temperature effect on the breakdown voltage and therefore on the gain.

Pulse shape and correlated noise The pulse shape resulting from the electric signal due to a single photon is characterised with an oscilloscope. Typical signals can be seen in Figure 2.13. The part after the triggered peak can be approximated as a sum of two decaying exponential functions with short (τ_{short}) and long (τ_{long}) decay constants. While the fast pulse is dominated by the acquisition bandwidth of our oscilloscope ($\tau_{short} < 1$ ns), the slow
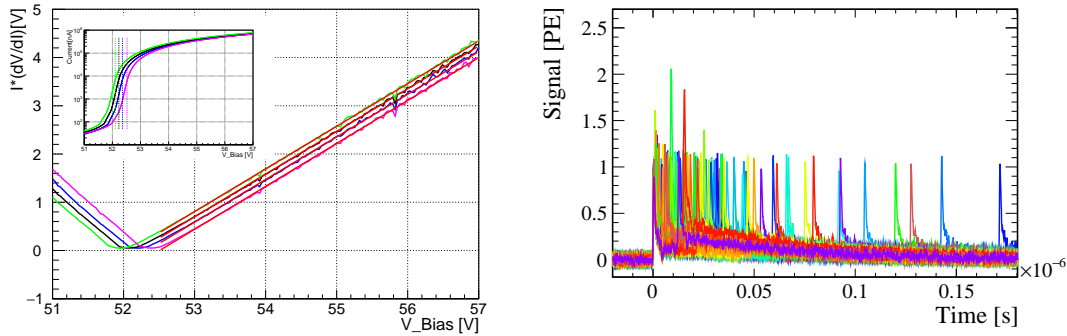
Figure 2.13 – (left) Examples of the fit to get the breakdown voltage from an *I-V* scan. (right) Many pulse waveforms recorded by an oscilloscope with cross-talk peaks.

time component can be obtained by fitting the tail of the pulse shape with an exponential. The decay constant of the slow pulse, τ_{long}, should not be too large to avoid dead time and to avoid spill-over effects given the high data acquisition frequency of the LHCb Upgrade trigger.

Different types of *correlated noise* can also pollute the signal. This correlated noise increases with the amount of signal. First, the *cross-talk* happens when one of the infrared photons produced in an avalanche travels to, and activates, a nearby pixel. Opaque optical trenches are implemented between the pixels to reduce this effect; however, they increase the non-sensitive area of the detector and should therefore not be too large to ensure a high hit detection efficiency. Second, the *after-pulses* happen when a fired pixel triggers another avalanche during the recovery time because of trapped charge carriers. Cross-talk and after-pulse probabilities increase with ΔV.

Gain   The gain is the average number of electrons produced during the avalanche triggered by a detected photon. For SiPMs, this value is around 10^6–10^7. The gain can be computed, for example, by measuring the total charge of a single photon peak (the area under the peak). The gain G can then be computed as $G = Q/(Ae)$, with Q the charge, A the gain of the amplifier and e the elementary electric charge. High gain is necessary to bring the signals to a measurable level and ensure single photon detection capability. However, cross-talk also increases with gain and a trade-off needs to be found, taking these two constraints in mind. The gain also increases linearly with the overvoltage.

Photo-detection efficiency   The photo-detection efficiency (PDE) is the ratio between the number of detected photons to the number of incident photons. Although it is difficult to make an absolute measurement, the relative PDE (with respect to another detector, here a photodiode) can be computed as a function of the wavelength. The relative PDE can be computed by the measurement of the current from the SiPM (I_{SiPM}) and from a photodiode (I_{PD}) in the same conditions.

The PDE measurement is made in a light-tight box, where a Xenon lamp is coupled to a

monochromator to scan through different wavelengths. Light travels through an optical fibre and reaches the SiPM or the photodiode. The PDE is thus

$$PDE = QE_{PD} \cdot \frac{I_{SiPM}}{G \cdot I_{PD}} \frac{A_{PD}}{A_{SiPM}}, \qquad (2.2)$$

where the quantum efficiency of the photodiode, QE_{PD}, is given by the manufacturer and A_{PD}/A_{SiPM} are the active surface of the photodiode and SiPM, respectively. The current I_{SiPM} has to be corrected for the contribution of correlated noise.

The parameters of interest for the SciFi tracker are the peak of the PDE distribution and the average value of the PDE in the region of interest, corresponding to the fibre emission spectrum.

Radiation hardness   As the SiPM detectors must provide good performance for several years in the LHCb detector, tests have been conducted to ensure that the performance of the detector is not excessively altered by radiation. Detector samples have been irradiated at a nuclear reactor to the dose expected at the end of LHCb operation and characterisation parameters can be measured and compared with those measured before the irradiation. In particular, it is interesting to measure another parameter called dark count rate (DCR), which is the frequency of background events in a signal-free environment and is calculated as

$$f_{DCR} = \frac{I}{G \cdot e}, \qquad (2.3)$$

where I is the current measured in a dark environment, where no signal is expected. The DCR is an important source of noise after radiation, but decreases with temperatures. For example, the DCR of Hamamatsu detectors is reduced by a factor two by decreasing the temperature by about 10°C.

2.4.2   Comparison and conclusion

In order to compare different SiPMs, it is first required to choose an appropriate ΔV. A higher overvoltage increases the amount of signal as the PDE increases and reduces the relative effect of the temperature dependence, but also increases all sources of noise: cross-talk, after-pulse and dark count rate. Although the characterisation is done for multiple values of ΔV, we compare here numbers for $\Delta V = 3.5$ V. Different properties for two detectors characterised in 2014 and more recently in 2016 for an Hamamatsu detector only are presented in Table 2.1.

The KETEK detectors have a low breakdown voltage and a small temperature dependence; however, the Hamamatsu detectors have a higher PDE at the peak and for the average in the region of interesting wavelengths, a faster pulse shape and are more radiation hard. Furthermore, Hamamatsu detectors are usually fully functional, while the KETEK ones come with many broken channels, due to the lack of a protective layer against humidity. The 2016 Hamamatsu detectors have better performances on many aspects and in particular much lower cross-talk and almost no after-pulse. A notable drawback is the larger value for the slow

	KETEK 2014	Hamamatsu 2014	Hamamatsu 2016_HRQ
Breakdown voltage [V]	23.6	54.7	51.0
Cross-talk + after-pulse	9%	12%	5.5%
Temperature coeff. [mV/K]	15	54	60
Gain [10^6]	12	3.5	3.1
PDE peak	43%	46%	48%
τ_{short} [ns]	<1	<1	<1
τ_{long} [ns]	~240	~22	~60

Table 2.1 – Comparison of the properties of one of the best 2014 KETEK detector (w1c3), one of the S10943-3183(x) 2014 Hamamatsu detectors and the 2016 Hamamatsu detector described in Ref. [66]. The properties are given for an overvoltage of 3.5 V.

component of the pulse shape compared to the 2014 Hamamatsu detector, which can be a source of spill-over signals in the high occupancy region of the detector.

As these values are now outdated with respect to the technologies used in the SciFi tracker, I redirect the reader to the upcoming Ph.D. theses by O. Girard and A. Kuonen from EPFL, which will discuss the latest results and present the choices and compromises made for the SiPMs used in the SciFi tracker and give more details about the fibre mats which will be installed in the upgraded detector.

3 Measurement of B_s^0 and D_s^- mesons lifetimes

3.1 Introduction

Precise measurements associated with quark-flavour dynamics probe the existence of particles and interactions at energies much larger than directly accessible in high-energy collisions. Indications of non-SM dynamics are typically searched for by comparing the experimental results with the values predicted in the SM. The accuracy of these predictions is often constrained by poorly known parameters associated with the phenomenology of the strong interaction at low energies, a region where QCD calculations are complex to perform. Typically, predictivity is recovered by resorting to effective models such as HQE, described in Section 1.2.2. Experimental measurements help to verify the range of validity of these models and to tune their free parameters. Lifetimes of bottom hadrons are particularly valuable for this purpose, because of their precision. Improved lifetime measurements reflect into improved predictions of quantities sensitive to non-SM dynamics, and ultimately allow for enhancing and sharpening searches for non-SM physics.

The goal of this analysis is a precise measurement of the flavour-specific B_s^0 meson lifetime,

$$\tau_s^{\text{fs}} = \frac{1}{\Gamma_s} \left[\frac{1 + \left(\frac{\Delta\Gamma_s}{2\Gamma_s}\right)^2}{1 - \left(\frac{\Delta\Gamma_s}{2\Gamma_s}\right)^2} \right] , \tag{3.1}$$

as defined in Section 1.2.2, using semileptonic decays. Thanks to large event samples, semileptonic decays offer the best potential for the ultimate precision in lifetime measurements. However, neutrinos and possibly neutral mesons in the final state, prevent from fully reconstructing the decay, thus introducing potentially serious systematic limitations associated with difficulties in constraining the contamination from backgrounds and in deriving the decay time from the observed decay length distribution.

The current best determinations of τ_s^{fs} are reported by the D0 collaboration, which reported $\tau_s^{\text{fs}} = 1.479 \pm 0.010 \pm 0.021$ ps [67] using $B_s^0 \to D_s^- \mu^+ \nu X$ decays[1], and by the LHCb collaboration,

---

[1] The symbol X identifies generically any other signal decay-product not included in the signal candidate reconstruction. Charge-conjugated decays are included unless stated otherwise.

which measured $\tau_s^{\text{fs}} = 1.535 \pm 0.015 \pm 0.014$ ps [68], using $B_s^0 \to D_s^- \pi^+$ decays. The first result has a better statistical uncertainty, but its final precision is limited by a significant systematic uncertainty, dominated by the contribution of large backgrounds and uncertainties in their composition.

In this analysis, we use a sample of several hundred thousands $B_s^0 \to D_s^-(\to K^+ K^- \pi^-)\mu^+ \nu X$ decays collected by LHCb during Run I, and in which the B_s^0 meson flavour at the time of production is not identified. The large signal yield gives the potential for a world-leading result, provided that we control the effect of systematic uncertainties. The fundamental idea to control these uncertainties is to measure the difference between the decay widths of the B_s^0 and B^0 mesons,

$$\Delta(B) = \Gamma(B_s^0) - \Gamma(B^0), \tag{3.2}$$

from a fit to the ratio of $B_s^0 \to D_s^-(\to K^+ K^- \pi^-)\mu^+ \nu X$ and $B^0 \to D^-(\to K^+ K^- \pi^-)\mu^+ \nu X$ event yields as a function of decay time. The final result of $\Delta(B)$ has been blinded. From its fitted value, using as input the precisely known value of the B^0 lifetime [19] we can improve the precision on the flavour-specific B_s^0 lifetime, as the B^0 lifetime is measured more precisely. In particular, we determine the B_s^0 and B^0 signal yields, as a function of decay time, using a fit to the *corrected* mass distribution of the selected candidates. The corrected mass [69] is determined from the $D_{(s)}^- \mu^+$ invariant mass, $m(D\mu)$, using the momentum of the $D_{(s)}^- \mu^+$ system transverse to the $B_{(s)}^0$ flight direction, $p_\perp(D\mu)$, to partially compensate for the momentum of the unreconstructed decay products:

$$m_{\text{corr}} = \sqrt{m^2(D\mu) + p_\perp^2(D\mu)} + p_\perp(D\mu). \tag{3.3}$$

The corrected mass corresponds to the invariant mass of the $D\mu\nu$ system if the longitudinal momentum of the visible decay products in the B rest frame can be ignored. The B decay time is calculated from the known $B_{(s)}^0$ mass [19], m_B, the observed $B_{(s)}^0$ decay length, L, the momentum of the $D_{(s)}^- \mu^+$ system, $p(D\mu)$, and a correction factor k to take into account for the component carried by decay products not included in the reconstruction:

$$t = \frac{m_B \, L}{p(D\mu)} \, k. \tag{3.4}$$

The correction k is an event-by-event scale factor determined from simulation and depends on the $D_{(s)}^- \mu^+$ mass, as explained in Section 3.6.1. To improve the scale-factor determination, the composition of the simulated sample in terms of different decay channels contributing to the inclusive $D_{(s)}^- \mu^+ X$ final state is matched to the observed ratios in data. The final decay-time-dependent fit to the ratio of B_s^0 and B^0 signal yields includes the effects of the decay-time resolution, modelled using simulation. The ratio of the decay-time acceptances of B_s^0 and B^0 decays is consistent with being uniform once a correction is applied to account for the different D_s^- and D^- lifetimes, which induce a different trigger efficiency in the two decay modes. The analysis method is validated directly on data by measuring the ratio of two semileptonic B^0 decays event yields, $B^0 \to D^-(\to K^+ K^- \pi^-)\mu^+ \nu X$ and $B^0 \to D^-(\to K^+ \pi^- \pi^-)\mu^+ \nu X$, as a function of decay time to be consistent with unity.

By measuring the ratios of B_s^0 and B^0 signal yields as a function of the decay time of the $D_{(s)}^-$ candidates, we also obtain a precise determination of the decay-width difference between D_s^- and D^- mesons,

$$\Delta(D) = \Gamma(D_s^-) - \Gamma(D^-). \tag{3.5}$$

The $D_{(s)}^-$ decay time is defined as

$$t_D = \frac{m_D \, \vec{L}' \cdot \vec{p}(D)}{p^2(D)}, \tag{3.6}$$

where m_D is the known value of the $D_{(s)}$ mass [19], $\vec{L}'$ is the vector between the B decay vertex and the D decay vertex and $\vec{p}(D)$ is the fully-reconstructed momentum of the $K^+ K^- \pi^-$ system. The measured value of $\Delta(D)$ combined with the known D^- lifetime [19] yields the world's most precise determination of the D_s^- lifetime. Also in this case the analysis method is validated directly on data with $B^0 \to D^- (\to K^+ K^- \pi^-) \mu^+ \nu X$ and $B^0 \to D^- (\to K^+ \pi^- \pi^-) \mu^+ \nu X$ decays.

This chapter is structured as follows. Section 3.2 describes the data samples used, with details on their selection. The expected sample composition, based on simulation studies of signal and background events, is presented in Section 3.3. Section 3.4 discusses the fits to the corrected B mass distribution and presents the resulting samples compositions. Section 3.5 and 3.6 presents the decay-time dependent fits used to determine $\Delta(D)$ and $\Delta(B)$, respectively. Finally, systematic uncertainties are evaluated in Sect. 3.8 and results are summarised in Section 3.9.

3.2 Data samples

The analysis uses the entire data set collected by LHCb during Run I, consisting of approximately $3.0 \, \text{fb}^{-1}$ of integrated luminosity.

3.2.1 Pre-selection (stripping)

To reconstruct the $B_s^0 \to D_s^- (\to K^+ K^- \pi^-) \mu^+ \nu X$, $B^0 \to D^- (\to K^+ K^- \pi^-) \mu^+ \nu X$ and $B^0 \to D^- (\to K^+ \pi^- \pi^-) \mu^+ \nu X$ decays, the $D_{(s)}^-$ candidates are first reconstructed from three tracks ($K^+ K^- \pi^-$ or $K^+ \pi^- \pi^-$) originating from the same vertex and then combined with a muon candidate originating from a common displaced vertex. In the $K^+ K^- \pi^-$ reconstruction channel, the $K^+ K^-$ pair is further required to come from the $\phi(1020)$ resonance.

Selected events are predominantly triggered by the L0 Muon line, as the muon is the particle of the decay that is the most efficiently identified. Various Hlt trigger lines are required, as discussed in Section 3.2.2.

Collected data must first satisfy a loose selection, aimed at producing a sample of reduced size and requiring less time and computational power to work with. This pre-selection is

known as stripping. Candidate $B_s^0 \to D_s^-(\to K^+K^-\pi^-)\mu^+\nu X$ and $B^0 \to D^-(\to K^+K^-\pi^-)\mu^+\nu X$ decays are reconstructed from the b2DsPhiPiMuXB2DMuNuX line of Stripping20r{0,1}p3; $B^0 \to D^-(\to K^+\pi^-\pi^-)\mu^+\nu X$ candidates are reconstructed using the b2DpMuXB2DMuNuX line of Stripping20r{0,1}p0. The details of this first selection are summarised in Table 3.1 and are described below.

- Minimum momentum p and transverse momentum p_T are required to reduce low-momentum combinatorial background.

- The vertex χ^2 describes the quality of the decay vertex fit, ensuring that the tracks come from the same vertex.

- The χ^2_{IP} of the impact parameter (IP) with respect to the pp collision (the primary vertex, PV) is defined as the difference between the vertex χ^2's of a fit where this track is included and a fit where this track is excluded. This criterion ensures the tracks do not come directly from the PV, but rather from another source: the B or the D meson.

- The track χ^2 (per ndf, number of degrees of freedom) establishes the quality of the track reconstruction.

- A track is called a ghost if it is wrongly reconstructed from random hits in the tracking stations; the track ghost probability requirement greatly removes such tracks.

- PID requirements use the particle identification system to estimate how likely the particle was identified properly.

- A mass veto appears in the $K^+K^-\pi^-$ channel to ensure that the two kaons come from the ϕ resonance, reducing thus the $D_{(s)}^-$ combinatorial background.

- The D meson χ^2 separation from the PV ensures that the D decay vertex is not too close of the PV, where the probability to reconstruct a D meson from random tracks is higher.

- The cosine of the angle between the reconstructed momentum of the D or B candidate and its flight distance as defined by the vector from its origin vertex (the B decay vertex for the D, the PV for the B) to its decay vertex is called the DIRA. This value is very close to one for signal decays, while it may be smaller for partially reconstructed events where some tracks are not properly reconstructed.

- The mass of the $D_{(s)}^-$ and $B_{(s)}^0$ are loosely constrained. The selection cut for the B^0 mass of the $K^+\pi^-\pi^-$ channel is somewhat tight, but impossible to change without generating many new simulation events. As the $K^+\pi^-\pi^-$ channel is only a control channel, we decided to keep this requirement.

- The distance along the beam direction (z) between the D and B decay vertices, $\nu_z(D) - \nu_z(B)$, should be larger than zero if the D flies in the same direction as the B. A negative difference might be due to the resolution of the detector, or because the D comes from another vertex.

Quantity	$K^+ K^- \pi^-$ requirement (b2DsPhiPiMuXB2DMuNuX)	$K^+ \pi^- \pi^-$ requirement (b2DpMuXB2DMuNuX)
$p_T(\mu)$	> 600 MeV/c	> 800 MeV/c
$p_T(K)$, $p_T(\pi)$	> 150 MeV/c	> 300 MeV/c
$p(\mu)$	–	> 3.0 GeV/c
$p(K)$, $p(\pi)$	> 1.5 GeV/c	> 2.0 GeV/c
Minimum $\chi^2_{IP}(\mu, \pi, K)$	> 4.0	> 9.0
Track $\chi^2/\mathrm{ndf}(\mu, \pi, K)$	-	< 4.0
Ghost probability (μ, π, K)	< 0.5	< 0.5
PIDmu(μ)	> 0.0	> 0.0
PIDK(K)	> 0.0	> 4.0
PIDK(π)	< 20.0	< 10.0
$m(K^+ K^-)$	$\in [979.455, 1059.455]$ MeV/c^2	–
D daughters' $\sum p_T$	–	> 1.8 GeV/c
D vertex χ^2/ndf	< 8.0	< 6.0
D χ^2/ndf separation from PV	> 20	> 100
D DIRA	> 0.99	> 0.99
$m(D^-_{(s)})$	$\in [1789.62, 2048.49]$ MeV/c^2	$\in [1789.62, 1949.62]$ MeV/c^2
B vertex χ^2/ndf	< 20.0	< 6.0
B DIRA	> 0.99	> 0.999
$m(D_{(s)}\mu)$	$\in [0.0, 1000.0]$ GeV/c^2	$\in [2.5, 6.0]$ GeV/c^2
$v_z(D) - v_z(B)$	> -0.3 mm	> 0.0 mm

Table 3.1 – Summary of stripping selections for (left) $K^+ K^- \pi^-$ and (right) $K^+ \pi^- \pi^-$ samples.
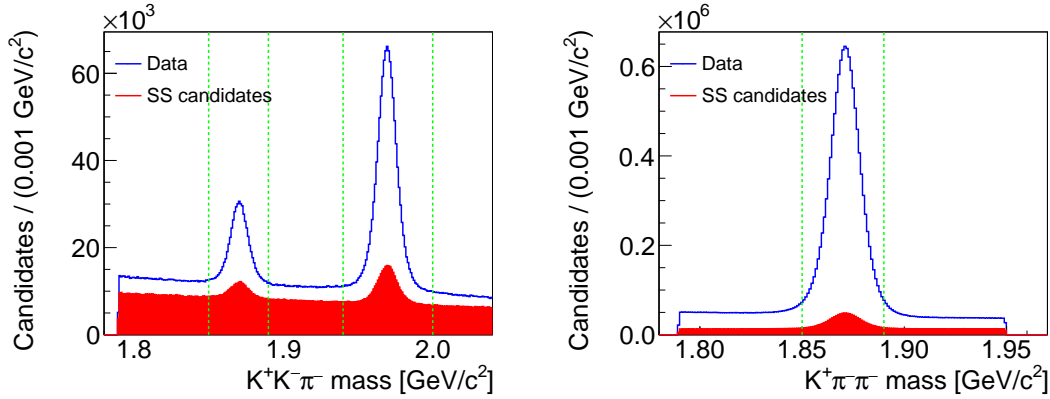
Figure 3.1 – Distributions of (left) $K^+K^-\pi^-$ and (right) $K^+\pi^-\pi^-$ masses for the candidates reconstructed by the pre-selection for opposite-sign and same-sign data.

Beauty meson candidates where the muon and the charmed meson candidates have the same charge are also reconstructed. Such *same-sign* (SS) candidates are used to study the combinatorial background formed by a real D meson associated to a random muon. They are compared to opposite-sign (OS) events, where the charge differs.

Figure 3.1 shows the $D_{(s)}$ mass distributions of the reconstructed candidates. Signal candidate yields equal 2.23×10^6 (1.13×10^6) $D^- \to K^+K^-\pi^-$, 4.50×10^6 (1.66×10^6) $D_s^- \to K^+K^-\pi^-$, and 17.53×10^6 (1.61×10^6) $D^- \to K^+\pi^-\pi^-$ for opposite-sign (same-sign) and are clearly distinguishable from smooth backgrounds. Signal $B_s^0 \to D_s^-(\to K^+K^-\pi^-)\mu^+\nu X$ and $B^0 \to D^-(\to K^+K^-\pi^-)\mu^+\nu X$ candidates are formed by restricting the $K^+K^-\pi^-$ mass in the ranges [1850, 1890] MeV/c^2 and [1940, 2000] MeV/c^2, respectively. Cross-contamination from D_s^- in the D^- mass range and vice versa is less than 0.1%, as estimated from simulation. Control $B^0 \to D^-(\to K^+\pi^-\pi^-)\mu^+\nu X$ candidates are also restricted in the $K^+\pi^-\pi^-$ mass range [1850, 1890] MeV/c^2. Figure 3.2 shows the $K^+K^-\pi^-\mu^+$ and $K^+\pi^-\pi^-\mu^+$ invariant mass, represented as the $D_{(s)}\mu$ invariant mass and corrected B mass distributions (only a part of the full sample is shown as an example).

In all plots and mass ranges the same-sign candidates are fewer than opposite-sign candidates. The $D_{(s)}\mu$ invariant mass shows a large, broad enhancement in the 3–5 GeV/c^2 range as expected in a region enriched in b-hadron decays. This is also consistent with the increased local discrepancy between opposite-sign and same-sign distributions. At higher masses, the differences in yield between same- and opposite-sign samples reduce and both distributions decrease roughly exponentially, which is consistent with a region dominated by combinatorial background. The similarity of same-sign and opposite-sign distributions in the 5.5–8.5 GeV/c^2 region suggests that the same-sign sample can be used to estimate the combinatorial component under the B signal 3–5 GeV/c^2 range. A small narrow enhancement at $D_{(s)}\mu$ invariant mass of approximately 5.3 GeV/c^2, corresponding to fully-reconstructed $B_{(s)}^0$ decays, is also seen. The corrected mass distributions show qualitatively similar features but the enhancement in the B-signal region is narrower due to the kinematic correction that reduces the B mass smearing.
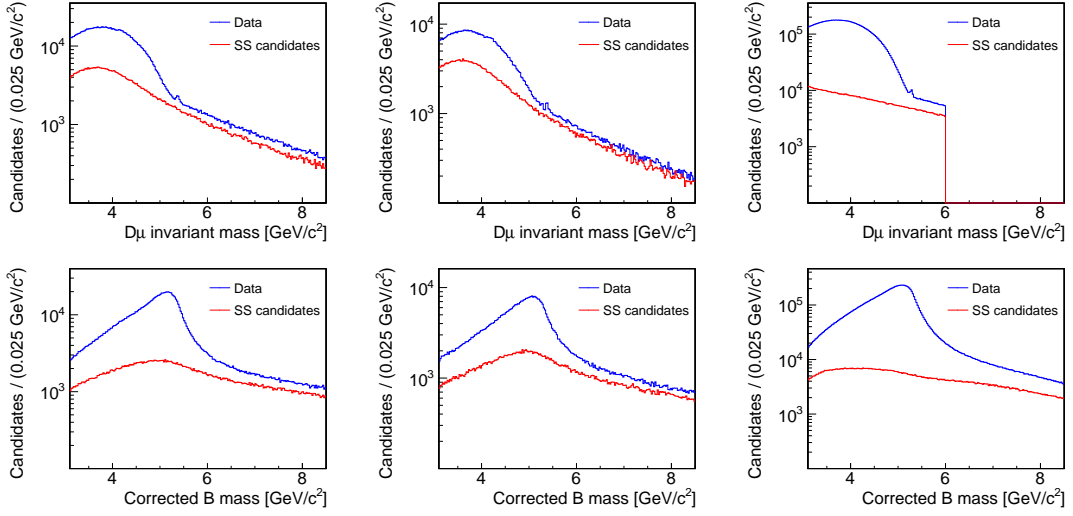
Figure 3.2 – Distributions of (top) $D_{(s)}\mu$ and (bottom) corrected B mass for (left) $B_s^0 \to D_s^- (\to K^+ K^- \pi^-)\mu^+ \nu X$, (centre) $B^0 \to D^- (\to K^+ K^- \pi^-)\mu^+ \nu X$ and (right) $B^0 \to D^- (\to K^+ \pi^- \pi^-)\mu^+ \nu X$ candidates reconstructed after stripping in 2012 magnet-down data. The narrower $D\mu$-mass range for the $B^0 \to D^- (\to K^+ \pi^- \pi^-)\mu^+ \nu X$ case is driven by the tighter stripping selection. Plots from 2011 and magnet-up data show similar features.

3.2.2 Offline selection

After the pre-selection, candidates are first filtered according to trigger information. We require each event to be consistent with being triggered by particles belonging to thhe signal candidates (Trigger On Signal, TOS).

- At the L0 level, only the `Muon` trigger is considered. It requires a minimum muon p_T of about 1.7 GeV/c and a limited amount of tracks in the SPD.

- At the Hlt1 level, the muon is required to trigger one of three trigger lines: `Hlt1TrackAllL0`, `Hlt1TrackMuon` or `Hlt1SingleMuonHighPT`. In the two first lines, (transverse) momentum requirements and basic tracking are applied to a single detached particle; any object for `Hlt1TrackAllL0` and a muon for `Hlt1TrackMuon`. The last line requires a single muon to be detected with large transverse momentum. Above 95% of candidates are selected by `Hlt1TrackMuon` and above 80% are selected by at least two Hlt1 lines.

- At the Hlt2 level, the B candidate is required to be selected by one of the three topological lines `Hlt2TopoMu{2,3,4}BodyBBDT`. These lines require 2, 3 or 4 lines to build a B candidate, one of them identified as a muon, and candidates are selected based on a multivariate selection, with input variables being: the sum of p_T's, minimum p_T, $D_{(s)}\mu$ and corrected B mass, track and vertex χ^2 and distance of closest approach between two tracks. The three lines are complementary and select between 60 and 90% of the candidates.

Details of each trigger line can be found in Ref. [70].

Quantity	$K^+K^-\pi^-$ requirement	$K^+\pi^-\pi^-$ requirement
ProbNNk(K)	> 0.2	> 0.2
ProbNNpi(π)	> 0.2	> 0.5
ProbNNmu(μ)	> 0.2	> 0.2
$p(K)$	$> 2\,\text{GeV}/c$	$> 3\,\text{GeV}/c$
$p(\pi)$	$> 2\,\text{GeV}/c$	$> 5\,\text{GeV}$
$p_T(K)$, $p_T(\pi)$	$> 300\,\text{MeV}/c$	$> 500\,\text{MeV}/c$
D vertex χ^2/ndf	< 6.0	< 6.0
$m(K^+K^-)$	$\in [1.008, 1.032]\,\text{GeV}/c^2$	$-$
$p_\perp(D)\,[\text{MeV}/c]$	$> 1500 + 1.1 \times (m_{\text{corr}}[\text{MeV}/c^2] - 4500)$	
t_D	$> 0.1\,\text{ps}$	
m_{corr}	$[3000, 8500]\,\text{MeV}/c^2$	
$m(D_{(s)}^-)$	$\in [1.85, 1.89]\,\text{GeV}/c^2$ (for B^0) $\in [1.94, 2.00]\,\text{GeV}/c^2$ (for B_s^0)	$\in [1.85, 1.89]\,\text{GeV}/c^2$
$m(D_{(s)}^-\mu^+)$	$> 3.1\,\text{GeV}/c^2$ $\notin [5.200, 5.400]\,\text{GeV}/c^2$ (for B^0) $\notin [5.280, 5.480]\,\text{GeV}/c^2$ (for B_s^0)	$> 3.1\,\text{GeV}/c^2$ $\notin [5.200, 5.400]\,\text{GeV}/c^2$
$m(\mu^+\mu^-)$	$\notin [3.040, 3.160]\,\text{GeV}/c^2$ $\notin [3.635, 3.735]\,\text{GeV}/c^2$	
$m(Kp\pi)$	$\notin [2.260, 2.310]\,\text{GeV}/c^2$	

Table 3.2 – Summary of offline selection criteria for the (left) $K^+K^-\pi^-$ and (right) $K^+\pi^-\pi^-$ samples. See text for motivations on the various mass vetoes.
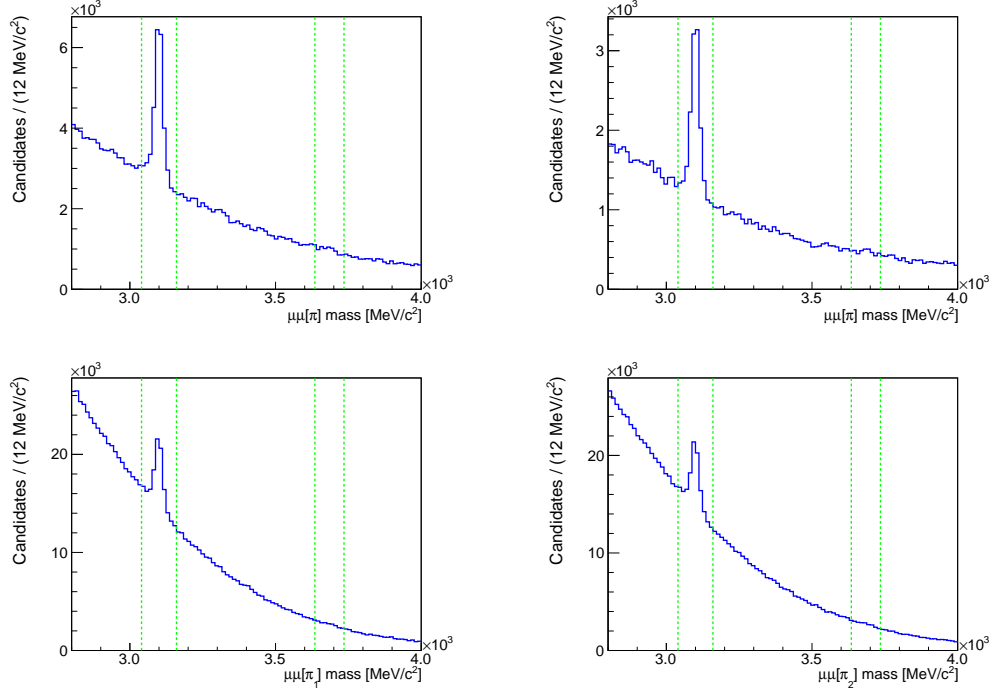
Figure 3.3 – Dimuon mass reconstructed by assigning the muon mass to a charged particle originally identified as a pion for (top left) $B_s^0 \to D_s^-(\to K^+K^-\pi^-)\mu^+\nu X$, (top right) $B^0 \to D^-(\to K^+K^-\pi^-)\mu^+\nu X$ and (bottom) $B^0 \to D^-(\to K^+\pi^-\pi^-)\mu^+\nu X$ candidates after the stripping. The vertical lines enclose the $\psi(1S)$ and $\psi(2S)$ mass regions, which are vetoed.

The resulting candidates are then required to satisfy the offline selection summarised in Table 3.2. The selection aims at reducing the background under the $D_{(s)}$ peak and minimising differences in yields and shapes between SS and OS data in the sideband of the $D_{(s)}\mu$ invariant mass. The goal is to use the SS sample as a reliable control sample to study the features of combinatorial background in the corrected B mass fit. This process is made more complicated in the $K^+\pi^-\pi^-$ sample by a stripping requirement at 6 GeV/c^2 on the $D\mu$ mass (see Figure 3.2, top-right plot).

Known sources of backgrounds from misreconstructed decays are suppressed in the following way. $B_s^0 \to \psi(\to \mu^+\mu^-)\phi(\to K^+K^-)$ decays (Fig. 3.3), where ψ indicates either the $1S$ or the $2S$ charmonium state, and where one of the muons from the ψ is misidentified as a pion, are removed by vetoing the corresponding regions in dimuon mass computed after assigning the muon mass to the charged particle originally identified as a pion. $\Lambda_b^0 \to \Lambda_c^+(\to pK^-\pi^+)\mu^-\nu X$ decays (Fig. 3.4) where the proton is misidentified as a kaon (for $K^+K^-\pi^-$) or a pion (for $K^+\pi^-\pi^-$) are also removed by a veto on the $pK\pi$ mass computed with similar mass reassignments. Backgrounds from fully-reconstructed $B_{(s)}^0 \to D_{(s)}^-\pi^+$ are removed by vetoing the corresponding region in $D_{(s)}\mu$ invariant mass.

Requirements on (transverse) momenta and on particle identification of the D daughters help to reduce further the non-D background. Most of these are tightening the pre-selection criteria. We also tighten the requirements on quantities capable to increase the signal-to-
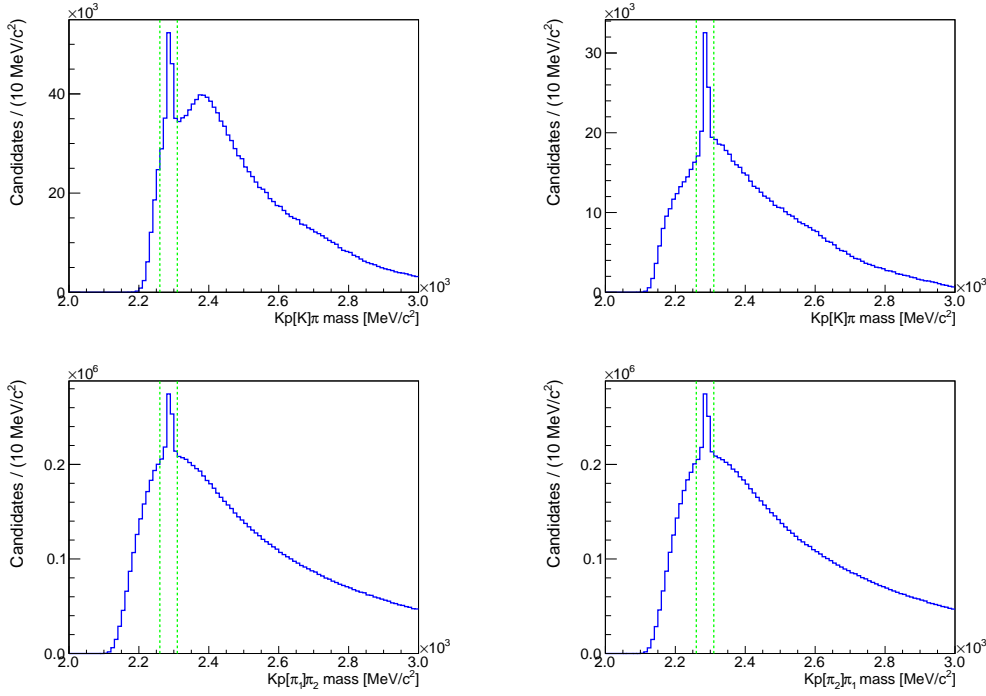
Figure 3.4 – $Kp\pi$ mass reconstructed by assigning the proton mass to a charged particle originally identified as a kaon (for $K^+K^-\pi^-$ candidates) or a pion (for $K^+\pi^-\pi^-$ candidates) for (top left) $B_s^0 \to D_s^-(\to K^+K^-\pi^-)\mu^+\nu X$, (top right) $B^0 \to D^-(\to K^+K^-\pi^-)\mu^+\nu X$ and (bottom) $B^0 \to D^-(\to K^+\pi^-\pi^-)\mu^+\nu X$ candidates after the stripping. The vertical lines enclose the Λ_b^0 mass region, which is vetoed.

background ratio while maintaining sufficient sample size, like particle-identification criteria ProbNNX, with X = μ, π, K. These variables estimate the probability that a particle is identified correctly, mainly with data from the RICH, calorimeters and muon chambers.

Backgrounds from decays of a b hadron into two charm hadrons, of which one peaks in $D_{(s)}$ mass and the other decays semileptonically, contribute at lower corrected B masses. Such backgrounds, described in detail in Sect. 3.3.2 with simulation, are suppressed by a requirement on the component of the D candidate momentum transverse to the B flight distance direction, $p_\perp(D)$, as a function of the corrected B mass: $p_\perp(D)[\text{MeV}/c] > 1500 + 1.1 \times (m_{\text{corr}}[\text{MeV}/c^2] - 4500)$. Different linear requirements and other shapes have been implemented in order to reduce the double-charmed background in this two-dimensional space, but the simulation estimates that this requirement, shown in Fig. 3.5, is optimal and roughly halves these backgrounds while retaining about 90% of the signal. As far as we know, this is the first time such a selection has been made and it has already spread to other measurements with semileptonic decays at LHCb.

A requirement on the decay time of the D candidate, $t_D > 0.1$ ps, is applied to ensure equal decay time distributions of the D^- and D_s^- mesons and thus the flattening of the ratio of the B_s^0 and B^0 decay-time acceptance, after the reweighting of the D_s^- decay time distribution described in Sect. 3.6.2.
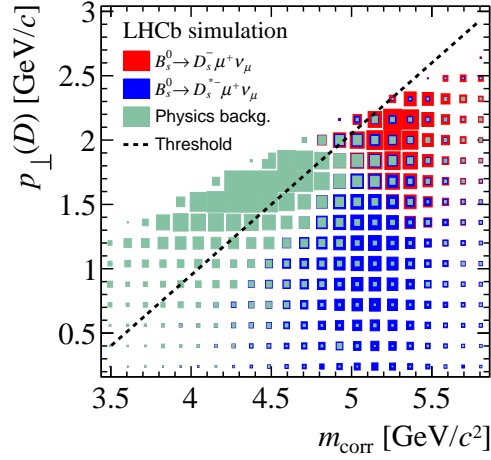
Figure 3.5 – Two-dimensional distribution of $p_\perp(D)$ and the corrected B mass in simulations for the different components expected to contribute in the B_s^0 sample, as described in Sect. 3.3. The dotted line represents the option finally chosen and events above the line are removed.
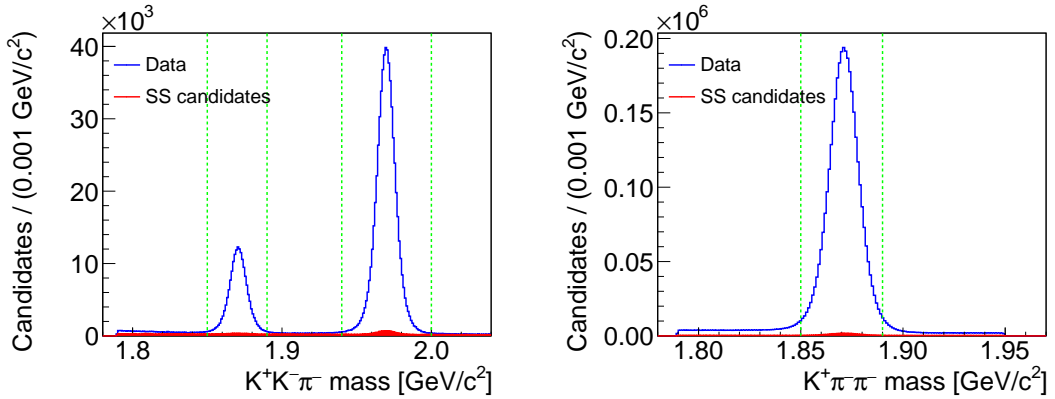
Figure 3.6 – Distributions of (left) $K^+K^-\pi^-$ and (right) $K^+\pi^-\pi^-$ masses for the candidates passing the final selection.

Figures 3.6 and 3.7 show the resulting $K^+K^-\pi^-/K^+\pi^-\pi^-$ and $KK\pi\mu/K\pi\pi\mu$ mass distributions, respectively. A total of 4.68×10^5 $B_s^0 \to D_s^-(\to K^+K^-\pi^-)\mu^+\nu X$ signal candidates meet the final selection criteria; 1.40×10^5 B^0 candidates meet the $K^+K^-\pi^-$ selection and 2.61×10^6 B^0 candidates, the $K^+\pi^-\pi^-$ selection. Combinatorial background is largely reduced with respect to the pre-selection and SS and OS distributions are much closer to each other away from the D signal peaks.

Figure 3.7 shows the comparison between OS and SS $KK\pi\mu$ and $K\pi\pi\mu$ distributions for candidates restricted to the D signal region, $1.85 < m(KK\pi/K\pi\pi) < 1.89$ GeV/c^2 for D^- and $1.94 < m(KK\pi) < 2.00$ GeV/c^2 for D_s^-. Figure 3.8 shows the same distributions for events in the D mass sidebands: $1.80 < m(KK\pi) < 1.85$ GeV/c^2, $1.89 < m(KK\pi) < 1.94$ GeV/c^2 and $2.00 < m(KK\pi) < 2.03$ GeV/c^2 for the $K^+K^-\pi^-$ samples; $1.80 < m(K\pi\pi) < 1.85$ GeV/c^2 and $1.89 < m(K\pi\pi) < 1.95$ GeV/c^2 for the $K^+\pi^-\pi^-$ sample. The agreement, in shape and normalisation, between the OS and SS distributions at high $D_{(s)}\mu$ mass is good in the D mass
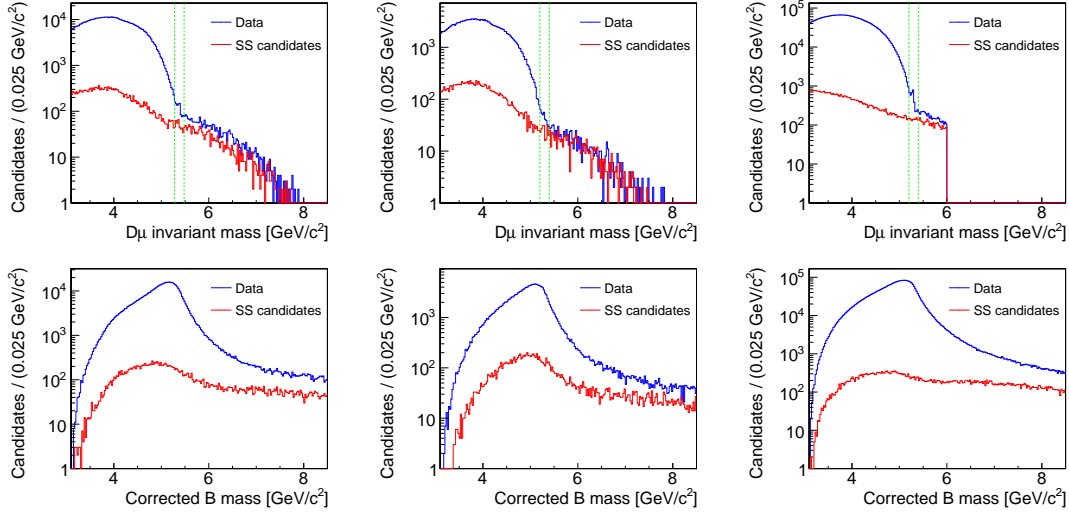
Figure 3.7 – Distributions of (top) $D_{(s)}\mu$ and (bottom) corrected B mass for (left) $B_s^0 \to D_s^-(\to K^+K^-\pi^-)\mu^+\nu X$, (centre) $B^0 \to D^-(\to K^+K^-\pi^-)\mu^+\nu X$ and (right) $B^0 \to D^-(\to K^+\pi^-\pi^-)\mu^+\nu X$ candidates passing the final selection. The vertical lines enclose the regions removed by the $D_{(s)}\mu$ veto.

sidebands and for $B^0 \to D^-(\to K^+K^-\pi^-)\mu^+\nu X$. Residual normalisation differences remain in the $B_s^0 \to D_s^-(\to K^+K^-\pi^-)\mu^+\nu X$ signal region (Fig. 3.7, top-left plot), presumably due to unaccounted physics backgrounds, although shapes are very similar. Given that the normalisation of the SS data is not fixed in any step of the analysis, we believe this level of agreement is sufficient to consider reliable the SS candidates distribution as a robust data-based model for the combinatorial background and include the effect of the residual differences in the systematic uncertainties.
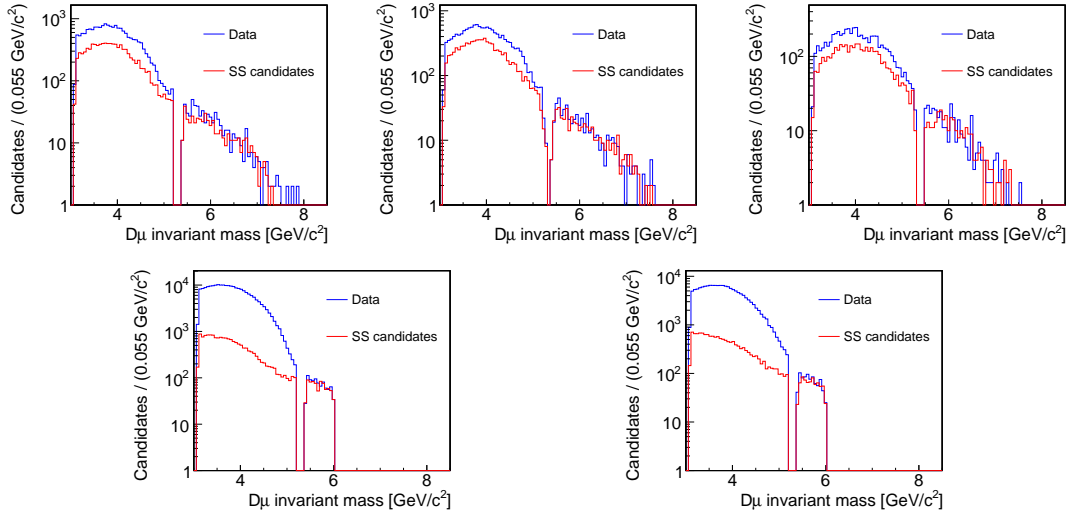
Figure 3.8 – $D_{(s)}\mu^+$ mass distribution for OS and SS candidates restricted to the D mass-sidebands. Top panels show candidates with $K^+K^-\pi^-$ mass (left) smaller than the D^- mass, (centre) comprised between the D^- and D_s^- mass and (right) larger than the D_s^- mass. Bottom panels show candidates with $K^+\pi^-\pi^-$ mass (left) smaller and (right) larger than the D^- mass.

3.3 Simulation and expected sample composition

Simulation is used to understand in detail all sources of b–hadron decays that contribute to the sample and model the relevant distributions used in the analysis. Simulated data goes through the same process of reconstruction and selection as the experimental data, following the path described in Section 2.2.4, before going through pre-selection (stripping) and offline selection.

Table 3.3 lists the simulated samples used, together with the number of candidates which correspond to the generated decays passing the final selection and the corresponding total efficiencies. In addition to the signal component and the two normalisation modes, the list includes decays contributing the main physics backgrounds (middle and bottom portions of Tab. 3.3). Each sample is split into up and down spectrometer magnet polarities and into 2011 and 2012 subsamples, in proportions similar to those present in data, except for the background samples, for which only 2012 conditions are simulated. Efficiencies include effects from generator level, stripping and offline selections. The $K^+ K^- \pi^-$ signal efficiency for selecting B^0 decays is lower than the efficiency for B_s^0 decays because topological triggers favour decays with closely spaced B and D vertices.

Sample	Candidates after selection	Efficiency [10^{-4}]
$B_s^0 \to D_s^- (\to K^+ K^- \pi^-) \mu^+ \nu X$	566419	7.05
$B^0 \to D^- (\to K^+ K^- \pi^-) \mu^+ \nu X$	290353	3.95
$B^0 \to D^- (\to K^+ \pi^- \pi^-) \mu^+ \nu X$	149131	8.49
$B_s^0 \to D_s^{(*)-} D_s^{(*)+}$	3037	1.98
$\Lambda_b^0 \to \Lambda_c^+ D_s^{(*)-} (\pi^0)$	3330	1.06
$B^+ \to D^{(*)0} D_s^{(*)+}$	2071	1.35
$B^0 \to D^{(*)-} D_s^{(*)+}$	1780	1.16
$B^- \to D_0^{*0}(2400)(\to D_s^{(*)+} K^+) \mu^- \nu$	6447	2.23
$\overline{B}^0 \to D_0^{*-}(2400)(\to D_s^{(*)+} K_s^0) \mu^- \nu$	6236	2.09
$B_s^0 \to D^0 D_s K$	4636	1.61
$B^+ \to D^- (\to K^+ K^- \pi^-) \pi^+ \mu^+ \nu X$	44734	2.25
$B^+ \to D^- (\to K^+ \pi^- \pi^-) \pi^+ \mu^+ \nu X$	18226	4.12

Table 3.3 – Samples of simulated data used in the analysis. Signal components are on the top, expected physics backgrounds for the B_s^0 sample are in the middle, and expected B^+ backgrounds to the B^0 samples are at the bottom.

3.3.1 Composition of the B_s^0 and B^0 signal samples

Table 3.4 lists the details of the configurations used to generate inclusive $B_s^0 \to D_s^- \mu^- \nu X$ and $B^0 \to D^- \mu^+ \nu X$ decays. The internal composition of the simulated B^0 sample is expected to mirror adequately the composition observed in data, as the generation parameters for the B^0 sample are tuned, by default, to reproduce the large body of experimental

information on these decays. In the B_s^0 case, it is less straightforward, since many of the relevant branching fractions are yet unknown and the simulation relies on theoretical assumptions that may deviate from the actual B_s^0 dynamics. We therefore resort to data by fitting the corrected B mass distribution with a composition of corrected B mass shapes for the signal and different background channels obtained from simulation, where the fractions of each channel are left as free parameters and determined in the fit (Sec. 3.4.2). This method is validated on the B^0 sample, by comparing the fractions obtained from the fit and known branching fractions. For the purpose of such fit of composition, the simulated events of inclusive $B_s^0 \to D_s^-(\to K^+K^-\pi^-)\mu^+\nu X$, $B^0 \to D^-(\to K^+K^-\pi^-)\mu^+\nu X$ and $B^0 \to D^-(\to K^+\pi^-\pi^-)\mu^+\nu X$ decays are each separated into four disjoint categories as reported in Table 3.5: exclusive $B_{(s)}^0 \to D_{(s)}^-\mu^+\nu$ decays; $B_{(s)}^0 \to D_{(s)}^{*-}\mu^+\nu$ decays, with $D_{(s)}^{*-}$ decaying into $D_{(s)}$ and a photon or a neutral pion; semimuonic decays involving higher D resonances ($D_{(s)}^{**-}$), which will be referred to as $B_{(s)}^0 \to D_{(s)}^-\mu^+\nu X$ decays; inclusive semitauonic decays channels, with the τ decaying to a muon and neutrinos, which will be referred to as $B_{(s)}^0 \to D_{(s)}^-\tau^+\nu X$ decays. This table lists the fractions corresponding to each category for each of the three samples. Note that the two B^0 samples do not necessarily have a compatible composition, as the selections are very different. The two first categories will later be considered as the signal, while the two others will be considered as physics backgrounds, along with the other decays discussed in the following section.

3.3.2 Physics backgrounds

Backgrounds from real b-hadron decays that peak in the $D_{(s)}$ mass distribution are not accounted for by the SS background and need to be treated separately in the corrected B mass fit. These include decays of b-hadrons to pairs of charm mesons and semileptonic decays otherwise similar to the signal, but with an extra hadron in the final state. We estimate the fractions of these decays with respect to signal using

$$\frac{f_{\text{bkg}}}{f_{\text{sig}}} = \frac{\mathcal{B}(B \to DD, DK\mu\nu, ...)\mathcal{B}(D \to \mu X)\mathcal{B}(D_{(s)} \to \phi\pi, \phi \to KK)}{\mathcal{B}(B_{(s)} \to D_{(s)}\mu X)\mathcal{B}(D_{(s)} \to KK\pi)} \frac{\epsilon_{\text{bkg}}}{\epsilon_{\text{sig}}} \frac{f_{u/d/s/\Lambda}}{f_{d/s}}, \quad (3.7)$$

where $\mathcal{B}$ are the known branching fractions [19]; $\epsilon_{\text{bkg}}/\epsilon_{\text{sig}}$ is the efficiency ratio, defined as the ratio of the fractions of generated events that meet the full selection[2]; and f are b-hadron production fractions. The total branching fraction is the product of the branching fractions for the b-hadrons decay, the semileptonic D decay, depending on the flavour of the charm meson and, for $B \to DD$ decays, $D_s^+ \to \phi(\to K^+K^-)\pi^+$, as these background decays are forced to proceed through an intermediate ϕ meson. The input branching fractions are either experimentally known or estimated from measurements of decays with a similar topology. We use ratios of production fractions $f_u/f_s = f_d/f_s = 3.86 \pm 0.22$ and $f_\Lambda/f_s = 2.34 \pm 0.31$ based on LHCb determinations [71, 72].

Table 3.6 lists the dominant physics backgrounds expected in the $B_s^0 \to D_s^-(\to K^+K^-\pi^-)\mu^+\nu X$

---

[2]The efficiency ratios here differ from ratios that can be calculated from Tab. 3.3, as these ratios include the effect of the B_s^0 sample reweighting for the $\Delta(B)$ measurement described in Sect. 3.6.2; in the $\Delta(D)$ measurement these ratios are evaluated without the B_s^0 reweighting and corresponds to those from Tab. 3.3.

sample, grouped in four categories: $B \to DD$, $B \to DK\mu\nu$, $B \to DDK$ and Λ_b^0 decays. The estimated contamination fractions with respect to the signal are also shown. Uncertainties are dominated by the $\approx 30\%$ relative uncertainty on the signal branching fraction. In the fit of the composition we consider the two main components of the $B \to DD$ modes and the two $B \to DK\mu\nu$ modes. The other components are considered only in the systematic uncertainties (Sec. 3.8.3). The contribution of $\Lambda_b^0 \to D_s^+ \Lambda^0 \mu^- \nu$ decays cannot be estimated reliably as the branching ratios of this decay is unknown; we produce a sample of these decays at generator level, from which we compute the corrected mass. This is later used to build a mass template of this background to include in the mass fit for computing an extra systematic uncertainty (Sec. 3.8.3).

For the two B^0 samples (Tab. 3.7), the only relevant physics background is $B^+ \to D^- \pi^+ \mu^+ \nu X$. Its contamination fraction relative to the B^0 signal is found to be $(6.02 \pm 1.12)\%$ and $(5.12 \pm 0.95)\%$ for the $K^+ K^- \pi^-$ and $K^+ \pi^- \pi^-$ samples, respectively. Decays of b-hadron to pairs of charm hadrons are estimated assuming similar selection efficiencies to the ones in Tab. 3.6; these backgrounds are expected to have a negligible contribution and are therefore ignored. The branching ratio of the $\Lambda_b^0 \to D^- n \mu^+ \nu$ decays is unknown; by plugging in the fit of the composition a mass template derived from simulation with floating normalisation, we found the yield of this background to be consistent with zero, and thus we neglect it in the rest of the analysis.

Process	$\mathscr{B}$ [%]	Decay model
$B_s^0 \to D_s^- \mu^+ \nu$	2.1000	`HQET2 1.17 1.074`
$B_s^0 \to D_s^{*-}(\to D_s^- X)\mu^+ \nu$	5.1000	`HQET2 1.16 0.921 1.37 0.845` †
$B_s^0 \to D_{s0}^{*-}(\to D_s^{(*)-}X)\mu^+ \nu$	0.7000	`ISGW2`
$B_s^0 \to D_{s1}^-(\to D_s^{(*)-}X)\mu^+ \nu$	0.4000	`ISGW2`
$B_s^0 \to D_{s1}^{\prime -}(\to D_s^{(*)-}X)\mu^+ \nu$	0.4000	`ISGW2`
$B_s^0 \to D_s^- \tau^+(\to \mu^+ \nu\nu)\nu$	0.138	`ISGW2`
$B_s^0 \to D_s^{*-}(\to D_s^{(*)-}X)\tau^+(\to \mu^+ \nu\nu)\nu$	0.2770	`ISGW2`
$B_s^0 \to D_{s0}^{*-}(\to D_s^{(*)-}X)\tau^+(\to \mu^+ \nu\nu)\nu$	0.0310	`ISGW2`
$B_s^0 \to D_{s1}^{\prime -}(\to D_s^{(*)-}X)\tau^+(\to \mu^+ \nu\nu)\nu$	0.0310	`ISGW2`
$B^0 \to D^- \mu^+ \nu$	2.1700	`HQET2 1.18 1.074`
$B^0 \to D^{*-}(\to D^- X)\mu^+ \nu$	1.6182	`HQET2 1.20 0.908 1.426 0.818` †
$B^0 \to D_1^-(\to D_{(0)}^* X)\mu^+ \nu$	0.1848	`ISGW2`
$B^0 \to D_2^{*-}(\to D_{(0)}^{(*)} X)\mu^+ \nu$	0.1652	`ISGW2`
$B^0 \to D_0^{*-}(\to D^{(*)-}X)\mu^+ \nu$	0.1436	`ISGW2`
$B^0 \to D^- \pi^+ \pi^- \mu^+ \nu$	0.1197	`PHSP`
$B^0 \to D^{*-}(\to D^- X)\pi^+ \pi^- \mu^+ \nu$	0.0902	`PHSP`
$B^0 \to D_1^{\prime -}(\to D^{(*)-}X)\mu^+ \nu$	0.0616	`ISGW2`
$B^0 \to D^- \pi^0 \pi^0 \mu^+ \nu$	0.0294	`PHSP`
$B^0 \to D^{*-}(\to D^- X)\pi^0 \pi^0 \mu^+ \nu$	0.0237	`PHSP`
$B^0 \to D^- \pi^0 \mu^+ \nu$	0.0198	`GOITY_ROBERTS`
$B^0 \to D^{*-}(\to D^- X)\pi^0 \mu^+ \nu$	0.0149	`GOITY_ROBERTS`
$B^0 \to D^- \tau^+(\to \mu^+ \nu\nu)\nu$	0.1910	`ISGW2`
$B^0 \to D^{*-}(\to D^- X)\tau^+(\to \mu^+ \nu\nu)\nu$	0.0841	`ISGW2`
$B^0 \to D_2^{*-}(\to D_{(0)}^{(*)} X)\tau^+(\to \mu^+ \nu\nu)\nu$	0.0110	`ISGW2`
$B^0 \to D_1^-(\to D_{(0)}^* X)\tau^+(\to \mu^+ \nu\nu)\nu$	0.0087	`ISGW2`
$B^0 \to D_0^{*-}(\to D^{(*)-}X)\tau^+(\to \mu^+ \nu\nu)\nu$	0.0069	`ISGW2`
$B^0 \to D_1^{\prime -}(\to D^{(*)-}X)\tau^+(\to \mu^+ \nu\nu)\nu$	0.0053	`ISGW2`

Table 3.4 – Processes contributing to the simulated samples of inclusive (top) $B_s^0 \to D_s^- \mu^- \nu X$ and (bottom) $B^0 \to D^- \mu^+ \nu X$ decays. Branching fractions and decay models used in generation are also reported.

†Because of a bug in generation, different `HQET(2)` parameters have been used for these two decays, but the samples have been reweighing accordingly. The systematics assigned to the model of the $B_s^0 \to D_s^{*-}(\to D_s^- X)\mu^+ \nu$ model are much larger than any possible remaining effect.

Process	Relative fraction [%]		
	B_s^0	B^0 ($K^+K^-\pi^-$)	B^0 ($K^+\pi^-\pi^-$)
$B_{(s)}^0 \to D_{(s)}^- \mu^+ \nu$	26.04 ± 0.05	53.98 ± 0.14	54.35 ± 0.19
$B_{(s)}^0 \to D_{(s)}^{*-}(\to D_{(s)}^- X)\mu^+ \nu$	61.71 ± 0.07	38.37 ± 0.11	37.79 ± 0.16
$B_{(s)}^0 \to D_{(s)}^{**-}(\to D_{(s)}^{(*)-} X)\mu^+ \nu$	11.46 ± 0.03	6.73 ± 0.05	7.02 ± 0.07
$B_{(s)}^0 \to D_{(s)}^- \tau^+(\to \mu^+ \nu\nu)\nu X$	0.79 ± 0.01	0.91 ± 0.02	0.85 ± 0.02

Table 3.5 – Observed proportions of the various contributions to the inclusive simulated samples of $B_s^0 \to D_s^-(\to K^+K^-\pi^-)\mu^+\nu X$, $B^0 \to D^-(\to K^+K^-\pi^-)\mu^+\nu X$ and $B^0 \to D^-(\to K^+\pi^-\pi^-)\mu^+\nu X$ decays after the full selection.

Category	Decay	$\mathcal{B}$ [10^{-4}]	$\epsilon_{\rm bkg}/\epsilon_{\rm sig}$	$f_{q/\Lambda}/f_s$	$f_{\rm bkg}/f_{\rm sig}$ [%]
	$B^0 \to D^{(*)-}D_s^{(*)+}$	12.74 ± 1.60	0.174 ± 0.004	3.86 ± 0.22	1.08 ± 0.36
$B \to DD$	$B^+ \to D^{(*)0}D_s^{(*)+}$	11.36 ± 1.29	0.197 ± 0.005	3.86 ± 0.22	1.09 ± 0.36
	$B_s^0 \to D_s^{(*)-}D_s^{(*)+}$	12.17 ± 3.93	0.281 ± 0.006	1	0.43 ± 0.19
$B \to DK\mu\nu$	$B^- \to D_s^{(*)+}K^-\mu^- X$	6.10 ± 1.00	0.319 ± 0.005	3.86 ± 0.22	0.95 ± 0.33
	$B^0 \to D_s^{(*)-}K_S^0\mu^+ X$	6.10 ± 1.00	0.299 ± 0.005	3.86 ± 0.22	0.89 ± 0.31
$B \to DDK$	$B_s^0 \to D^0 D_s^- K^+$	0.24 ± 0.09	0.236 ± 0.004	1	0.01 ± 0.01
	$B_s^0 \to D^- D_s^+ K^0$	0.17 ± 0.06	0.236 ± 0.004	1	0.01 ± 0.01
Λ_b^0	$\Lambda_b^0 \to \Lambda_c^+ D_s^{(*)+}(\pi^0)$	4.31 ± 1.69	0.156 ± 0.003	2.34 ± 0.31	0.20 ± 0.10
	$\Lambda_b^0 \to D_s^+ \Lambda^0 \mu^- \nu$	–	–	–	–

Table 3.6 – Background contributions for the $B_s^0 \to D_s^-(\to K^+K^-\pi^-)\mu^+\nu X$ sample grouped into four main categories. The signal branching fraction, $\mathcal{B}(B_s^0 \to D_s^- \ell^+\nu X) = (7.9 \pm 2.4)\%$, is the dominant source of uncertainty for the estimated relative fractions.

Category	Decay	$\mathcal{B}$ [10^{-4}]	$\epsilon_{\rm bkg}/\epsilon_{\rm sig}$	$f_{q/\Lambda}/f_d$	$f_{\rm bkg}/f_{KK\pi}$ [%]
B^+ ($K^+K^-\pi^-$)	$B^+ \to D^-\mu^+ X$	97 ± 16	0.569 ± 0.006	1	6.02 ± 1.12
B^+ ($K^+\pi^-\pi^-$)	$B^+ \to D^-\mu^+ X$	97 ± 16	0.485 ± 0.005	1	5.12 ± 0.95
	$B^0 \to D^- D_{(s)}^+ X$	4.60 ± 0.67	0.174 ± 0.004	1	0.09 ± 0.02
$B \to DD$	$B^0 \to D^- D^+ X$	0.14 ± 0.01	0.174 ± 0.004	1	< 0.01
	$B_s^0 \to D^- D^+$	0.15 ± 0.04	0.281 ± 0.006	0.26 ± 0.02	< 0.01
	$B^- \to D^- D^0$	0.10 ± 0.01	0.197 ± 0.005	1	< 0.01
Λ_b^0	$\Lambda_b^0 \to \Lambda_c^+ D^- X$	0.09 ± 0.04	0.156 ± 0.003	0.60 ± 0.08	< 0.01
	$\Lambda_b^0 \to D^- n\mu^+ \nu$	–	–	–	–

Table 3.7 – Background contributions for the $B^0 \to D^-(\to K^+K^-\pi^-)\mu^+\nu X$ and $B^0 \to D^-(\to K^+\pi^-\pi^-)\mu^+\nu X$ samples.

3.4 Fit of sample composition

A binned least-squares fit to the corrected B mass distribution is used to discriminate signal from backgrounds and determine the signal composition in terms of the four event categories defined in Table 3.5. Mass shapes are represented by histogram templates from simulation for signal components and background components from other b-hadron decay modes, while the combinatorial background is modelled using SS data. The fit minimises the following χ^2-like variable, which also includes an uncertainty due to the limited size of the simulation samples, allowing for Poissonian fluctuations in each bin:

$$\chi^2 = \sum_i^{\text{bins}} \frac{[n_i - p_i(\theta)]^2}{\sigma_{n_i}^2 + \sigma_{p_i}^2(\theta)}, \tag{3.8}$$

where n_i (p_i) is the number of observed (predicted) data candidates in the mass bin i, σ_{n_i} (σ_{p_i}), its statistical uncertainty and θ, a set of known and unknown parameters. The number of predicted candidates is

$$p_i = N \sum_j^{n_c} f_j \, h_{ji},$$

where f_j is the fraction of the component j (which are n_c in total) with mass template h_j, whose contribution to mass bin i is h_{ji} events. Templates are normalised to unity in the mass range of the fit and $\sum_j^{n_c} f_j = 1$. The parameter N is an overall normalisation corresponding to the total number of candidates predicted in the fit mass range and is fixed to the number of events in the data histogram. The set of fit parameters with respect to which Eq. (3.8) is minimised includes all fractions but one, $\theta = \{f_1, f_2, \ldots, f_{n_c-1}\}$. For weighted samples (see Section 3.6.2), n_i represents the sum of the weights in bin i and $\sigma_{n_i}^2$ is the sum of the squared weights.

The fit yields unbiased estimates with Gaussian uncertainties, as confirmed with the pseudo-experiments detailed in Sec. 3.7.

3.4.1 Fit to the B^0 data samples

In the fit of the B^0 samples we consider the four categories of signal decay chains given in Tab. 3.5, the $B^+ \to D^- \mu^+ \nu X$ background, and the combinatorial background. Other backgrounds are expected to contribute less than 0.1% of the signal yield (see Tab. 3.7), and are neglected.

Figure 3.9 shows the corrected B mass shapes for all the components used in the fit: they all differ enough to allow for separation, except for the $B^0 \to D^- \mu^+ \nu X$ and $B^+ \to D^- \mu^+ \nu X$ decays, which feature very similar distributions, because of their similar topologies. For these, a single template is obtained by summing the templates of the two components weighted according to their expected relative yields with respect to the signal, derived from the known branching fractions (see Tables 3.5 and 3.7); a single yield, determined by the fit, is associated to this combined template.
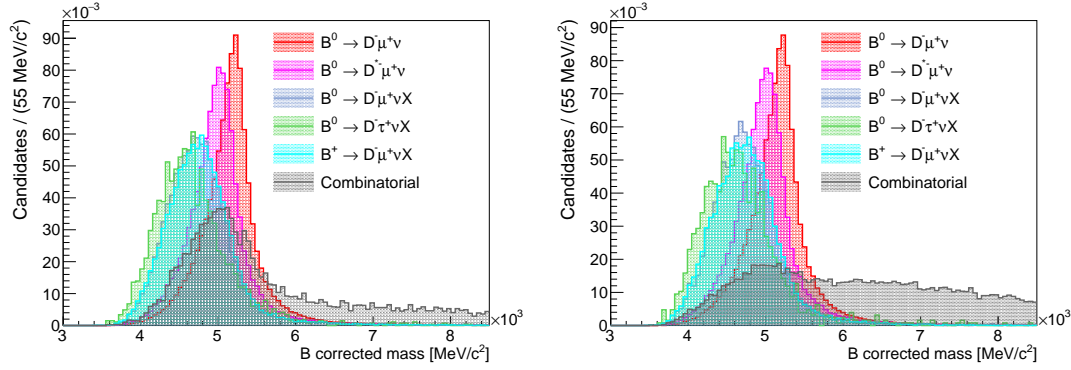
Figure 3.9 – Corrected B mass distributions of the components considered in the (left) $B^0 \rightarrow D^-(\rightarrow K^+K^-\pi^-)\mu^+\nu X$ and (right) $B^0 \rightarrow D^-(\rightarrow K^+\pi^-\pi^-)\mu^+\nu X$ fits.

Component	$K^+K^-\pi^-$		$K^+\pi^-\pi^-$	
	Fit fraction [%]	Prediction [%]	Fit fraction [%]	Prediction [%]
$B^0 \rightarrow D^-\mu^+\nu$	45.39 ± 0.67	45.83 ± 3.04	49.17 ± 0.53	50.47 ± 3.05
$B^0 \rightarrow D^{*-}\mu^+\nu$	31.16 ± 0.92	32.57 ± 0.99	31.24 ± 0.93	35.10 ± 0.96
$B^0/B^+ \rightarrow D^-\mu^+\nu X$	13.46 ± 0.47	10.83 ± 1.90	15.96 ± 1.22	11.27 ± 1.90
$B^0 \rightarrow D^-\tau^+\nu X$	(-1.1 ± 0.9)	0.78 ± 0.22	1.26 ± 0.77	0.79 ± 0.21
Combinatorial	9.99 ± 0.33	–	2.37 ± 0.07	–

Table 3.8 – Results of the fit to the corrected B mass distribution of the $B^0 \rightarrow D^-(\rightarrow K^+K^-\pi^-)\mu^+\nu X$ and $B^0 \rightarrow D^-(\rightarrow K^+\pi^-\pi^-)\mu^+\nu X$ samples. Uncertainties of the branching ratios of the decays are included in the expected fractions. The $B^0 \rightarrow D^-\tau^+\nu X$ component is shown in parentheses because it is neglected in the subsequent analysis.

Figure 3.10 shows the corrected B mass distribution, with results of the fit overlaid, for the $K^+K^-\pi^-$ and $K^+\pi^-\pi^-$ samples. Fit results are reported in Tab. 3.8, compared with the expectations of Tab. 3.5 and the background estimation discussed in Sect. 3.3.2, after accounting for the fraction of the combinatorial background. The χ^2/ndf of the fits are $103.9/89$ (probability 13.4%) in the $K^+K^-\pi^-$ sample and $109.6/88$ (probability 5.9%) in the $K^+\pi^-\pi^-$ sample. Correlation matrices are in App. A.1. The fraction of each component is not expected to be the same in the $K^+K^-\pi^-$ and $K^+\pi^-\pi^-$ samples, because the selection differs for the two data sets. The $B^0 \rightarrow D^-\tau^+\nu X$ component in the $K^+K^-\pi^-$ case is neglected in the subsequent analysis since it is found to be negative and compatible with zero; we still keep this component in the case of the $K^+\pi^-\pi^-$ sample.

Results in both samples are compatible with the expectations from known branching fractions and measured efficiencies, building confidence on the fit of the sample composition.

3.4.2   Fit to the B_s^0 data sample

In the fit of the B_s^0 samples we consider the four categories of Tab. 3.5, the physics backgrounds described in Sec. 3.3.2, and the combinatorial background.
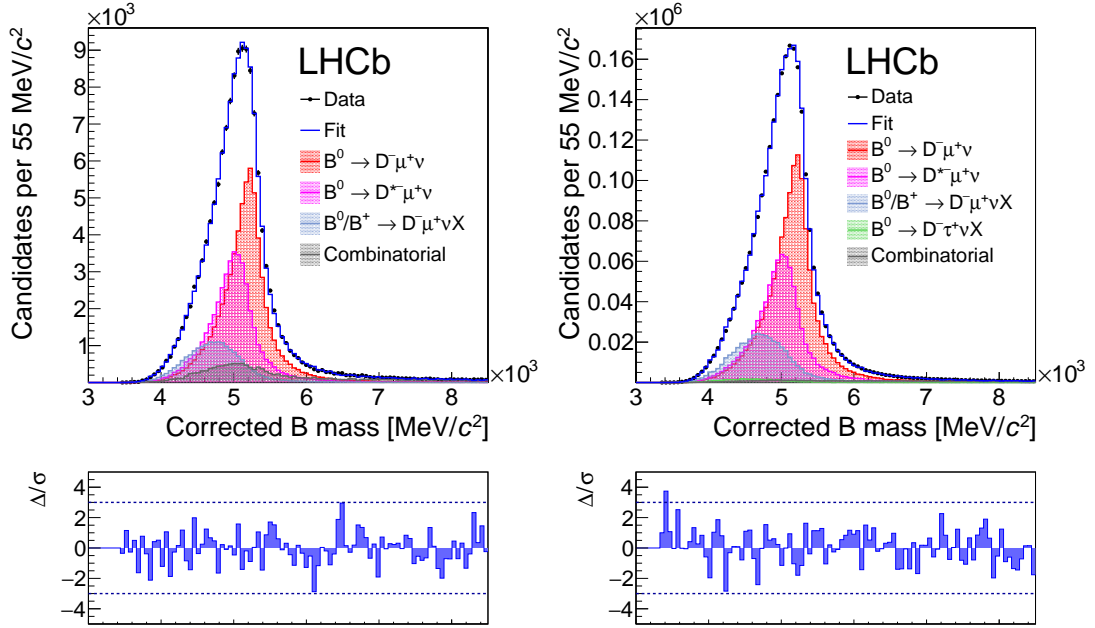
Figure 3.10 – Corrected B mass distributions of the (left) $B^0 \to D^-(\to K^+K^-\pi^-)\mu^+\nu X$ and (right) $B^0 \to D^-(\to K^+\pi^-\pi^-)\mu^+\nu X$ samples with results of the fit overlaid.

Component	Fit fraction [%]
$B_s^0 \to D_s^-\mu^+\nu$	29.20 ± 0.52
$B_s^0 \to D_s^{*-}\mu^+\nu$	57.77 ± 0.91
$B_s^0 \to D_{(s)}^{(**)}(D_s)X$ (backg. 1)	3.21 ± 0.74
$B_s^0 \to D_s(K\mu\nu)(\tau\nu)$ (backg. 2)	4.00 ± 0.28
Combinatorial	5.82 ± 0.13

Table 3.9 – Results of the fit to the corrected B mass distribution of the B_s^0 sample.

The top row of Fig. 3.11 shows the distributions of the different physics backgrounds. The decays $B^0 \to D^{(*)-}D_s^{(*)+}$, $B^+ \to D^{(*)0}D_s^{(*)+}$, $\Lambda_b^0 \to \Lambda_c^+D_s^{(*)+}(\pi^0)$, $B_s^0 \to D_s^{(*)-}D_s^{(*)+}$ and $B_s^0 \to D_{(s)}^{**}\mu X$, feature very similar shapes; they are therefore lumped together in a single template (referred to as B_s^0 background 1 in the following), each weighted with the expected fraction with respect to the signal (see Tab. 3.6). In the sum, we only consider components expected to contribute by more than 0.5% of the signal yield, and thus neglect $\Lambda_b^0 \to \Lambda_c^+D_s^{(*)+}(\pi^0)$ and $B_s^0 \to D_s^{(*)-}D_s^{(*)+}$ decays; the impact of this simplification is considered in Sect. 3.8.3. Similarly, the decays $B^- \to D_s^{(*)+}K^-\mu^-X$, $B^0 \to D_s^{(*)-}K_S^0\mu^+X$ and $B_s^0 \to D_s^-\tau^+(\to \mu^+\nu\nu)\nu X$ are grouped in a single template (B_s^0 background 2 in the following). Note that the two last categories of Table 3.5 have to be considered as background here, as they cannot be separated from the other physics backgrounds. The bottom of Fig. 3.11 shows mass shapes for all the components used in the fit: the two signal components, B_s^0 backgrounds 1 and 2, and SS data for combinatorics. The shapes of the mass distribution are sufficiently distinct to allow for a statistical separation.

Fit results are reported in Tab. 3.9 and the mass distribution of the data along with the fitted
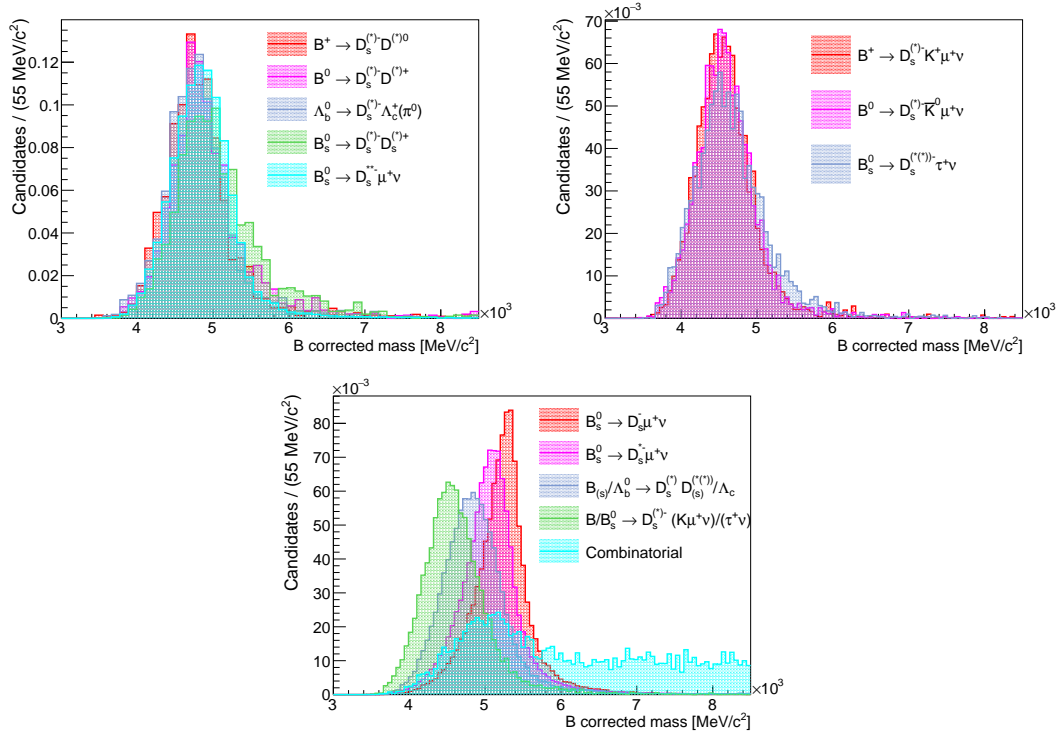
Figure 3.11 – Corrected B mass distribution for (top left) $B^0 \to D^{(*)-}D_s^{(*)+}$, $B^+ \to D^{(*)0}D_s^{(*)+}$, $\Lambda_b^0 \to \Lambda_c^+ D_s^{(*)+}(\pi^0)$, $B_s^0 \to D_s^{(*)-}D_s^{(*)+}$ and $B_s^0 \to D_{(s)}^{**}\mu X$ backgrounds; (top right) $B^- \to D_s^{(*)+}K^-\mu^- X$, $B^0 \to D_s^{(*)-}K_S^0\mu^+ X$ and $B_s^0 \to D_s^-\tau^+(\to \mu^+\nu\nu)\nu X$ backgrounds; and (bottom) all final components used to fit the B_s^0 sample.

distributions of each component are shown in Fig. 3.12. The χ^2/ndf of the fit is 84.3/89 (probability 62.1%). The correlation matrix of the fit is in App. A.1. Variations of this fit are discussed in Sect. 3.8.3 for the assessment of systematic uncertainties.

3.5 Determination of $\Delta(D)$

The difference between the decay widths of the D_s^- and D^- mesons, $\Delta(D)$, is measured through a fit to the ratio of B_s^0 and B^0 signal yields as a function of the decay time of the $D_{(s)}^-$ candidates, t_D. In each decay-time bin, signal yields are extracted with a fit to the corrected B mass. The ratio of the B_s^0 and B^0 signal yields as function of t_D is then fitted to measure $\Delta(D)$, with a function which includes the decay-time acceptance and resolution, derived from simulation.

3.5.1 Signal yields as functions of t_D

We split the full data and simulation samples into 20 subsamples (decay-time bins) according to the decay time of the $D_{(s)}^-$ candidates, such that the amount of B_s^0 signal events is nearly equal in all subsets. However, as the D_s^- lifetime is roughly two times smaller than the D^- lifetime, the splitting also needs to make sure the first bins are sufficiently populated by B^0 signal events. In each bin, we determine the yields of $B_{(s)}^0 \to D_{(s)}^-\mu^+\nu$ and $B_{(s)}^0 \to D_{(s)}^{*-}\mu^+\nu$ de-
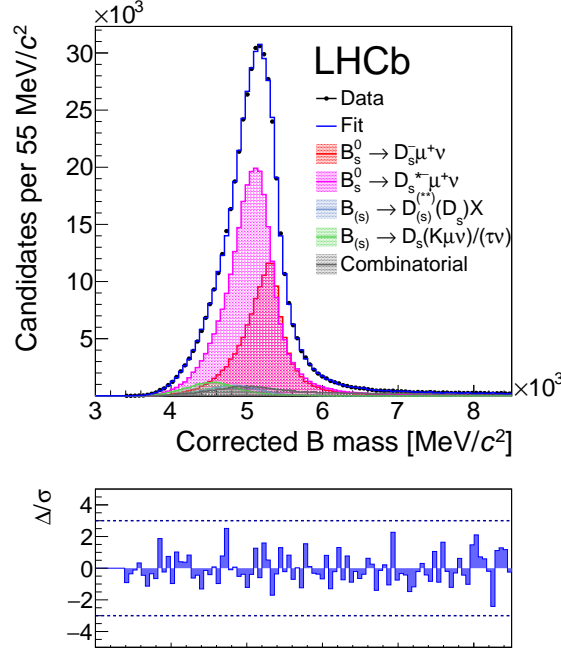
Figure 3.12 – Corrected B mass distribution of the $B_s^0 \to D_s^-(\to K^+K^-\pi^-)\mu^+\nu X$ sample with results of the fit overlaid.

cays using fits to the corrected B mass. These fits are similar to those described in Sec. 3.4, but with a simpler model. First, the $B_{(s)}^0 \to D_{(s)}^-\mu^+\nu$ and $B_{(s)}^0 \to D_{(s)}^{*-}\mu^+\nu$ contributions are merged into a single signal component with relative fractions extracted from the time-integrated fit; similarly, all other physics contributions are merged into a single template (the $B^0 \to D^-\tau^+\nu X$ component in the $K^+K^-\pi^-$ sample is not considered in this sum, as its yield is found to be consistent with zero, see Tab. 3.8). The combinatorial background is still described by a separate template from SS data. The χ^2 function of Eq. (3.8) is minimised to obtain the fraction of the signal in each decay time bin; the signal yields are determined from the product of these fractions and the total number of candidates in the decay time bin. Detailed fit results for the B_s^0 and B^0 samples are reported in Appendix A.2.

3.5.2 Relative acceptance correction

The similarity between signal and reference decays and the use of common selection criteria results in nearly identical D_s^- and D^- decay-time acceptances. Figure 3.13 (left) shows the ratio of acceptances as determined using simulation for the two main signal components, $B_{(s)}^0 \to D_{(s)}^-\mu^+\nu$ and $B_{(s)}^0 \to D_{(s)}^{*-}\mu^+\nu$ with proportions consistent with those measured in data. A fit with a linear function $a + bt_D$ gives $a = 1.0108 \pm 0.0042$ and $b = -0.0108 \pm 0.0043\,\text{ps}^{-1}$ with $\chi^2/\text{ndf} = 14.3/18$ (probability of 71%); a fit with a flat line gives $\chi^2/\text{ndf} = 20.5/19$ (probability of 37%). The $\Delta\chi^2$ between the two fits corresponds to a 2.4σ deviation of the ratio from a constant. Although not very significant, we prefer to account for the acceptance ratio in the lifetime fit for the $\Delta(D)$ measurement by using the histogram of Fig. 3.13 as a template.
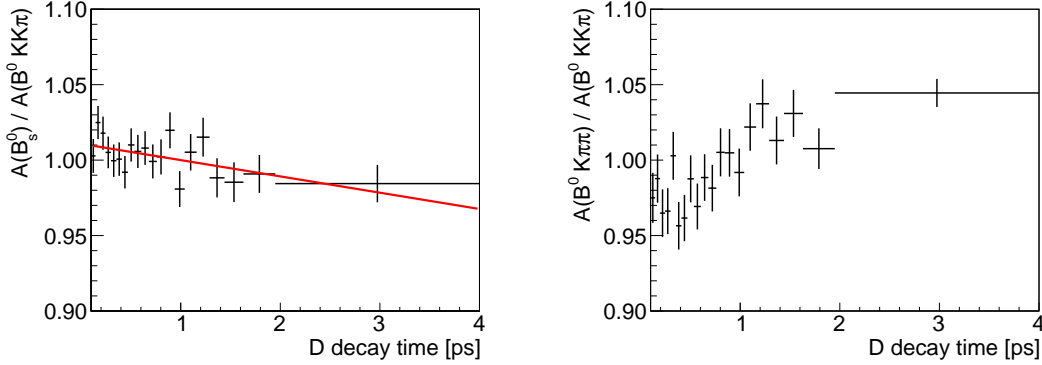
Figure 3.13 – Ratio of acceptances as a function of D decay time for (left) B_s^0 over B^0 and (right) B^0 ($K^+\pi^-\pi^-$) over B^0 ($K^+K^-\pi^-$) in simulation.

Figure 3.13 (right) shows the acceptance ratio between the two B^0 samples, $K^+\pi^-\pi^-$ over $K^+K^-\pi^-$. The ratio of the acceptances presents a larger variation of around 10%, due to the different kinematics and selection requirements of the $K^+K^-\pi^-$ and $K^+\pi^-\pi^-$ samples. This ratio is used in Sect. 3.5.4 in the validation of the $\Delta(D)$ measurement.

3.5.3 Lifetime fit

A binned least-squares fit is used to extract $\Delta(D)$, by minimising

$$\chi^2 = \sum_i^{\text{bins}} \frac{(n_i - R_i d_i)^2}{\sigma_{n_i}^2 + R_i^2 \sigma_{d_i}^2}, \tag{3.9}$$

where n_i (d_i) is the yield of the numerator (denominator) in decay-time bin i, σ_{n_i} (σ_{d_i}) its uncertainty, and R_i is the expected ratio defined as

$$R_i = N A_i \frac{\int_{T_i} \text{pdf}_n(t_D) \, dt_D}{\int_{T_i} \text{pdf}_d(t_D) \, dt_D}. \tag{3.10}$$

For the bin i, T_i is the corresponding t_D interval, A_i is the ratio between the decay-time acceptances of the numerator over the denominator in this bin, $\text{pdf}_{n(d)}$ is the pdf of the numerator (denominator), and N a normalisation factor. The integral over t is done numerically with 100 steps per decay-time bin. In the χ^2 definition, $\sigma_{n_i}^2 + R_i^2 \sigma_{d_i}^2$ is a good approximation of the uncertainty of the ratio of two Poisson-distributed variables. Each pdf is written as

$$\text{pdf}_j(t_D) = e^{-\Gamma_j t_D} \otimes \mathscr{G}_j^{\text{res}}(t_D) \qquad (j = n, d), \tag{3.11}$$

where $\otimes$ represents a decay-time convolution, Γ_j is the decay width and $\mathscr{G}_j^{\text{res}}(t_D)$ is the decay-time resolution, which is modelled from simulations using the template histograms shown in Fig. 3.14. This distribution of the difference between reconstructed and true decay time has an RMS of about 70 fs. The convolution of Eq. (3.11) is evaluated numerically with 100 steps. In the denominator, Γ_d is fixed to the known value of the D^- lifetime, $\tau(D^-) = 1.040 \pm 0.007$ ps [19]; while the width of the numerator, Γ_n, is written as $\Gamma_d + \Delta(D)$ with $\Delta(D)$ determined by the fit.
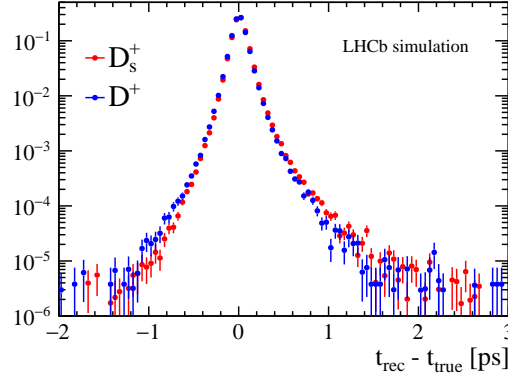
Figure 3.14 – Distributions of the difference between reconstructed and true D decay times for the (red) B_s^0 and (blue) B^0 ($K^+ K^- \pi^-$) samples. These distributions are used to describe the D-decay-time resolution in the fit.

The normalisation N is also a free parameter, while the decay-time resolution histograms have no free parameters.

3.5.4   Null test using B^0 decays

We perform a null test to validate the analysis method by measuring the ratio between signal yields determined in the two B^0 samples, $K^+ \pi^- \pi^-$ and $K^+ K^- \pi^-$. We use the $K^+ K^- \pi^-$ as the reference (denominator) in the ratio and expect to measure a null value of $\Delta(D)$ with a similar precision as the real $\Delta(D)$ analysis, since both measurements are limited by the size of the B^0 $K^+ K^- \pi^-$ sample.

Detailed results of the mass fits in bins of decay time are presented in App. A.2. Figure 3.15 shows the yield-ratio distribution after acceptance correction with the results of the decay-time fit overlaid. The fit has $\chi^2/\mathrm{ndf} = 19.5/18$ (probability 36%) and yields

$$\Delta(D)_{\mathrm{null-test}} = (-19 \pm 10) \times 10^{-3}\,\mathrm{ps}^{-1}. \tag{3.12}$$

Although the result deviates a little from the expectation, it is still consistent with zero. The success of the null test builds confidence on the analysis strategy, confirming the reliability of the mass model to subtract the backgrounds and of the simulation for describing the ratio of acceptances. Indeed, even with deviations of the order of 10% in the acceptances ratio, the result stays consistent.

3.5.5   Results

The fit of the ratio of the B_s^0 and B^0 ($K^+ K^- \pi^-$) signal yields in bins of $D_{(s)}$ decay time yields

$$\Delta(D) = 1.0131 \pm 0.0117\,\mathrm{ps}^{-1}. \tag{3.13}$$
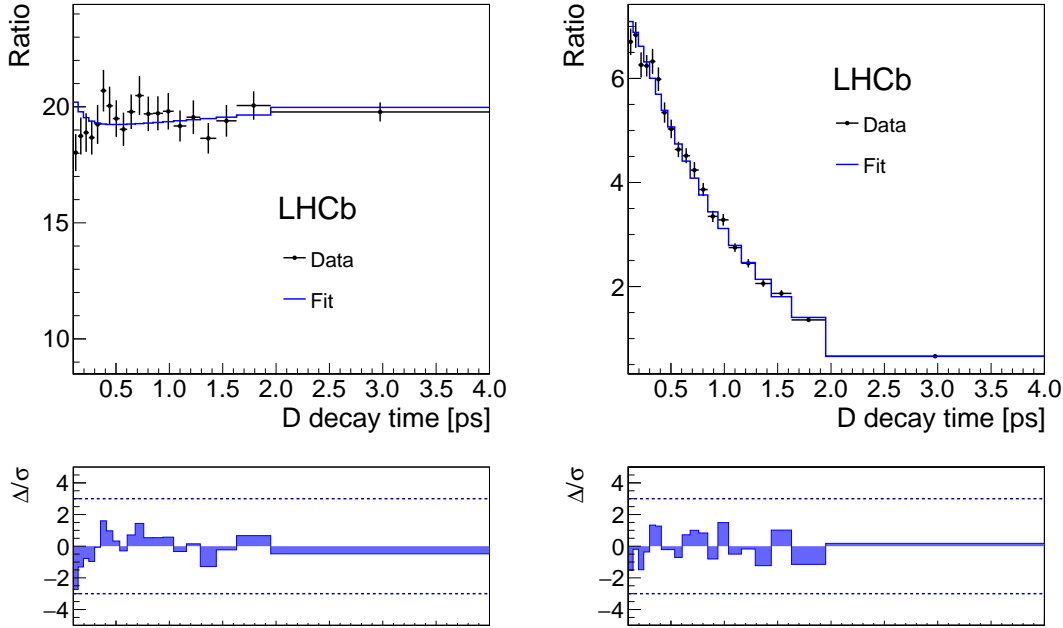
Figure 3.15 – Acceptance-corrected signal-yield ratio of (left) the two B^0 samples, $K^+\pi^-\pi^-$ over $K^+K^-\pi^-$, and (right) B_s^0 over B^0 ($K^+K^-\pi^-$) as a function of D decay time with fit projection overlaid.

Figure 3.15 shows the yield-ratio distribution after acceptance correction with results of the time-fit overlaid. The fit quality is good, with $\chi^2/\text{ndf} = 18.0/18$ (probability 45%). Systematic errors associated to this measurement are discussed in Section 3.8. Section 3.9 presents the final results and the determination of the D_s^- lifetime.

3.6 Determination of $\Delta(B)$

The difference $\Delta(B)$ between the decay widths of the B_s^0 and B^0 mesons is measured through a fit to the ratio of B_s^0 and B^0 signal yields as a function of the B decay time, in a way similar to the $\Delta(D)$ measurement. However, in order to get an unbiased estimate of the decay time, a simulation-based correction that accounts for the missing momentum of unreconstructed final-state particles has to be applied. Then, the samples are divided according to the resulting corrected decay time, and the signal yields in each corrected-decay-time bin are extracted with a mass fit similar to the one described in Sect. 3.5.1. The fit to the ratio of the B_s^0 and B^0 signal yields as a function of the corrected decay time determines $\Delta(B)$. The effects of decay-time acceptance and resolution are studied in simulation and included in the fit when necessary.
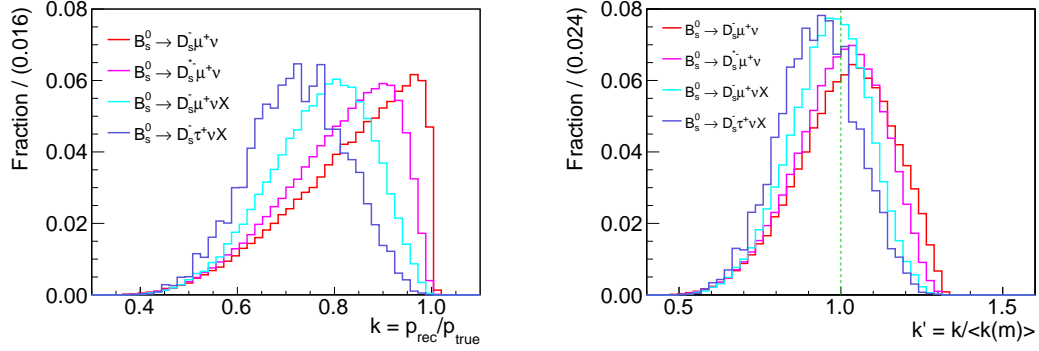
Figure 3.16 – Distributions of (left) $k(m)$ and (right) k' for the different internal components of the simulated inclusive sample of $B_s^0 \to D_s^-(\to K^+K^-\pi^-)\mu^+\nu X$ decays. The k'-factor is determined by using the function $\langle k \rangle (m)$ of the full sample.

3.6.1 Missing momentum correction

The missing momentum correction is determined from simulation and is represented by a scale factor, k, which is a function of the $D_{(s)}\mu$ invariant mass, m,

$$\langle k \rangle (m) = \left\langle \frac{p(D\mu)}{p^{\text{true}}(B)} \right\rangle (m), \tag{3.14}$$

where $p(D\mu)$ is the reconstructed momentum of the $D_{(s)}^-\mu^+$ system, $p^{\text{true}}(B)$ the true momentum of the $B_{(s)}^0$ meson, known in simulated samples, and where the average is done over all events in a given mass range. The decay-time smearing introduced by this correction is also determined from simulation through the distribution of the per-event k factor scaled by its average value as a function of the $D_{(s)}\mu$ mass [73, 74].

$$k'(m) = \frac{p(D\mu)/p^{\text{true}}(B)}{\langle p(D\mu)/p^{\text{true}}(B)\rangle(m)}. \tag{3.15}$$

The k and k' distributions both depend on the kinematic properties of the decay channel. As an example, Fig. 3.16 shows these two distributions for the four distinct categories of the inclusive B_s^0 signal decays from Table 3.5. The magnitude of missing momentum increases with the number of unreconstructed candidates' final-state particles and may also depend on the kinematics of a decay. As the missing momentum increases, the distribution of k-factors is shifted and peaks at lower values; the more the unreconstructed final-state particles, the poorer the resolution in the determination of the momentum correction. We therefore restrict our signal to the two main components $B_{(s)}^0 \to D_{(s)}^-\mu^+\nu$ and $B_{(s)}^0 \to D_{(s)}^{*-}\mu^+\nu$ only, which guarantee smaller corrections and better determined k-factors. In addition, it allows to merge the remaining components of the inclusive signal decays, which contribute to less than 5% (9%) of the total signal in the B_s^0 (B^0) case, with the other physics backgrounds, as corrected mass templates of these remaining components are complicated to disentangle from templates of physical backgrounds, as discussed in Sec. 3.4.2. The relative contribution

53
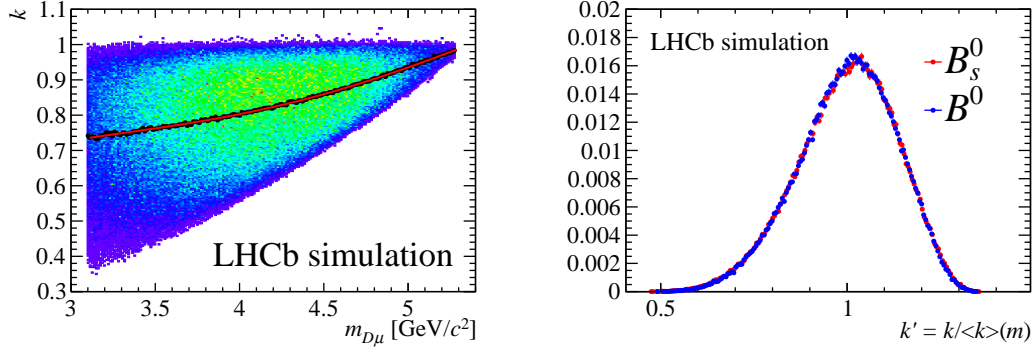
Figure 3.17 – Distribution of (left) k-factor for different $D_s\mu$ invariant mass m and corresponding function $\langle k \rangle (m)$ for the B_s^0 sample and (right) k' factor for B_s^0 and $B^0 \to D^-(\to K^+K^-\pi^-)\mu^+\nu X$ samples.
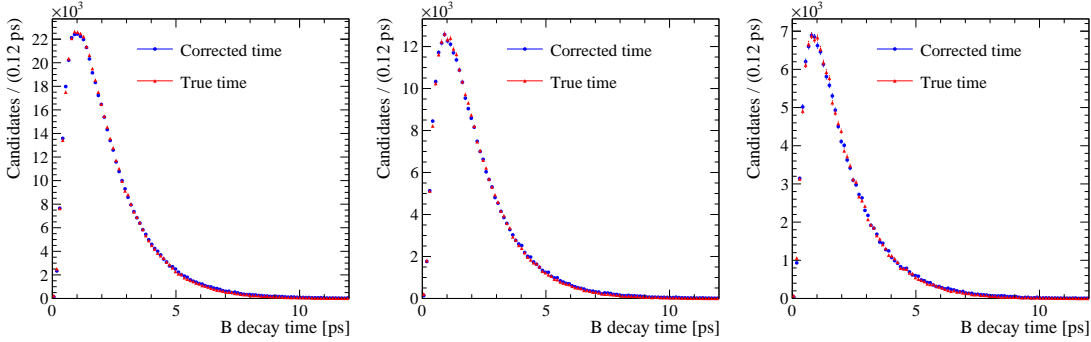
Figure 3.18 – Comparison between corrected and true decay time in simulation for (left) B_s^0, (middle) $B^0 \to D^-(\to K^+K^-\pi^-)\mu^+\nu X$ and (right) $B^0 \to D^-(\to K^+\pi^-\pi^-)\mu^+\nu X$ samples.

of the two main components in simulation is matched to that measured in data to improve the scale-factor determination. Figure 3.17 shows the k distribution for the B_s^0 sample and the k' distribution for the B_s^0 and $B^0 \to D^-(\to K^+K^-\pi^-)\mu^+\nu X$ samples. The corresponding k distributions for the two B^0 sample and k' distribution for the $B^0 \to D^-(\to K^+\pi^-\pi^-)\mu^+\nu X$ sample are extremely similar. The rare candidates outside the $D_{(s)}\mu$ invariant mass region used in the fit are assigned unit k factor. The observed B decay time, t, is corrected as follows:

$$t_{\mathrm{corr}} = t\, k(m).\tag{3.16}$$

Figure 3.18 shows the t_{corr} distribution in simulations compared to the true B decay time. The correction transforms t into an unbiased estimate of the B decay time.

3.6.2 B_s^0 sample reweighting and decay-time acceptances

The topological triggers are more efficient for decays with closely spaced B and D vertices, resulting in events that predominantly contain D candidates with small flight distance, and thus decay time. As the D^- lifetime is around twice the D_s^- lifetime, the efficiency strongly differs between the two decays, as shown in Fig. 3.19 (left), where the ratio of decay-time
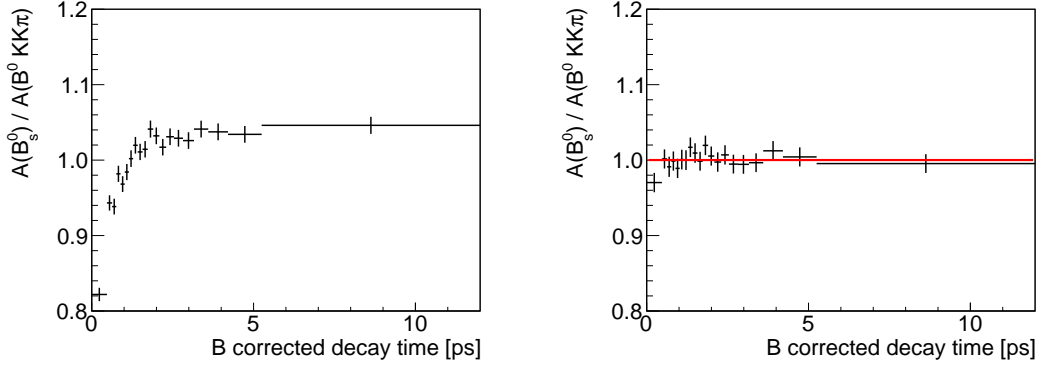
Figure 3.19 – Ratio of decay-time acceptances of $B_s^0 \to D_s^-(\to K^+K^-\pi^-)\mu^+\nu X$ over $B^0 \to D^-(\to K^+K^-\pi^-)\mu^+\nu X$ as determined in simulation (left) without and (right) with the reweighting based on the $D_{(s)}$ lifetime described in Sec. 3.6.2.

acceptances between B_s^0 and B^0 decays is shown. The ratio of acceptances is determined by using simulation for the two main signal components, $B^0_{(s)} \to D_{(s)}^-\mu^+\nu$ and $B^0_{(s)} \to D_{(s)}^{*-}\mu^+\nu$ mixed with proportions equal to those measured in data.

To reduce the impact of this difference, a candidate-by-candidate weight w_D is applied on the B_s^0 sample, in order to reduce the differences between the D^- and D_s^- decay-time distributions,

$$w_D = e^{\Delta(D)t_D}, \tag{3.17}$$

where $\Delta(D) = 1.0131\,\mathrm{ps}^{-1}$ is the value measured in Sect. 3.5.5. This weight is applied just after the selection, and therefore affects all subsequent analysis steps in the measurement of $\Delta(B)$, including the fit of sample composition. The results of the B_s^0 sample composition fit after reweighting are reported in App. A.3.

Figure 3.20 shows the decay-time distributions of D_s^- simulated candidates before and after the reweighting. The D_s^- distribution becomes consistent with the D^- distribution for $t_D > 0.1\,\mathrm{ps}$, corresponding to the value of the selection cut. Figure 3.19 (right) shows that the D-lifetime reweighting of Eq. (3.17) reduces effectively most differences between decay-time acceptances. After reweighting, the ratio of acceptances is compatible with a uniform distribution with $\chi^2/\mathrm{ndf} = 13.2/19$ (probability of 83%). Having performed this reweighting, we can perform a measurement of decay-widths difference, by neglecting the ratio of decay-time acceptances in the lifetime fit and by treating any residual difference in the systematic uncertainties.

We also study the acceptance ratio between the two B^0 samples, $K^+\pi^-\pi^-$ over $K^+K^-\pi^-$ (Fig. 3.21). These samples are used in Sect. 3.6.5 to validate the $\Delta(B)$ measurement. Unlike for the ratio between B_s^0 and $B^0 \to D^-(\to K^+K^-\pi^-)\mu^+\nu X$ modes, here the ratio differs significantly from one, with relative deviations of up to 20%. Such large acceptance differences are due to significantly different selections, especially at the stripping stage, on kinematic and geometric discriminants like, for example, the momenta of final-state particles and the D-vertex separation from the primary vertex. As the criteria on the momenta are tighter for
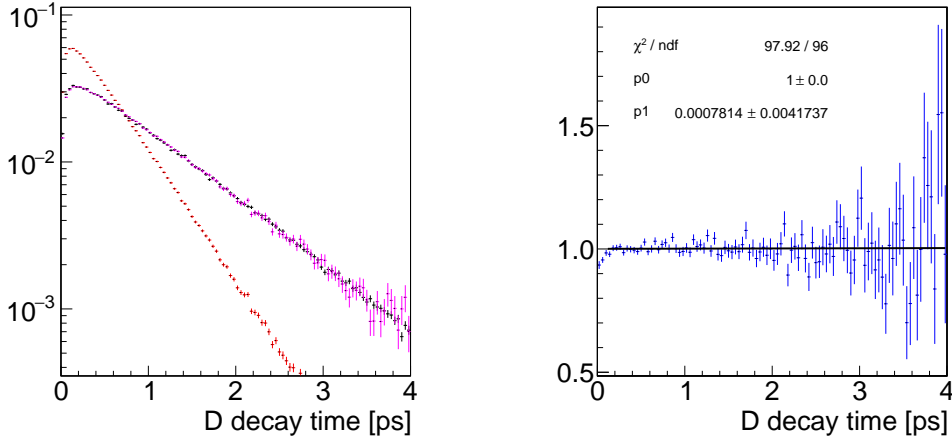
Figure 3.20 – (Left) Decay-time distribution of D candidates in simulations. The distribution of D_s^- candidates is shown (red) before and (magenta) after the reweighting of Eq. (3.17); D^- candidates are shown in black. (Right) Ratio between the D_s^- and D^- decay-time distributions in simulation after the reweighting of the D_s^- candidates; the ratio is consistent with a uniform distribution starting from 0.1 ps (data below 0.1 ps are removed by the offline selection, Tab. 3.2).
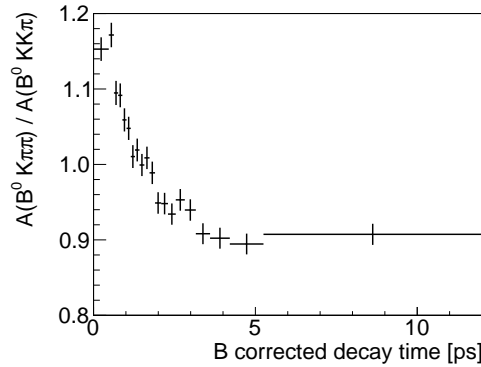
Figure 3.21 – Ratio of the decay-time acceptances of $B^0 \to D^-(\to K^+\pi^-\pi^-)\mu^+\nu X$ over $B^0 \to D^-(\to K^+K^-\pi^-)\mu^+\nu X$ as a function of corrected B decay time.

the $K^+\pi^-\pi^-$ sample, for a given decay time, B candidates will fly further away from the PV and will be easier to reconstruct, hence the larger efficiency at low decay time compared to the $K^+K^-\pi^-$ sample.

3.6.3 Signal yields as functions of decay time

We split the sample into 20 subsamples (decay-time bins) according to the candidate's corrected B decay time, such that the amount of B^0 signal events is approximately the same in each subset. In each bin, we determine the yields of $B_{(s)}^0 \to D_{(s)}^- \mu^+ \nu$ and $B_{(s)}^0 \to D_{(s)}^{*-} \mu^+ \nu$ decays using fits to the corrected B mass, as described in Sect. 3.5.1. Detailed fit results for the B_s^0 and B^0 samples are in App. A.2.
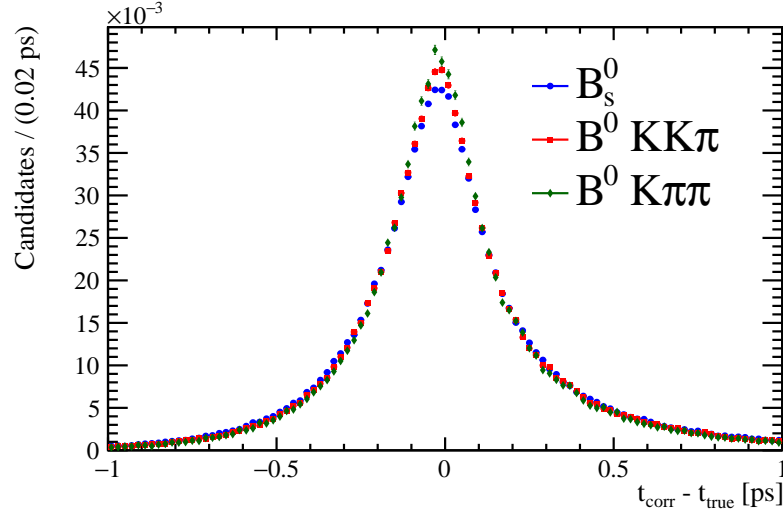
Figure 3.22 – Distributions of the difference between the true decay time and the decay time computed using the reconstructed B flight distance and the true B momentum, for (blue) $B_s^0 \rightarrow D_s^-(\rightarrow K^+K^-\pi^-)\mu^+\nu X$, (red) $B^0 \rightarrow D^-(\rightarrow K^+K^-\pi^-)\mu^+\nu X$ and (green) $B^0 \rightarrow D^-(\rightarrow K^+\pi^-\pi^-)\mu^+\nu X$ decays. A double-Gaussian is fit to extract the shape of the distribution and determine the resolution due to the flight distance.

3.6.4 Lifetime fit

The binned least-square fit of Sect. 3.5.3 is used to measure $\Delta(B)$. The pdf's of Eq. (3.11) is modified to include the k' resolution due to the incomplete correction for the missing final-state particles:

$$\mathrm{pdf}_j(t) = \int k' e^{-\Gamma_j k' t} F_j(k') dk' \qquad (j = n, d). \tag{3.18}$$

Here, Γ_j is the decay width and $F_j(k')$ is the one-dimensional distribution of the k' factor (Fig. 3.17, right). The integral over k' is evaluated numerically with 200 steps. In the denominator, Γ_d is fixed using the known value of the B^0 lifetime, $\tau(B^0) = 1.520 \pm 0.004$ ps [19]; while the width of the numerator, Γ_n, is written as $\Gamma_d + \Delta(B)$, with $\Delta(B)$ free in the fit.

Effects on the corrected decay time and on the determination of $\Delta(B)$ due to the decay-length resolution have been estimated in simulation (see Fig. 3.22) to be much smaller than those caused by the missing momentum and are therefore neglected in the fit. The impact of this simplification is assessed in the evaluation of the systematic uncertainties.

3.6.5 Null test using B^0 decays

We also perform the full analysis in data using the two B^0 samples, $K^+\pi^-\pi^-$ and $K^+K^-\pi^-$. We use the $K^+K^-\pi^-$ sample as the reference mode (denominator) to measure $\Delta(B)$, expected to be zero, with a similar precision as for the B_s^0 measurement, since both are limited by the size of the B^0 $K^+K^-\pi^-$ sample. Here, the numerator and denominator acceptances (Fig. 3.21) are very different and we do not attempt at equalising them by reweighting. We instead include

the bin-by-bin acceptance ratio in the fit as described in Eq. (3.10).

Appendix A.2 collects the detailed results of the mass fits in bins of decay time. Figure 3.23 shows the yield-ratio distribution after acceptance correction with projections of the fit overlaid. The fit has $\chi^2/\mathrm{ndf} = 22.4/18$ (probability 21.5%) and we get

$$\Delta(B)_{\mathrm{null-test}} = (-4.1 \pm 5.4) \times 10^{-3}\,\mathrm{ps}^{-1}, \tag{3.19}$$

which is consistent with zero as expected. The success of the null test supports the analysis strategy, which proves to be robust even in the limiting case in which the variations in the decay-time acceptances are large (Fig. 3.21). It confirms mainly the reliability of the simulation for the description of mass templates, decay-time corrections and treatment of acceptances. The observed structures in the low decay-time region are most likely due to an imperfect modelling of the large variation of the acceptance ratio. However, this is not a concern for the measurement of $\Delta(B)$ as the ratio of B_s^0 and $B^0(KK\pi)$ acceptances, after the reweighting of the B_s^0 sample is flat as a function of corrected B decay time (Fig. 3.19).

3.6.6 Results

The fit to the ratio of the B_s^0 and B^0 ($K^+K^-\pi^-$) signal yields in bins of decay time yields

$$\Delta(B) = -0.0115 \pm 0.0053\,\mathrm{ps}^{-1}. \tag{3.20}$$

Figure 3.23 shows the yield-ratio with the results of the decay-time fit overlaid; the fit quality is $\chi^2/\mathrm{ndf} = 10.5/18$ (probability 91%). Systematics uncertainties are now discussed and followed by the final results and determination of the flavour-specific lifetime in Section 3.9.
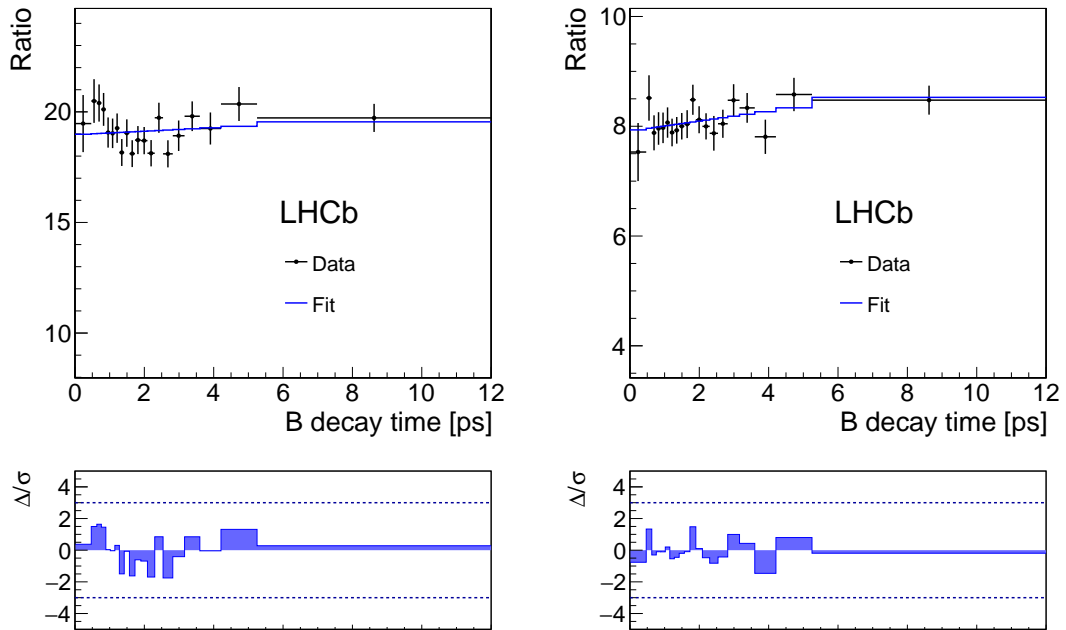
Figure 3.23 – (Left) Acceptance-corrected yield ratio of $B^0 \to D^-(\to K^+\pi^-\pi^-)\mu^+\nu X$ over $B^0 \to D^-(\to K^+K^-\pi^-)\mu^+\nu X$ and (right) yield ratio of $B_s^0 \to D_s^-(\to K^+K^-\pi^-)\mu^+\nu X$ over $B^0 \to D^-(\to K^+K^-\pi^-)\mu^+\nu X$ decays as a function of corrected decay time with fit projections overlaid.

3.7   Analysis validation using pseudo-experiments

The entire analysis flow is validated using pseudo-experiments generated by resampling with repetitions (bootstrapping) the samples of fully-simulated signal and background decays that pass our selection requirements (the combinatorial background is obtained by bootstrapping the SS data sample).

In each pseudo-experiment, we generate pseudo-data with exactly the same statistics as the parent sample and with proportions of signal and background components as close as possible to that observed in the real data (Tabs. 3.8 and 3.9). Small differences are introduced in the fractions of background events to avoid too many repetitions of the same events. These proportions are allowed to fluctuate as a multinomial distribution in each pseudo-experiment. The generated pseudo-data contain all the information of the original data set and is therefore processed through the same entire analysis flow as the data, from the fit of sample composition of Sec. 3.4 to the time-dependent fits of Secs. 3.5 and 3.6, including also the recalculation of the missing-momentum correction, the decay-time acceptances, the resolutions, and the D-decay-time weights, according to the pseudo-experiment-specific fitted compositions.

In the fit of the sample composition, the distribution of the residual of each component fraction shows that the fit is free of biases, while the pull distributions have a width that is smaller than unity (about 80% for the B^0 fractions and 75% for the B_s^0 fractions). This reflects the contribution of the uncertainty introduced by the finite size of the simulated sample to the final statistical uncertainty. This effect is accounted for by the statistical uncertainties on each bin of the corrected mass templates, as written in the χ^2 expression of Eq. (3.8). It has been checked that the width of the pull distributions goes back to unity if, in Eq. (3.8), the uncertainties on the mass templates are not included. Therefore, the fit of the sample composition is found to be unbiased and to correctly estimate the uncertainty on the fractions.

Figure 3.24 shows the residual and pull distributions for $\Delta(D)$ and $\Delta(B)$. Here, the reference "true" values have been calculated using the numbers for the $D_{(s)}$ and $B_{(s)}^0$ lifetimes used in the generation of the parent sample, from which the pseudo-experiments are bootstrapped.
Also in this case the pull have a width that is smaller than unity, for the same reason. The direction of the effect is compatible with what is seen in the data, where, by repeating the analysis without including the statistical fluctuations of the mass templates, the uncertainty on $\Delta(D)$ determined by the fit decreases from 0.0117 ps^{-1} to 0.0104 ps^{-1}, and the uncertainty on $\Delta(B)$ from 0.0053 ps^{-1} to 0.0050 ps^{-1}.
No statistically significant biases are observed for $\Delta(D)$, where the distribution of the residuals has a mean value of $(-3.9 \pm 3.5) \times 10^{-4}$ ps^{-1}, while a small bias of $(9.3 \pm 1.5) \times 10^{-4}$ ps^{-1} is observed for $\Delta(B)$. The bias on $\Delta(B)$ is very small with respect to the precision of the measurement and therefore will only have a limited impact on the final measurement. A systematic uncertainty is assigned for both measurements in Section 3.8.1.

Finally, Fig. 3.25 shows, through the two-dimensional distribution of the $\Delta(D)$ and $\Delta(B)$ pulls, that the two measurements are mostly uncorrelated (the correlation coefficient is evaluated to be about 2%).
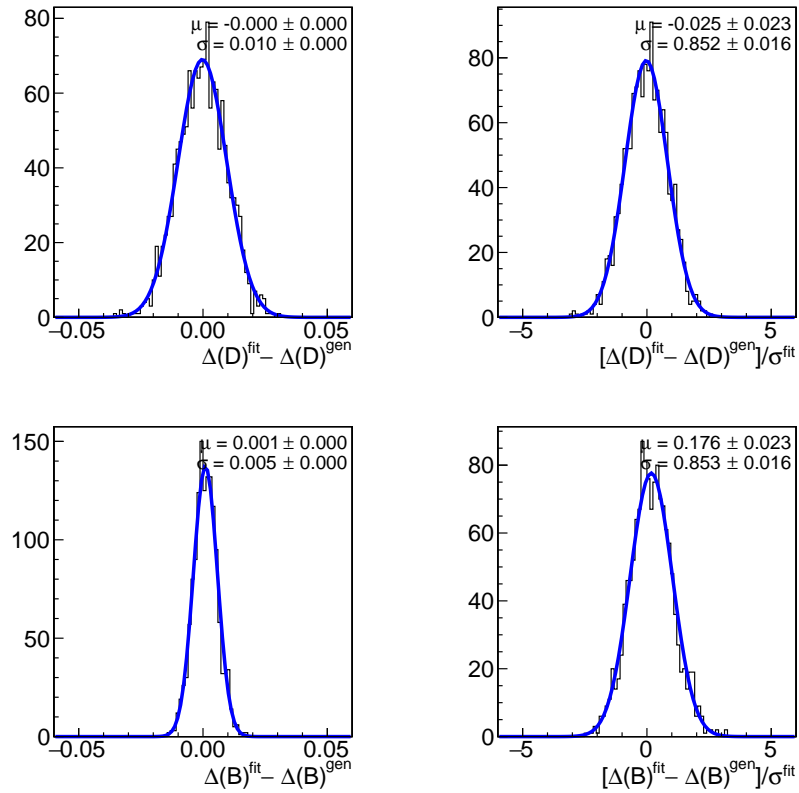
Figure 3.24 – (Left) Residual and (right) pull distributions for (top) $\Delta(D)$ and (bottom) $\Delta(B)$ fit values.
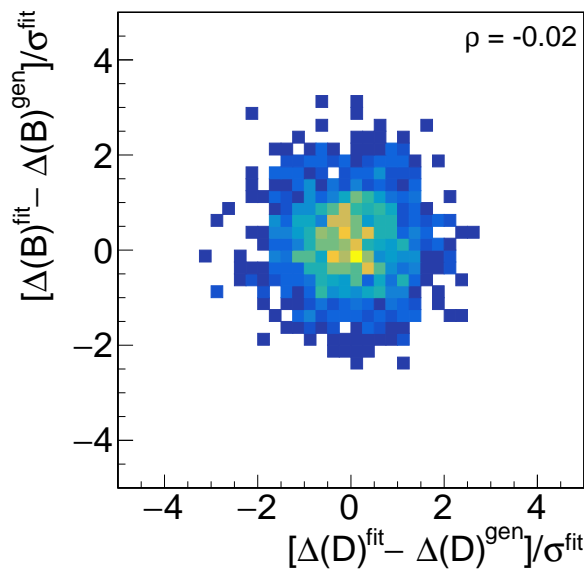
Figure 3.25 – Distribution of the $\Delta(B)$ pull versus the $\Delta(D)$ pull.

3.8   Systematic uncertainties and checks

Systematic uncertainties on the $\Delta(D, B)$ measurement are usually considered as the absolute value of the difference between the $\Delta(D, B)$ value obtained in the nominal analysis and the values obtained after modulating the parameters of the sources of systematic errors. We assess systematic uncertainties accounting for the following classes of effects: (i) fit biases; (ii) assumed form-factor model of the $B_s^0 \rightarrow D_s^{*-} \mu^+ \nu$ decay; (iii) assumptions on the components contributing to the sample and their mass shapes; (iv) mismodelling of transverse-momentum differences between B^0 and B_s^0 mesons production at pp collisions; (v) uncertainties associated with the decay-time acceptance; (vi) uncertainties associated with the decay-time resolution; (vii) contamination from B_s^0 candidates produced in B_c^+ decays. The sources (ii)–(iv) impact the determination of the sample composition and require to go through all subsequent steps of the analysis. In the case of $\Delta(B)$, it also means recomputing the k-factor and the decay-time correction, dependent on the two signal components fractions. The systematic uncertainties considered are listed in Tab. 3.10 and detailed in the following. The total systematic uncertainty is their sum in quadrature.

	$\sigma[\Delta(D)]$ [ps^{-1}]	$\sigma[\Delta(B)]$ [ps^{-1}]
Fit bias	0.0004	0.0009
Decay model of $B_s^0 \rightarrow D_s^{*-} \mu^+ \nu$	0.0005	0.0025
Sample composition	0.0007	0.0005
$f_s/f_d(p_T)$	0.0018	0.0028
Decay-time acceptance	0.0049	0.0004
Decay-time resolution	0.0039	0.0004
Feed-down from B_c^+ decays	–	0.0010
Total systematic	0.0065	0.0041
Statistical	0.0117	0.0053

Table 3.10 – Summary of the systematic and statistical uncertainties.

3.8.1   Fit bias

The measurement technique is validated with pseudo-experiments is Sec. 3.7. No statistically significant biases are found for the $\Delta(D)$ measurement, we therefore assign $0.0004\,\text{ps}^{-1}$ as systematic, corresponding to the uncertainty on the mean value of the residual distribution. The $\Delta(B)$ measurement shows a small bias of $0.0009\,\text{ps}^{-1}$, which is accounted for as a systematic uncertainty.

3.8.2   Model of $B_s^0 \rightarrow D_s^{*-} \mu^+ \nu$ decays in simulation

The decay form factors of the $B_s^0 \rightarrow D_s^{*-} \mu^+ \nu$ component are not known and are assumed to be close to those of the corresponding B^0 decay. To evaluate a corresponding systematic uncertainty, we identify the two most extreme variations (Fig. 3.26) out of nine alternative form-factor models, each obtained by changing at least one of HQET2 parameters of the
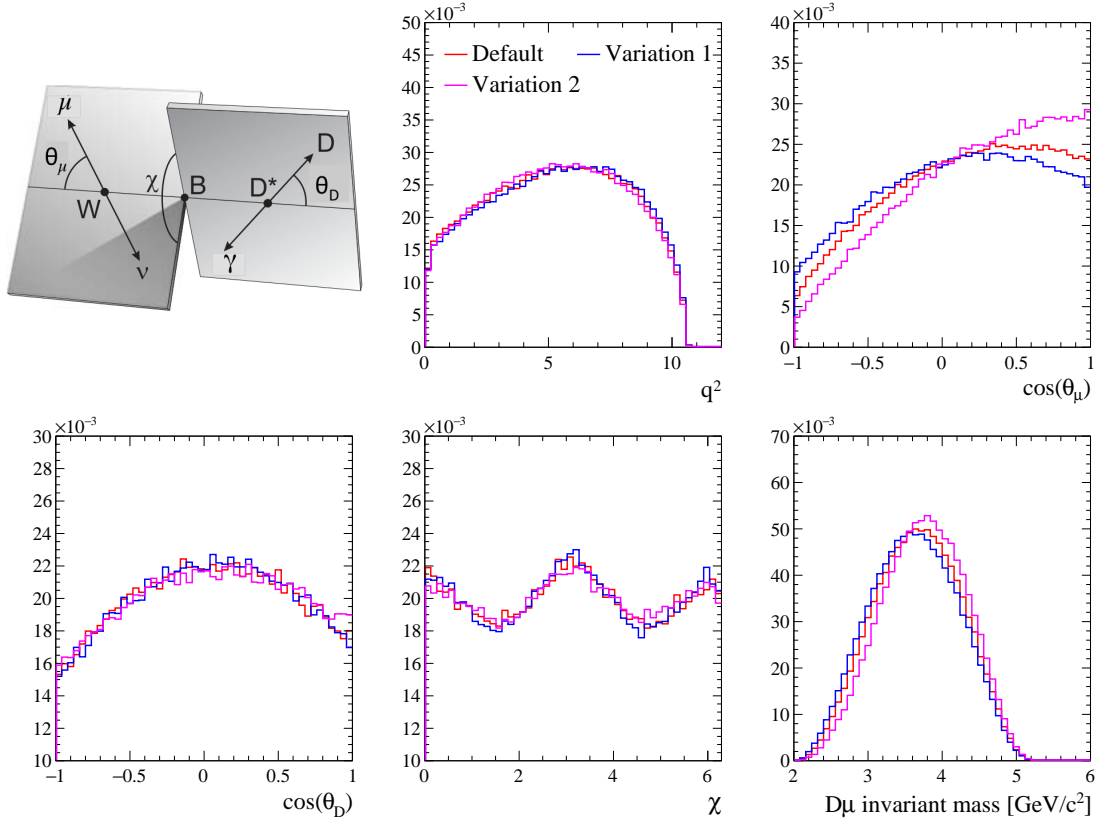
Figure 3.26 – (Top-left) Definition of the helicity angles in $B_s^0 \to D_s^{*-} \mu^+ \nu$ decays. Generator-level distributions of (top-middle) q^2, (top-right) $\cos\theta_\mu$, (bottom-left) $\cos\theta_D$, and (bottom-middle) χ. (Bottom-right) Reconstructed distribution of the $D_s\mu$ invariant mass. The (red) default model is compared with two (blue, magenta) alternative models obtained through extreme variations of the form-factor parameters. The first variation provides the largest difference in $\Delta(D, B)$ with respect to the nominal result.

nominal model by at least 50%. These two models are then used to fit pseudo-experiments generated with the default model (Sec. 3.7). The largest average variations in the measured value of $\Delta(D, B)$ amount to 0.0005 and 0.0025 ps^{-1}, respectively. These are used as systematic uncertainties due to the assumed form-factor model.

We notice in Fig. 3.26 that the helicity angles of the muon and the D_s^- meson, and the $D_s\mu$ mass show a large dependence on the form-factors model, unlike the corrected mass, which distribution only varies slightly as can be seen in Figure 3.27 (left). Thus, any mismodelling due to a poor simulation of the $B_s^0 \to D_s^{*-} \mu^+ \nu$ decay would be more evident in the distribution of the $D_s\mu$ invariant mass and the helicity angles. As an additional data-driven test of the used $B_s^0 \to D_s^{*-} \mu^+ \nu$ decay model, we show in Fig. 3.28 the projection of the fit of sample composition on the $D_s\mu$ mass for the nominal configuration and for the variation with different form factors. The agreement between the fit and the data is satisfactory for the nominal result, with $\chi^2/\text{ndf} = 107.2/82$ (probability 3%), while it is not for the alternative model, $\chi^2/\text{ndf} = 185.6/82$ (probability 10^{-8}). This supports the form-factors model used for the nominal results and suggests that the associated systematic uncertainty has been assessed using a somewhat extreme scenario. The relatively small difference in $\Delta(D, B)$ in this extreme case also proves
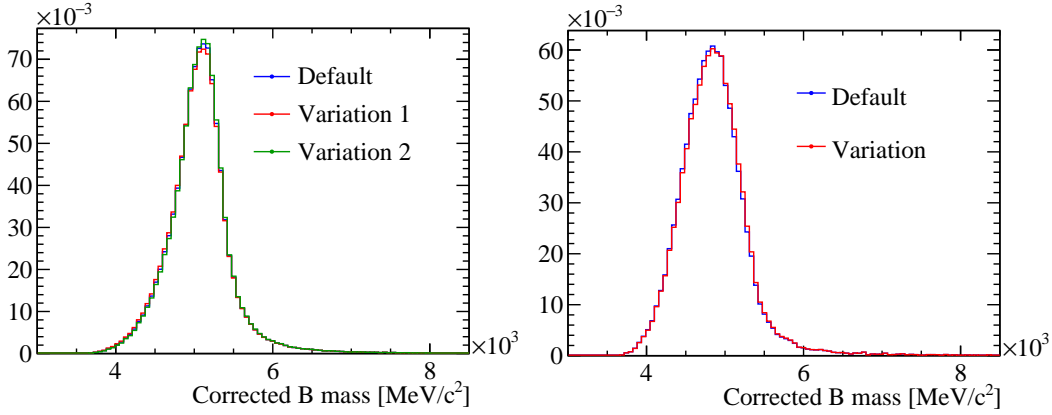
Figure 3.27 – Corrected B mass distribution of the (left) $B_s^0 \to D_s^{*-}\mu^+\nu$ for the default model and two form factors variations and (right) $B_s^0 \to D_s^{**-}\mu^+\nu$ decays for the default and alternate compositions.
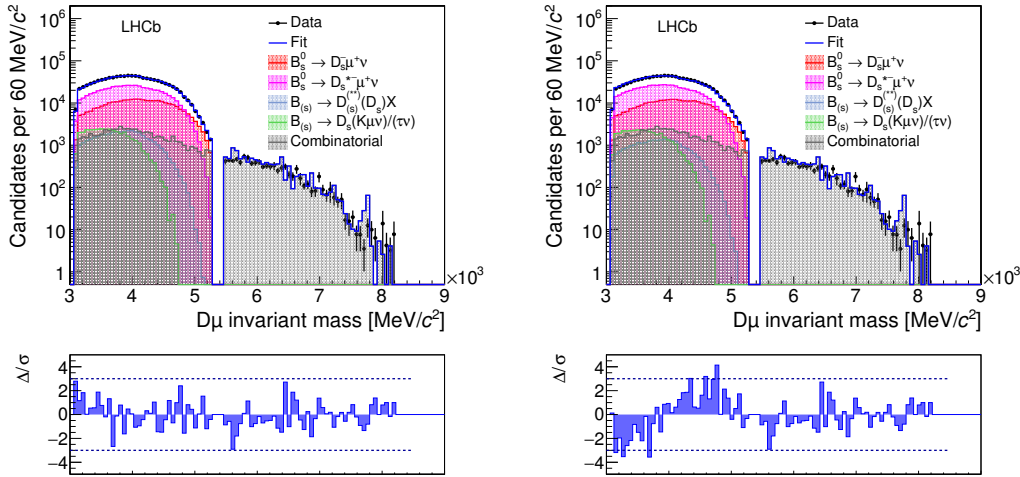
Figure 3.28 – Projection of the fit of sample composition on the $D_s\mu$ invariant mass using results and templates from (left) the nominal analysis and (right) the systematic variation of the $B_s^0 \to D_s^{*-}\mu^+\nu$ form-factors model.

than even though the $B_s^0 \to D_s^{*-}\mu^+\nu$ model might not be perfect, it is largely sufficient for the fit of the corrected mass.

3.8.3 Sample composition

The following variations to the nominal fit configuration of the B_s^0 sample are considered for assigning systematic uncertainties due to the limited knowledge of the sample composition:

1. we add a template for the $B \to DDK$ component;

2. we add a template for the $\Lambda_b^0 \to D_s^+ \Lambda^0 \mu^- \nu$ component;

3. we modify the internal composition of the $B_s^0 \to D_s^{**-}\mu^+\nu$ component to choose other proportions of each decay mode (Fig. 3.27, right);

4. we neglect the $B_s^0 \to D_s^- \tau^+ \nu X$ component;

5. we add the Λ_b^0 and B_s^0 decays of Tab. 3.6 in the physics background templates.

	Nominal	Adding $B \to DDK$	Adding $\Lambda_b^0 \to D_s^+ \Lambda^0 \mu^- \nu$
$B_s^0 \to D_s^- \mu^+ \nu$ [%]	29.26 ± 0.76	29.07 ± 0.79	28.98 ± 0.78
$B_s^0 \to D_s^{*-} \mu^+ \nu$ [%]	56.32 ± 1.34	57.03 ± 1.50	56.35 ± 1.40
Total signal [%]	85.58 ± 1.65	86.10 ± 1.85	85.34 ± 1.75
$\frac{f(B_s^0 \to D_s^- \mu^+ \nu)}{f(B_s^0 \to D_s^{*-} \mu^+ \nu)}$ [%]	51.94 ± 1.99	50.97 ± 2.14	51.43 ± 2.09
physics bkg 1 [%]	3.94 ± 1.05	2.88 ± 1.46	4.30 ± 1.26
physics bkg 2 [%]	3.68 ± 0.39	4.59 ± 0.95	5.22 ± 1.16
Combinatorial	6.80 ± 0.23	6.82 ± 0.23	6.76 ± 0.23
$B \to DDK$ [%]	–	-0.38 ± 0.36	–
$\Lambda_b^0 \to D_s^+ \Lambda^0 \mu^- \nu$ [%]	–	–	-1.62 ± 1.26
χ^2/ndf	$84.3/89$	$82.9/88$	$79.87/88$
Fit probability [%]	62.1	63.3	72.0
Normalisation	3.73 ± 0.31	3.72 ± 0.31	3.73 ± 0.31
$\Delta(D)$ [ps^{-1}]	1.0054 ± 0.0116	1.0055 ± 0.0117	1.0054 ± 0.0116
Difference	–	0.0001	0.0000
χ^2 (ndf= 18)	19.91	19.96	19.90
Fit probability [%]	33.8	33.5	33.8
Normalisation	7.84 ± 0.11	7.93 ± 0.11	7.88 ± 0.11
$\Delta(B)$ [ps^{-1}]	-0.0115 ± 0.0053	-0.0107 ± 0.0053	-0.0111 ± 0.0053
Difference	–	0.0008	0.0004
χ^2 (ndf= 18)	10.64	10.44	10.56
Fit probability [%]	90.9	91.7	91.2

Table 3.11 – Variations in sample composition observed when including additional background components. The first part of the table reports the fractions of components obtained from the time-integrated mass fit; the second reports the results of the lifetime fit for $\Delta(D)$; the third reports the results for $\Delta(B)$. The row "Difference" reports the difference of $\Delta(D, B)$ from the nominal results (first column).

Results of the time-integrated mass fits corresponding to the first two variations are reported in Tab. 3.11. The estimated fractions of these additional components are both negative and compatible with zero. They produce very small changes in the estimation of the signal fractions and, if propagated to the rest of the analysis, on the final results. We therefore do not assign any systematic associated to them.

For the remaining three variations, we perform the full analysis on pseudo-experiments generated with the default composition (Sec. 3.7). Table 3.12 reports the resulting average differences with respect to the case when the correct composition is used. For the $\Delta(D)$ measurement, all variations produce negligible biases except for case 3 where a difference of $0.0007\,\text{ps}^{-1}$ is propagated as systematic uncertainty. For the $\Delta(B)$ measurement, variations 3 and 5 produce similar biases, resulting in a total systematic uncertainty of $0.0005\,\text{ps}^{-1}$.

	Other composition for $B_s^0 \to D_s^{**-}\mu^+\nu$	Neglecting $B_s^0 \to D_s^-\tau^+\nu X$	Adding Λ_b^0 and B_s^0 with $B \to DD$ and D^{**}
$\Delta[\Delta(D)]$	0.0007	< 0.0001	< 0.0001
$\Delta[\Delta(B)]$	0.0004	< 0.0001	0.0003

Table 3.12 – Average differences of the $\Delta(D, B)$ measurements observed when fitting with the variations considered for the sample composition a set of pseudo-experiments generated with the default composition.
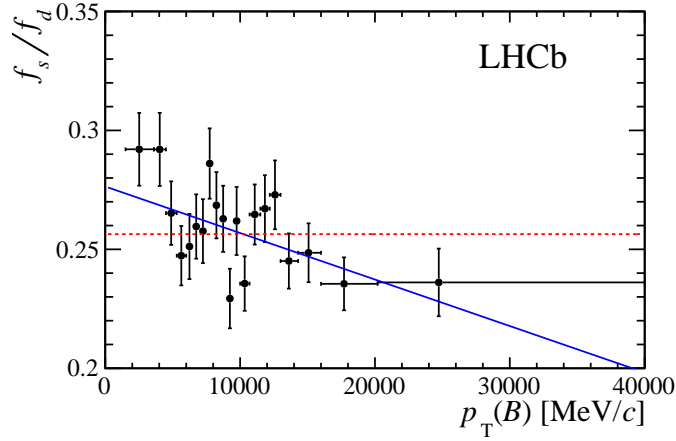
Figure 3.29 – Dependence of f_s/f_d on the transverse momentum of the B candidate, replicated from Ref. [72].

3.8.4 Mismodelling of transverse-momentum differences between B^0 and B_s^0 mesons

The difference in the p_T spectra of B_s^0 and B^0 mesons in pp collisions observed in Ref. [72] (Fig. 3.29) is not reproduced in the simulation and may alter the determination of the mass shapes, k-factor, and uniformity of the acceptance ratio. We therefore reweight the simulated B_s^0 sample according to the measured dependence as a function of the true B_s^0 transverse momentum and produce pseudo-experiments as in Sec. 3.7 which are then fit with the nominal model. Absolute average differences of $0.0018\,\text{ps}^{-1}$ and $0.0019\,\text{ps}^{-1}$ with respect to the default values are observed for $\Delta(D)$ and $\Delta(B)$, respectively, and are assigned as systematic uncertainties. This approach is preferred with respect to applying a correction to the default analysis because the observed dependence of f_s/f_d versus p_T is only marginally significant (at the level of three standard deviations) [72].

3.8.5 Decay-time acceptance and resolution for the $\Delta(D)$ measurement

The relative acceptance correction for the $\Delta(D)$ measurement is limited by the statistics of the simulated data. If the uncertainty on the acceptance is included in the fit, the uncertainty of $\Delta(D)$ increases from $0.0116\,\text{ps}^{-1}$ to $0.0126\,\text{ps}^{-1}$. The difference in quadrature of these uncertainties yields a systematic uncertainty of $0.0049\,\text{ps}^{-1}$.

Because the width of the first decay-time bins in the $\Delta(D)$ measurement is comparable with the decay-time resolution, the results might be rather sensitive to the approximations associated with the modelling of the decay-time resolution. Based on studies performed in other time-dependent analyses of b-hadron decays [75], a systematic uncertainties of $0.0039\,\text{ps}^{-1}$ is evaluated using pseudo-experiments where the D-decay-time distribution used to describe the resolution is scaled by a factor of 1.1 with respect to the nominal value.

3.8.6 Decay-time acceptance and resolution for the $\Delta(B)$ measurement

The measurement of $\Delta(B)$ aims to equalise the acceptances of the signal and reference decays with the reweighting of the D_s^- decay-time distribution (see Sect. 3.6.2). For the nominal results, the ratio of acceptances is assumed to be uniform as a function of decay time and thus neglected in Eq. (3.10) for the lifetime fit. The uniformity of such ratio is checked in simulation (see Fig. 3.19) and the reweighting method is validated by the success of the null test (Sect. 3.6.5). We thus introduce the relative acceptance of Fig. 3.19 (right) in the fit to assess a systematic uncertainty due to possible deviations from uniformity of the acceptance ratio. The effect on $\Delta(B)$ is evaluated with pseudo-experiments to be $0.0004\,\text{ps}^{-1}$.

The decay-time pdf does not include the resolution on the measurement of the B flight distance, from which the observed decay time is computed, because this is much smaller than the resolution due to the missing momentum and similar for B^0 and B_s^0 mesons. To evaluate the effect of this simplification, we perform the lifetime fit after having modified the decay-time pdf of Eq. (3.18) with the inclusion of a resolution term, $\mathscr{G}_j^{\text{FD}}$, described by a Gaussian function with standard deviation of 70 fs (see Fig. 3.22),

$$\text{pdf}_j(t) = \int k' \left(e^{-\Gamma_j k' t} \otimes \mathscr{G}_j^{\text{FD}} \right) F_j(k') dk' \qquad (j = n, d), \tag{3.21}$$

where $\otimes$ refers to a numerical time-convolution with 100 steps. As expected, no difference is seen in $\Delta(B)$ with respect to the nominal result. If the effect of decay-time resolution due to the k-factor correction is removed and only the simple exponential is kept in Eq. (3.18), the lifetime fit has a quality of $\chi^2/\text{ndf} = 10.6/18$ and the difference of $\Delta(B)$ from the nominal results is found to be $0.0004\,\text{ps}^{-1}$. Compatible results are also obtained on pseudo-experiments. The small impact of the resolution in the lifetime fit can be explained qualitatively by considering the variable width of the decay time bins: even if the decay time resolution worsens as the decay time increases, the increasing width of the decay-time bin compensates for it by limiting bin-to-bin migrations. We consider the total systematic due to the decay-time resolution to be $0.0004\,\text{ps}^{-1}$.

3.8.7 Feed-down from B_c^+ decay

Candidates B_s^0 produced in the decay of a B_c^+ meson can introduce a bias in the lifetime measurement because their reconstructed decay length is calculated with respect to the primary vertex, which may likely corresponds to the B_c^+ production vertex, measuring effectively the sum of the two decay times. Reference [76] reports the measurement

$(f_c/f_s)\mathscr{B}(B_c^+ \to B_s^0\pi^+) = (2.37 \pm 0.37) \times 10^{-3}$, where f_c/f_s is the ratio of fragmentation probabilities of B_c^+ and B_s^0 mesons. From this measurement, the fraction of B_s^0 mesons coming from B_c^+ decays in our sample, $f_{B_c^+}$, is estimated to be about 1%, assuming a similar efficiency between selecting secondary and prompt B_s^0 decays and considering the expectation $\mathscr{B}(B_c^+ \to B_s^0 X)/\mathscr{B}(B_c^+ \to B_s^0\pi^+) \approx 4$ [77]. Decays of a B_c^+ meson into a $B^0 X$ final state involves a $c \to d$ transition and are more suppressed than $B_c^+ \to B_s^0 X$ decays; therefore, we neglect B_c^+ feed-down in the B^0 sample. The impact of B_c^+ feed-down on $\Delta(B)$ is calculated from a sample of simulated $B_c^+ \to B_s^0(\to D_s^-\mu^+ X)\pi^+$ decays. The bias on $\Delta(B)$ when neglecting a 1% of secondary B_s^0 is found to be $0.0010\,\mathrm{ps}^{-1}$. This corresponds to a bias on the lifetime of $0.0025\,\mathrm{ps}$, in agreement with what is estimated in Ref. [77].

The impact of B_c^+ feed-down on $\Delta(B)$ can also be calculated with some reasonable approximations [78]: (i) the decay chain happens in one dimension, along the z direction; (ii) secondary and prompt B_s^0 decays have the same decay-time acceptance. With these assumptions, the decay-time distribution of secondary B_s^0 meson is the following time-convolution:

$$g(t) = A_{B_c^+}(t)\frac{e^{-t/\tau_s^{\mathrm{fs}}}}{\tau_s^{\mathrm{fs}}} \otimes \frac{e^{-t/\tau_{B_c^+}}}{\tau_{B_c^+}} = A_{B_c^+}(t)\frac{e^{-t/\tau_s^{\mathrm{fs}}} - e^{-t/\tau_{B_c^+}}}{\tau_s^{\mathrm{fs}} - \tau_{B_c^+}}, \tag{3.22}$$

with $\tau_{B_c^+} = 0.507 \pm 0.009\,\mathrm{ps}$ [19] and $A_{B_c^+}$ the acceptance for B_s^0 from B_c^+ decays. The bias on the measured B_s^0 lifetime, when neglecting the secondary component, is therefore

$$\delta = f_{B_c^+}\left[\int_0^\infty t\,g(t)\,dt - \langle t_s \rangle\right] \approx f_{B_c^+}\left(\langle t_{B_c^+} \rangle - \langle t_s \rangle\right) = 0.0025\,\mathrm{ps}, \tag{3.23}$$

where $\langle t \rangle$ is the mean value of the decay time distribution, taking the acceptance into account. This corresponds to a bias of $0.0010\,\mathrm{ps}^{-1}$ on $\Delta(B)$, which we take as systematic uncertainty.

This number is crosschecked by changing the pdf of the ratio of the yields, allowing for 1% of $B_c^+ \to B_s^0 X$ decays. This leads to a systematic of $0.0010\,\mathrm{ps}^{-1}$, compatible with the above calculation.

3.8.8 Other systematic uncertainties

Because of $B_{(s)}^0 - \overline{B}_{(s)}^0$ oscillations, nonzero production and detection asymmetries change the exponential decay-time distribution and alter the interpretation of the measured value of $\Delta(B)$. Indicating with N ($\overline{N}$) the number of produced $B_{(s)}^0$ ($\overline{B}_{(s)}^0$) and with ϵ^+ (ϵ^-) the detection efficiency of the $D_{(s)}^-\mu^+$ ($D_{(s)}^+\mu^-$) final state, the total rate of untagged decays, assuming no CP violation, can be written as

$$\Gamma_{\mathrm{tot}} \propto e^{-\Gamma_{d,s}t}\left[(N+\overline{N})(\epsilon^+ + \epsilon^-)\cosh(\Delta\Gamma_{d,s}t/2) + (N-\overline{N})(\epsilon^+ - \epsilon^-)\cos(\Delta m_{d,s}t)\right]. \tag{3.24}$$

For small asymmetries, *i.e.* $(N-\overline{N})/(N+\overline{N})$ and $(\epsilon^+ - \epsilon^-)/(\epsilon^+ + \epsilon^-)$ of the order of few 10^{-2}, the effect on the measured lifetimes is completely negligible.

The imperfect knowledge of the length scale of the detector translates into a systematic

uncertainty on the absolute value of the decay length. Previous analyses [79] have shown that this results in a 0.02% relative uncertainty on the decay-time scale (a precision of about $2\,\mu m$ on the flight distance of B and D mesons), which corresponds to an uncertainty on $\Delta(B, D)$ of below $0.0002\,\mathrm{ps}^{-1}$. This is much smaller than other systematic uncertainties and is therefore neglected.

3.8.9 Consistency checks

We check the consistency of the results by repeating the full analysis in subsets of the data selected according to criteria that may potentially induce biases on the measured width difference:

- magnet polarities and data-taking year (four independent subsets). This is a standard criterion that probes potential systematic dependencies on the overall conditions of data taking and tracking;

- trigger categories for Hlt1 (`Hlt1TrackMuon` exclusive, `Hlt1SingleMuonHighPT` inclusive and `Hlt1TrackAllL0` but NOT `Hlt1SingleMuonHighPT`) and Hlt2 (`Hlt2TopoMu{2,3}BodyBBDT` exclusive, and `Hlt2TopoMu4BodyBBDT` inclusive), where the categories are grouped in an exclusive way to allow sufficient statistics. As the trigger choice may have an effect on the acceptances, the ratio of acceptances is also included in the fit of $\Delta(B)$;

- number of reconstructed primary vertices in the event (events with 1 PV, 2 PV's, 3 or more PV's). This criterion checks against effects due to wrongly associated primary vertices, which may bias the B decay-length measurement;

- number of tracks associated with the candidate's PV (less than 35, between 35 and 50, more than 50). This variable probes effects associated with the quality of the primary vertex, which is correlated with the number of tracks associated with it, and the probability to have a random muon faking the B vertex when associated with the D candidate;

- momentum of the $D_{(s)}\mu$ pair (smaller than $75\,\mathrm{GeV}/c$, between 75 and $120\,\mathrm{GeV}/c$, larger than $120\,\mathrm{GeV}/c$);

- transverse momentum of the $D_{(s)}\mu$ pair (smaller than $6.5\,\mathrm{GeV}/c$, between 6.5 and $9.3\,\mathrm{GeV}/c$, larger than $9.3\,\mathrm{GeV}/c$). This criterion checks for residual effects associated with the differences in p_T spectra between B^0 and B_s^0 mesons.

The results of the analyses of these subsets are summarised in Fig. 3.30. Resulting values of $\Delta(B)$ are consistent with one another and their weighted average are consistent with the nominal values. The only deviation is observed in the $\Delta(B)$ values as functions of B transverse momentum, which differ by about 1σ. We attribute this shift to the dependence of f_s/f_d on $p_T(B)$ because it is of similar magnitude and in the same direction as that observed in Fig. 3.30 (bottom-left); indeed, the values of $\Delta(B)$ obtained by using the acceptance ratio corrected for the dependence of f_s/f_d on $p_T(B)$ is closer to the weighted average.

Figure 3.30 also shows the results of the measurement when considering only one of two components $B^0{}_{(s)} \to D^-_{(s)} \mu^+ \nu$ and $B^0{}_{(s)} \to D^{*-}_{(s)} \mu^+ \nu$ as the signal. The two results are in agreement between them and with the nominal value.

Results of the same checks for the measurement of $\Delta(D)$ are reported in Fig. 3.31. Values of $\Delta(D)$ are consistent with one another.
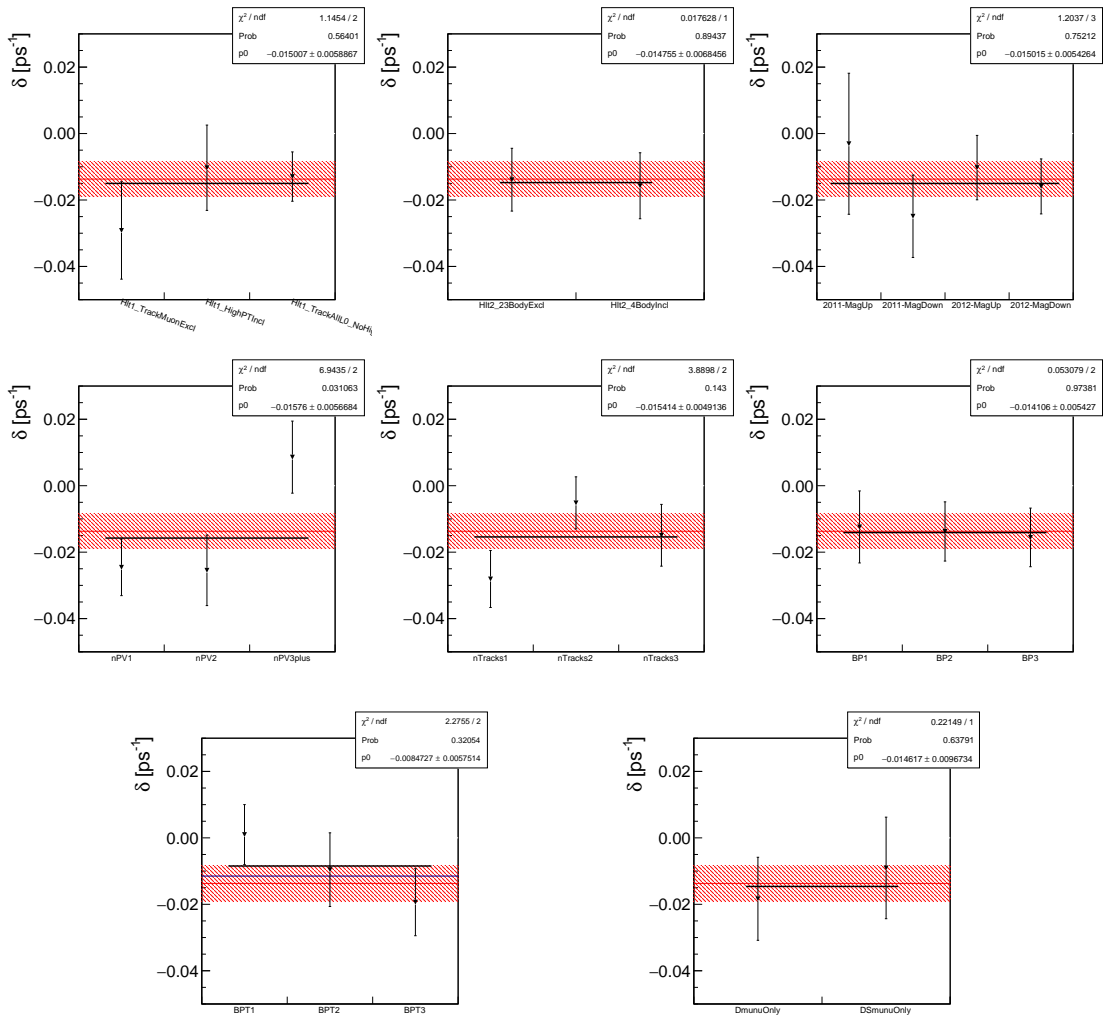
Figure 3.30 – $\Delta(B)$ values observed in the consistency checks as functions of (from top-left to bottom-right) different Hlt1 and Hlt2 requirements, magnet polarity and data-taking year, primary vertex multiplicity, track multiplicity of the PV, $D_{(s)}\mu$ momentum, $D_{(s)}\mu$ transverse momentum, the two signal components analysed separately. The red line indicates the nominal value, the bands represent the uncertainty; the black line is the weighted average of the values of $\Delta(B)$. The blue line in the bottom-left plot represents the value of $\Delta(B)$ obtained by using the acceptance ratio corrected for the dependence of f_s / f_d on $p_T(B)$.
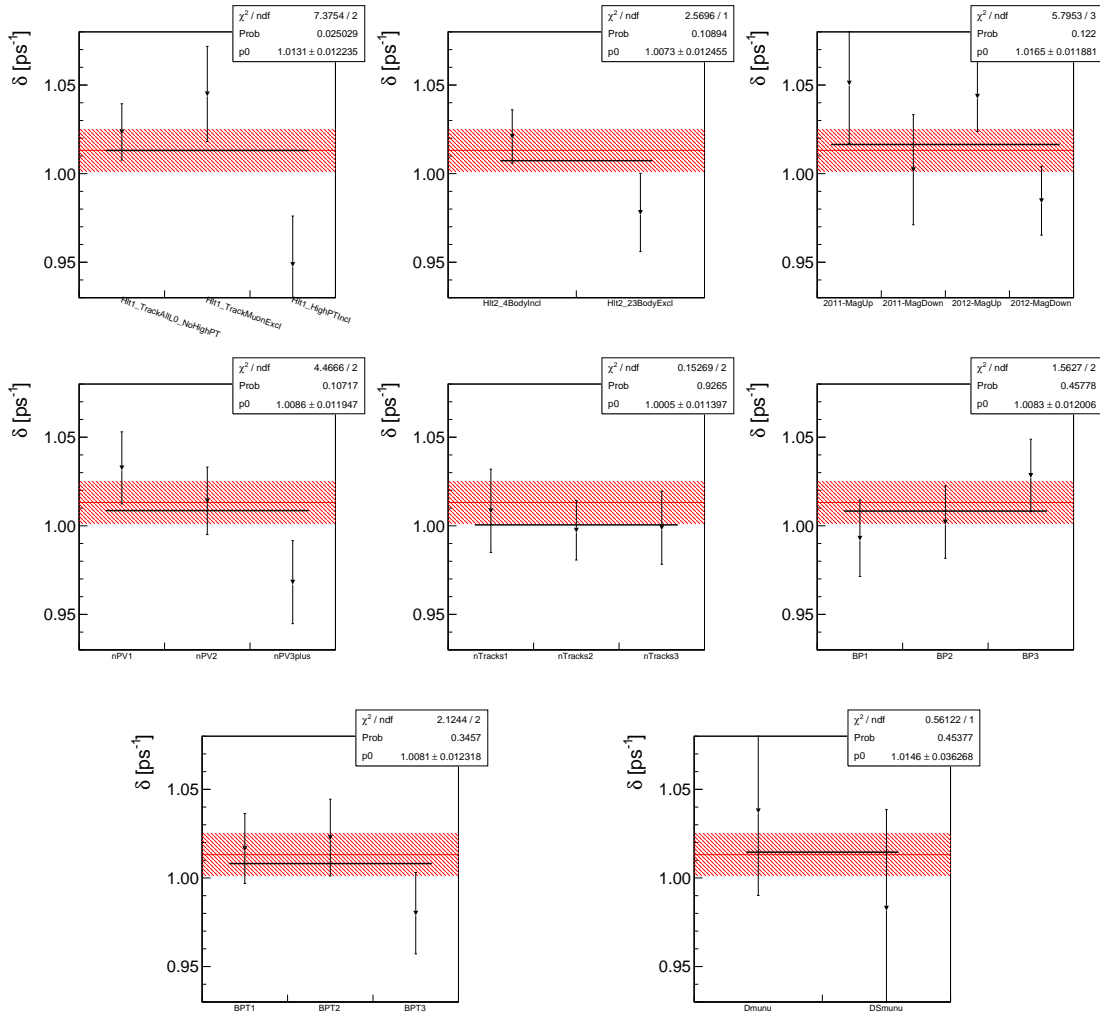
Figure 3.31 – $\Delta(D)$ values observed in the consistency checks as functions of (from top-left to bottom-right) different Hlt1 and Hlt2 requirements, magnet polarity and data-taking year, primary vertex multiplicity, track multiplicity of the PV, $D_{(s)}\mu$ momentum, $D_{(s)}\mu$ transverse momentum, the two signal components analysed separately. The red line indicates the nominal value, the bands represent the uncertainty; the black line is the weighted average of the values of $\Delta(D)$.

Figure 3.32 – (left) Comparison of the flavour-specific B_s^0 lifetime measurements and average listed in Table 3.13. The blue band corresponds to the new world average. (right) Contours of $\Delta(\ln(L)) = 0.5$ (39% CL for the enclosed 2D regions, 68% CL for the bands) in the plane (Γ_s, $\Delta\Gamma_s$). The average of all $B_s^0 \to J/\psi\phi$, $B_s^0 \to J/\psi K^+K^-$ and $B_s^0 \to \psi(2S)\phi$ measurements is shown as the red contour, and the constraints given by the effective lifetime measurements with CP-odd final states ($B_s^0 \to J/\psi f_0(980)$ and $B_s^0 \to J/\psi\pi^+\pi^-$), 1.668 ± 0.024 ps, CP-even final states ($B_s^0 \to J/\psi\eta$ and $B_s^0 \to D_s^+D_s^-$), 1.422 ± 0.023 ps, and flavour-specific final states, 1.526 ± 0.011 ps, are shown as the green, pink and blue bands, respectively. The average taking all constraints into account is shown as the black filled contour. The gray band is a theory prediction $\Delta\Gamma_s = 0.088 \pm 0.020$ ps^{-1} which assumes no new physics in B_s^0 mixing [81]. Figure by the HFLAV collaboration [80].

3.9 Summary

We report on a measurement of the difference between the decay widths of the B_s^0 and B^0 mesons, $\Delta(B)$, and the width difference between the D_s^- and D^- mesons, $\Delta(D)$, using semileptonic $B_s^0 \to D_s^-(\to K^+K^-\pi^-)\mu^+\nu X$ and $B^0 \to D^-(\to K^+K^-\pi^-)\mu^+\nu X$ decays partially reconstructed in the full data set collected in Run I by LHCb at $\sqrt{s} = 7$ and 8 TeV and corresponding to an integrated luminosity of 3 fb^{-1}. The final results are reported in Table 3.13.

Using the known value of the B^0 lifetime as input [19], we obtain a measurement of the flavour-specific lifetime of the B_s^0 meson, $\tau_s^{\text{fs}} = 1.547 \pm 0.013\,(\text{stat}) \pm 0.010\,(\text{syst}) \pm 0.004\,(\tau_{B^0})$ ps, where the last uncertainty is due to the uncertainty of the B^0 lifetime. This result is consistent with and more precise than the other most precise determinations by the D0 and LHCb collaborations and is also consistent with the 2016 world's average value. The HFLAV collaboration [80] makes averages of different measurements and computed the new flavour-specific B_s^0 lifetime average, showing that our measurement improves on the flavour-specific B_s^0 lifetime by about 20%, as shown in Figure 3.32 (left).

This result allows to put constraints on the values of Γ_s and $\Delta\Gamma_s$, as shown in Figure 3.32 (right). Constraints due the flavour-specific lifetime measurements correspond to the blue band. The precision on Γ_s and $\Delta\Gamma_s$ have also improved between the averages of 2016 and 2017; however, this is also due to other non-flavour-specific B_s^0 lifetime measurements.

With the $\Delta(D)$ measurement, and using the known value of the D^- lifetime [19], we obtain a

$\Delta(B)$		$-0.0115 \pm 0.0053\,\text{(stat)} \pm 0.0041\,\text{(syst)}\,\text{ps}^{-1}$
$\Delta(D)$		$1.0131 \pm 0.0117\,\text{(stat)} \pm 0.0065\,\text{(syst)}\,\text{ps}^{-1}$
τ_s^{fs}	This measurement	$1.547 \pm 0.013\,\text{(stat)} \pm 0.010\,\text{(syst)} \pm 0.004(\tau_{B^0})\,\text{ps}$
	LHCb 2014 [68]	$1.535 \pm 0.015\,\text{(stat)} \pm 0.014\,\text{(syst)}\,\text{ps}$
	D0 2015 [67]	$1.479 \pm 0.010\,\text{(stat)} \pm 0.021\,\text{(syst)}\,\text{ps}$
	HFLAV 2016 [80]	$1.516 \pm 0.014\,\text{ps}$
	HFLAV 2017 [80]	$1.526 \pm 0.011\,\text{ps}$
$\tau_{D_s^-}$	This measurement	$0.5064 \pm 0.0030\,\text{(stat)} \pm 0.0017\,\text{(syst)} \pm 0.0017(\tau_{D^-})\,\text{ps}$
	FOCUS [82]	$0.5074 \pm 0.0055\,\text{(stat)} \pm 0.0051\,\text{(syst)}\,\text{ps}$
	PDG 2017 [19]	$0.500 \pm 0.007\,\text{ps}$

Table 3.13 – Final results for measurements of $\Delta(B)$ and $\Delta(D)$. The flavour-specific B_s^0 lifetime and D_s^+ lifetime are reported along with world's leading results and averages. The τ_s^{fs} value by HFLAV includes our measurement in the 2017 average.

determination of the D_s^- lifetime, $\tau_{D_s^-} = 0.5064 \pm 0.0030\,\text{(stat)} \pm 0.0017\,\text{(syst)} \pm 0.0017(\tau_{D^-})\,\text{ps}$. This value is consistent with and more precise than the world's best determination from the FOCUS collaboration and improves upon the world's average value by almost a factor two, as shown in Tab. 3.13.

Finally, the measured values of $\Delta(D)$ and $\Delta(B)$ are independent of any lifetime measurement. Therefore, any improvement on the B^0 and D^- lifetimes may translate in a shift for the values of τ_s^{fs} and $\tau(D_s^-)$, as well as an improvement on the uncertainty due to this external lifetime input.

4 Feasibility study of a D^0 lifetime measurement

4.1 Introduction

The success of the measurement of the D_s^- and flavour-specific B_s^0 lifetime highlights a new method to perform precise measurements of different observables. By computing the ratio of the same observable in two different decays with a similar topology, it is possible to equalise the selection in order to have the same efficiency for each decay mode. This method could also be used for a wide range of other measurements, the more straightforward being cross-sections, but in this Chapter we will measure once more the difference between two decay widths.

Measurements of charm hadrons lifetimes are currently less valuable than for bottom hadrons, because the theoretical predictions from HQE discussed in Section 1.2.2 are still far from current experimental determinations. However, reducing the uncertainty on the ratio of the D^0 and D^- lifetimes for example, would still be useful in order to tune the parameters of an effective model or to eliminate an effective model which would not correctly represent the physics of charm hadrons.

The current best determination of the D^0 lifetime is 0.4101 ± 0.0015 ps, while the D^- lifetime is measured to be 1.040 ± 0.007 ps [19]. Thus a measurement of the difference between the decay widths of the D^0 and D^- mesons,

$$\Delta(D)' = \Gamma(D^0) - \Gamma(D^-), \tag{4.1}$$

can still improve the precision on $\tau(D^0)$; the uncertainty on the D^0 lifetime $\sigma_{\tau_{D^0}}$ due to the uncertainty on the D^- lifetime $\sigma_{\tau_{D^-}}$ is

$$\sigma_{\tau_{D^0}} = \sigma_{\tau_{D^-}} \times \left(\frac{\tau_{D^0}}{\tau_{D^-}} \right)^2, \tag{4.2}$$

which amounts to 0.0011 ps. Although this uncertainty is quite large, a precise $\Delta(D)'$ measurement is also interesting as one can compute τ_{D^0}/τ_{D^-} with a good precision from $\Delta(D')$ and τ_{D^-}. This ratio is particularly interesting as it can be directly compared with predictions from HQE or other effective models.

The method is the same as in Chapter 3. We use a sample of about 1.8 million $B^0 \to D^{*-}(\to \overline{D}^0(\to K^+\pi^-)\pi^-)\mu^+\nu X$ and 2.7 million $B^0 \to D^-(\to K^+\pi^-\pi^-)\mu^+\nu X$ candidates (the decay used as a control channel for the null-tests of Chapter 3) collected by LHCb during Run I. We also determine the D^0 and D^- signal yields as functions of the D decay time using a fit to the corrected B mass and equalise the decay-time acceptances of the two channels. However, the D decay-time resolution is significantly different for the two decays and needs to be studied with more care.

This chapter is structured as follows. First, the selection of the data samples is presented in Section 4.2 and the D^0 sample composition is studied with simulation and determined with a fit to the B corrected mass in Section 4.3. Section 4.4 presents the decay-time fit used to determine $\Delta(D)'$. Systematics uncertainties are discussed in Section 4.5 and results are summarised in Section 4.6.

4.2   Selection

As for the $\Delta(D, B)$ measurements, we use the entire LHCb Run I data set to perform this analysis.

4.2.1   Pre-selection (stripping)

To reconstruct the $B^0 \to D^{*-}(\to \overline{D}^0(\to K^+\pi^-)\pi^-)\mu^+\nu X$ decay, a D^0 candidate is built from a $K\pi$ pair and combined with a third slow pion track (denoted π_s in the following) to form a D^* originating from the same vertex. This resonance is finally combined with a muon originating from a common displaced vertex.

Collected data goes through the stripping pre-selection and candidate decays are reconstructed from the `Bd2DstarMuNuTight` line of `Stripping21r{0,1}`. The details of this selection are summarised in Table 4.1 and the variables not already introduced in Section 3.2.1 are described below.

- As the soft pion is not needed to reconstruct the D^0, it does not need to have a large transverse momentum to avoid D^0 combinatorial events, hence the looser criteria; other criteria are also loose or not applied.

- The minimum distance from the PV ensures the tracks come from the $B^0 \to D^{*-}\mu^+\nu$ decay and not directly from the PV.

- The two muon booleans, `HasMuon` & `IsMuon`, indicate if there are hits in the muon stations and if they are consistent with a muon, respectively.

- The D^* resonance needs to have a large p_T, but the quality of the vertex is not as important as for the D^0, as the combination is made with a soft pion.

- The B^0 is required to have flown with respect to the primary vertex, to reduce combinatorial background.

Figure 4.1 – Distributions of (left) $K^-\pi^+$ mass (D^0 sample) and (right) $K^+\pi^-\pi^-$ mass (D^- sample) for the candidates reconstructed after stripping for opposite-sign and same-sign data in 2012 magnet-down data. Plots from 2011 and magnet-up data show similar features.

The pre-selection of $B^0 \to D^-(\to K^+\pi^-\pi^-)\mu^+\nu X$ decays uses the same stripping line as in Section 3.2.1, but with a more recent version of the stripping software (`Stripping21r{0,1}`). Between these versions, the values of the stripping criteria changed significantly and are reported in Table 4.1. This pre-selection also requires that at least one line among a set of specific Hlt2 lines is triggered; all lines considered in this analysis are included in this set. Same-sign events are also reconstructed to study the combinatorial background.

Figure 4.1 shows the $K^-\pi^+/K^+\pi^-\pi^-$ mass distributions of the reconstructed candidates. Signal candidates amount to 15.2×10^6 (3.67×10^6) $D^0 \to K^-\pi^+$ and 30.7×10^6 (8.29×10^6) $D^- \to K^+\pi^-\pi^-$ decays for opposite-sign (same-sign), including backgrounds.

Figure 4.2 shows the $K^+\pi^-\pi^-\mu^+$ invariant mass, represented as the $D^{(*)}\mu$ invariant mass and corrected B mass distributions. In all distributions and mass ranges the same-sign candidates are fewer than opposite-sign candidates. With the new stripping selection of the $B^0 \to D^-(\to K^+\pi^-\pi^-)\mu^+\nu X$ sample, it is possible to evaluate the $D\mu$ mass spectrum above $6\,\mathrm{GeV}/c^2$. The small differences above $5.5\,\mathrm{GeV}/c^2$ between the OS and SS samples suggest the same-sign sample can be used as a proxy for the combinatorial background. The small enhancement around $5.3\,\mathrm{GeV}/c^2$ is once again due to fully reconstructed B decays. For the D^0 sample, it is impossible to compare OS and SS data in this spectrum, because the $D^*\mu$ invariant mass is rejected above $5.280\,\mathrm{GeV}/c^2$. The amount of physics background events can however still be estimated from the differences between OS and SS samples in the D^0 mass spectrum sidebands. In the corrected mass distributions, the differences between the samples are more pronounced and the B-signal region peaks in a narrower region thanks to the kinematic correction.

4.2.2 Offline selection

Following the stripping, candidates are filtered according to the selection at trigger level, by requiring the same lines as in Section 3.2.2. The candidates are then required to satisfy the offline selection from Table 4.2. The goal of the selection is to reduce the different backgrounds

Quantity	D^0 requirement (Bd2DstarMuNuTight)	D^- requirement (b2DpMuXB2DMuNuX)
$p_T(\mu)$	> 800 MeV/c	> 1000 MeV/c
$p_T(K)$, $p_T(\pi)$	> 350 MeV/c	> 250 MeV/c
$p_T(\pi_s)$	> 110 MeV/c	–
$p(\mu)$	> 2.0 GeV/c	> 6.0 GeV/c
$p(K)$, $p(\pi)$	> 2.0 GeV/c	> 2.0 GeV/c
Minimum IP $\chi^2(\mu,\pi,K)$	–	> 4.0
Track $\chi^2/\mathrm{ndf}(\mu,\pi,K)$	–	< 4.0
Ghost probability (μ, π, K)	< 0.5	< 0.5
Min. distance from PV(π,π_s,K)	> 0.04 mm	–
PIDmu(μ)	> -5.0	> 0.0
Muon ID	HasMuon & IsMuon	–
PIDK(K)	> -5.0	> -5.0
PIDK(π)	–	< 20.0
D daughters' $\sum p_T$	–	> 1.8 GeV/c
D vertex χ^2/ndf	< 10.0	< 6.0
D χ^2/ndf separation from PV	> 50	> 25
$m(D)$	$\in [1804.83, 1924.83]$ MeV/c^2	$\in [1789.62, 1949.62]$ MeV/c^2
D^* daughters' $\sum p_T$	> 1.25 GeV/c	–
D^* vertex χ^2/ndf	< 20	–
$m(D^*)$	$\in [1940.26, 2080.26]$ MeV/c^2	–
B vertex χ^2/ndf	< 25	< 6.0
B DIRA	> 0.999	> 0.999
$m(D\mu)$	$\in [3.000, 5.280]$ GeV/c^2	$\in [0, 9999]$ GeV/c^2
$v_z(D) - v_z(B)$	> -2.5 mm	> -1.0 mm
$v_z(B) - v_z(PV)$	> 0.5 mm	–

Table 4.1 – Summary of stripping selections for (left) D^0 and (right) D^- samples. For the D^- sample, the requirements are different from the ones presented in Table 3.1.

Figure 4.2 – Distributions of (top) $D^- \mu^+ / D^{*-} \mu^+$ invariant mass and (bottom) corrected B mass for (left) $B^0 \to D^{*-}(\to \overline{D}^0(\to K^+ \pi^-)\pi^-)\mu^+ \nu X$ and (right) $B^0 \to D^-(\to K^+ \pi^- \pi^-)\mu^+ \nu X$ candidates reconstructed after stripping in 2012 magnet-down data. Plots from 2011 and magnet-up data show similar features.

and to minimise difference between the SS and OS samples in the sideband of the $D^{(*)}\mu$ invariant mass. However, because of the tight cuts on the B mass during the stripping, the effects of the selection cannot be efficiently visualised on the $D^*\mu$ invariant mass spectrum for the D^0 sample; the comparison is therefore done on the D^0 mass spectrum. Physics backgrounds are also reduced by analysing an inclusive sample of $D^{*-} \to \overline{D}^0(\to K^+ \pi^-)\pi^-$ decays. In order to reduce the differences in the time-dependent efficiencies of each sample, selection criteria are equalised between the two samples when possible, resulting in a different final selection for the $B^0 \to D^-(\to K^+ \pi^- \pi^-)\mu^+ \nu X$ sample compared to the $\Delta(D, B)$ measurement.

Known sources of background from misreconstructed decays are suppressed with mass vetoes. Candidate $B_s^0 \to \psi(\to \mu^+ \mu^-)\phi(\to K^+ K^-)$ decays, where one of the muons from the ψ is misidentified as a pion and a kaon is misidentified as a pion, are removed by vetoing the corresponding regions in dimuon mass computed after assigning the muon mass to the charged particle originally identified as a pion. For the $B^0 \to D^-(\to K^+ \pi^- \pi^-)\mu^+ \nu X$, the $\Lambda_b^0 \to \Lambda_c^+(\to pK^- \pi^+)\mu^- \nu X$ mass veto is applied; no such signal appears for the $B^0 \to D^{*-}(\to \overline{D}^0(\to K^+ \pi^-)\pi^-)\mu^+ \nu X$ decay.

Requirements on (transverse) momenta and particle identification criteria help to reduce the non-D and non-D^* backgrounds. Most of these are tighter variants of the pre-selection criteria and may slightly reduce the signal for a greater gain in signal-to-background ratio. Backgrounds are further reduced by criteria on the quality of the D and B mesons vertices.

To reduce decays of a b hadron into $D^* D$, where the D decays semileptonically, we use the same linear requirement as in Section 3.2.2: $p_\perp(D)[\text{MeV}/c] > 1500 + 1.1 \times (m_{\text{corr}}[\text{MeV}/c^2] -$

Quantity	D^0 requirement	D^- requirement
ProbNNk(K)	> 0.2	> 0.2
ProbNNpi(π)	> 0.5	> 0.5
ProbNNpi(π_s)	> 0.1	–
ProbNNmu(μ)	> 0.1	> 0.2
IP $\chi^2(K, \pi)$	> 18	–
$p(K)$	$> 3\,\text{GeV}/c$	$> 3\,\text{GeV}/c$
$p(\pi)$	$> 5\,\text{GeV}/c$	$> 5\,\text{GeV}/c$
$p(\mu)$	$> 6\,\text{GeV}/c$	$> 6\,\text{GeV}/c$
$p_T(K),\ p_T(\pi)$	$> 500\,\text{MeV}/c$	$> 500\,\text{MeV}/c$
$p_T(\mu)$	$> 1\,\text{GeV}/c$	$> 1\,\text{GeV}/c$
$p(D^*)$	$> 2\,\text{GeV}/c$	–
$\log(\text{IP}(D))$	> -3.0	–
D vertex χ^2/ndf	< 6.0	< 6.0
B vertex χ^2/ndf	< 6.0	–
$m(Kp\pi)$	–	$\notin [2260, 2310]\,\text{MeV}/c^2$
$m(D)$	$\in [1840, 1890]\,\text{MeV}/c^2$	$\in [1850, 1890]\,\text{MeV}/c^2$
$m(D^*)$	$\in [1960.26, 2060.26]\,\text{MeV}/c^2$	–
$m(D^*) - m(D)$	$\in [144, 147]\,\text{MeV}/c^2$	–

$p_\perp(D)\,[\text{MeV}/c]$	$> 1500 + 1.1 \times (m_{\text{corr}}[\text{MeV}/c^2] - 4500)$
t_D	$> 0.0\,\text{ps}$
m_{corr}	$[3, 8.5]\,\text{GeV}/c^2$
$m(D^- \mu^+)$	$\in [3.1, 5.2]\,\text{GeV}/c^2$
$m(\mu^+ \mu^-)$	$\notin [3.040, 3.160]\,\text{GeV}/c^2$
	$\notin [3.635, 3.735]\,\text{GeV}/c^2$

Table 4.2 – Summary of offline selection criteria for the (left) D^0 and (right) D^- samples. See text for motivations.
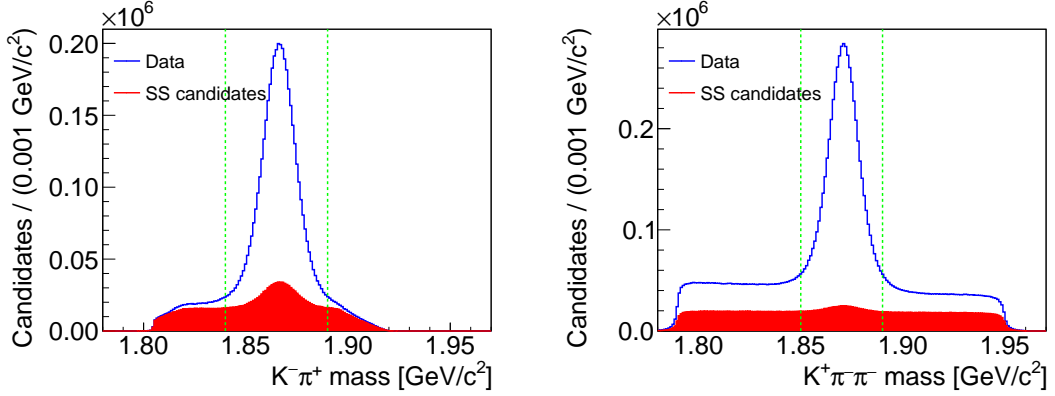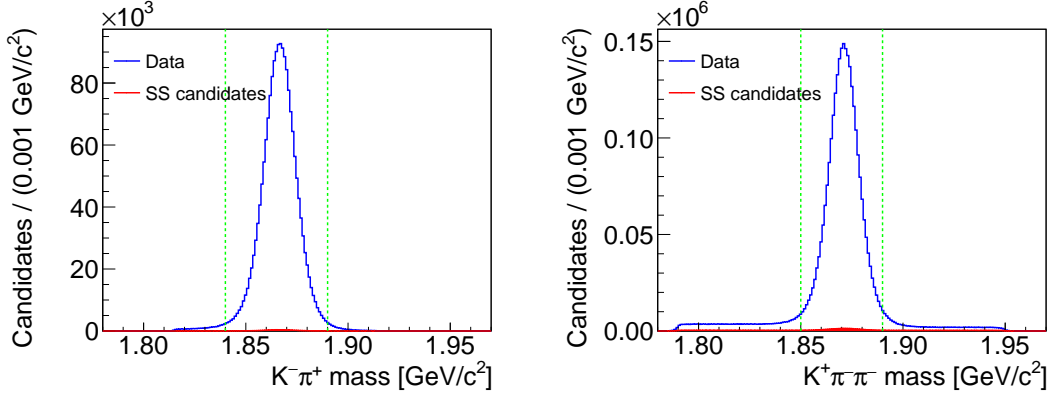
Figure 4.3 – Distributions of (left) $K^-\pi^+$ mass (D^0 sample) and (right) $K^+\pi^-\pi^-$ mass (D^- sample) for the candidates passing the final selection. Events above the green vertical line are removed by the selection.

4500). The parameters of this linear condition have been varied without significant improvement on its efficiency and is thus chosen to be the same as for $B^0 \to D^-(\to K^+\pi^-\pi^-)\mu^+\nu X$ decays. The simulation estimates that this requirement removes about 40% of these backgrounds while retaining about 94% of the signal.

In order to reduce the number of D^* coming directly from the pp interaction and associated to a random muon, a requirement is put on the IP of the D^0 meson, reducing such decays by about 95%. The daughters of the D^0 are also required to not come directly from the PV with a minimum on their IP χ^2.

As the D^0 mass is slightly lower than the D^- mass, the mass ranges are chosen to be [1.84,1.89] GeV/c^2 and [1.85,1.89] GeV/c^2, respectively. In the D^0 case, further requirements are added on the mass of the resonance, required to be in the range [1960.26, 2060.26] MeV/c^2 and the difference between the D^* and D^0 masses is set to be between 144 and 147 MeV/c^2 to greatly reduce the combinatorial D^* background.

Figures 4.3 and 4.4 show the resulting $K^+\pi^-/K^+\pi^-\pi^-$ and $K\pi\pi\mu$ mass distributions, respectively. The green line shows the upper limit of the $D^{(*)}\mu$ invariant mass range, 5.2 GeV/c^2, chosen to comply with the D^0 sample stripping selection and to remove the peak at 5.3 GeV/c^2, due to fully reconstructed background decays. A total of 1.80×10^6 $B^0 \to D^{*-}(\to \overline{D}^0(\to K^+\pi^-)\pi^-)\mu^+\nu X$ and 2.67×10^6 $B^0 \to D^-(\to K^+\pi^-\pi^-)\mu^+\nu X$ signal candidates meet the final selection criteria. Combinatorial background is greatly reduced and differences between OS and SS data fully disappear above 6 GeV/c^2 in the $D\mu$ mass spectrum for the D^- sample, validating the SS data as a good template for the combinatorial background. The amount of SS data is only 0.5% and 1.0% for the D^0 and D^- sample, respectively, compared to the OS data.

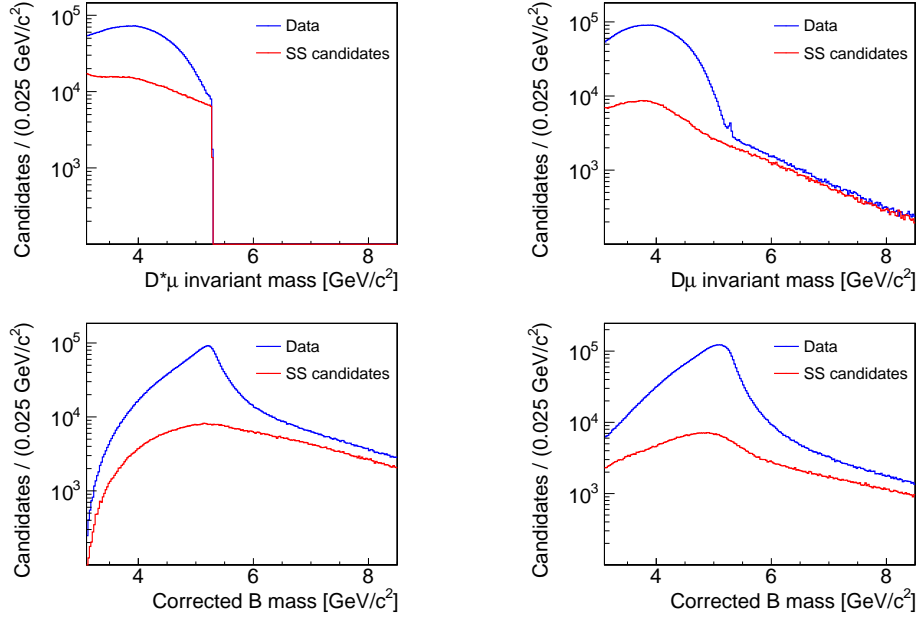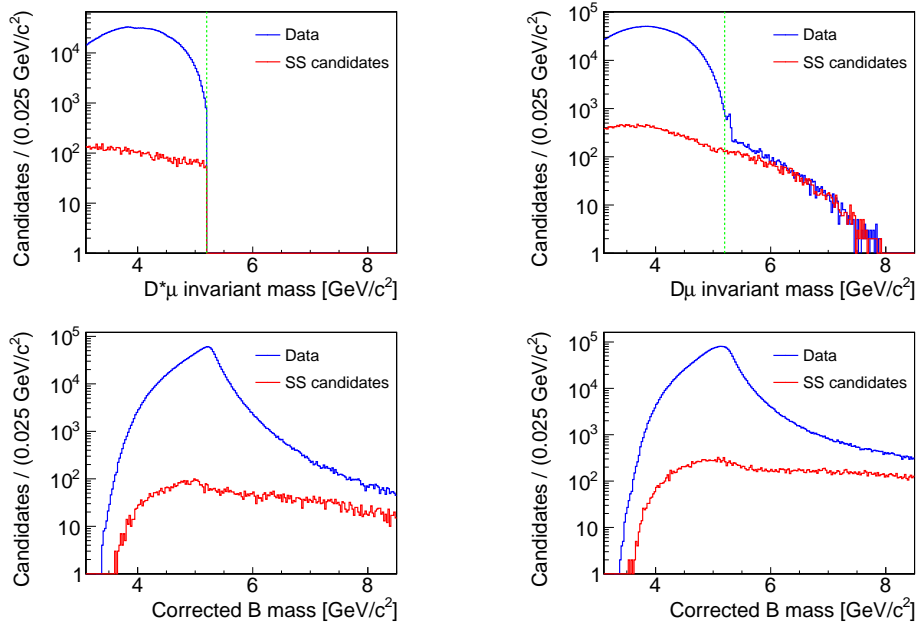Figure 4.4 – Distributions of (top) $D^-\mu^+/D^{*-}\mu^+$ invariant mass and (bottom) corrected B mass for (left) $B^0 \to D^{*-}(\to \overline{D}^0(\to K^+\pi^-)\pi^-)\mu^+\nu X$ and (right) $B^0 \to D^-(\to K^+\pi^-\pi^-)\mu^+\nu X$ candidates passing the final selection.

4.3   Determination of the sample composition

We use a fit to the corrected B^0 mass to discriminate between signal and background and extract the signal yields. First, the possible physics backgrounds are studied with simulation.

4.3.1   Simulation and expected sample composition

Simulation samples are used to describe the signal and main background distributions, as well as to suppress the physics background by refining the selection. Each sample is split into up and down magnet polarities and into 2011 and 2012 subsamples, in proportions similar to those present in data. After the full selection, the signal decays samples amount to 588 000 for $B^0 \to D^{*-}(\to \overline{D}^0(\to K^+\pi^-)\pi^-)\mu^+\nu X$ and 163 000 for $B^0 \to D^-(\to K^+\pi^-\pi^-)\mu^+\nu X$; the backgrounds samples amount to 9 000 for $B^+ \to \overline{D}^0(\to K^+\pi^-)\mu^+\nu X$ and 31 000 for $B^+ \to D^-(\to K^+\pi^-\pi^-)\pi^+\mu^+\nu X$. The signal yield slightly increased for the D^- signal decay with respect to Table 3.3 thanks to the new stripping selection; the B^+ background increased significantly more because of the addition of a 2011 sample. In addition, a small inclusive sample of inclusive $D^{*-} \to \overline{D}^0(\to K^+\pi^-)\pi^-$ decays is studied.

Table 4.3 lists the different modes included in the inclusive $B^0 \to D^{*-}(\to \overline{D}^0(\to K^+\pi^-)\pi^-)\mu^+\nu X$ decay, along with relative fractions and decay model. The $B^0 \to D^-(\to K^+\pi^-\pi^-)\mu^+\nu X$ composition did not change (Table 3.4). These relative branching fractions are mostly well-known, at least for the most common decays, but will be separated in the fit in different categories.

The inclusive sample of $D^{*-} \to \overline{D}^0(\to K^+\pi^-)\pi^-$ decays contains 9184 events after the stripping and 1018 reconstructed modes after the full selection. The detailed composition can be found in Table 4.4. Most of the sample (88%) corresponds to the $B^0 \to D^{*-}(\to \overline{D}^0(\to K^+\pi^-)\pi^-)\mu^+\nu X$ sample, which can further be separated in 95.2% of $B^0 \to D^{*-}\mu^+\nu$, 4.0% of $B^0 \to D^{**-}(\to D^{*-}X)\mu^+\nu$ modes with a higher resonance and 0.8% of semitauonic $B^0 \to D^{*-}\tau^+(\to \mu^+\nu\nu)\nu$ modes. The main background found in the inclusive sample is made of $B^+ \to D^{*-}\mu^+X$ decays, and some $B_s^0 \to D^{*-}\mu^+X$ following the same topology. As the main difference between these two decays is the mass of the B meson and that the corrected B mass distribution is mainly driven by the number of missing particles in the decay, we can use a single mass distribution for both modes. $B \to D^*D$ modes cannot be fully suppressed, but have an expected fraction below 2%. It was seen in Sect. 3.4.1 that this component has the same corrected mass spectrum as the semitauonic $B^0 \to D^{*-}\tau^+(\mu^+\nu\nu)\nu$ and can thus be modelled as such. Finally, some misidentified decays where the muon is misidentified as a kaon represents less than 1% of the inclusive sample. This component will be included with the signal, but will not have a large impact on the $\Delta(D)'$ result, as it includes a real D^0.

4.3.2   Fit of sample composition

A binned least-squares fit to the corrected B mass distribution is performed, following the method described in Section 3.4. Figure 4.5 shows the mass shapes for all components used in

Process	$\mathcal{B}$ [%]	Decay model
$B^0 \to D^{*-}\mu^+\nu$	5.01	HQET2 1.20 0.908 1.426 0.818 †
$B^0 \to D_1^-(\to D^{*-}X)\mu^+\nu$	0.1749	ISGW2
$B^0 \to D_2^{*-}(\to D^{*-}X)\mu^+\nu$	0.0620	ISGW2
$B^0 \to D_0^{*-}(\to D^{*-}X)\mu^+\nu$	0.0564	ISGW2
$B^0 \to D^{*-}\pi^+\pi^-\mu^+\nu$	0.2451	PHSP
$B^0 \to D_1^{\prime-}(\to D^{*-}X)\mu^+\nu$	0.0650	ISGW2
$B^0 \to D^{*-}\pi^0\pi^0\mu^+\nu$	0.2451	PHSP
$B^0 \to D^{*-}\pi^0\mu^+\nu$	0.0462	GOITY_ROBERTS
$B^0 \to D^{*-}\tau^+(\to \mu^+\nu\nu)\nu$	0.2604	ISGW2
$B^0 \to D_2^{*-}(\to D^{*-}X)\tau^+(\to \mu^+\nu\nu)\nu$	0.0041	ISGW2
$B^0 \to D_1^-(\to D^{*-}X)\tau^+(\to \mu^+\nu\nu)\nu$	0.0082	ISGW2
$B^0 \to D_0^{*-}(\to D^{*-}X)\tau^+(\to \mu^+\nu\nu)\nu$	0.0027	ISGW2
$B^0 \to D_1^{\prime-}(\to D^{*-}X)\tau^+(\to \mu^+\nu\nu)\nu$	0.0056	ISGW2

Table 4.3 – Processes contributing to the simulated sample of inclusive $B^0 \to D^{*-}(\to \overline{D}^0(\to K^+\pi^-)\pi^-)\mu^+\nu X$ decays. Branching fractions and decay models used in generation are also reported.
†Because of a bug in generation, different HQET(2) parameters have been used, but the sample has been reweighing accordingly.

Decay mode	Candidates after selection	Fraction [%]
$B^0 \to D^{*-}\mu^+X$	896	88.0
$B^+ \to D^{*-}\mu^+X$	83	8.2
$B_s^0 \to D^{*-}\mu^+X$	15	1.5
$B \to D^{*-}D(\to \mu X)$	17	1.7
$B \to D^{*-}K^+X$	7	0.7

Table 4.4 – Composition of the inclusive $D^{*-} \to \overline{D}^0(\to K^+\pi^-)\pi^-$ sample after the full selection.

the fit. Most of them can be separated, except for the $B^0 \to D^{(*)-}\mu^+\nu X$ and $B^+ \to D^{(*)-}\mu^+\nu X$ decays (as well as potential $B_s^0 \to D^{(*)-}\mu^+\nu X$ decays), which all have a similar distribution reflecting their similar topology. A single template is used by summing the templates of these two components, weighted according to their expected relative yield in simulation; a single yield is thus associated to this combined template.

Figure 4.6 shows the fit projections on top of the corrected B mass distributions for the D^0 and D^- samples. Fit results are reported in Table 4.5. The correlation matrices are reported in Appendix A.1. The D^- fit is very similar to the fit of Figure 3.10, but has a better χ^2/ndf of 84.4/88 (probability 59.0%) and a slightly lower combinatorics component thanks to the refined selection. However, the D^0 fit is bad with a χ^2/ndf of 166.5/91 (probability 2.4×10^{-6}) and the shape of the residuals indicates that the corrected B mass of the signal component is probably not modelled properly. Compared to the fractions expected from the inclusive sample, the signal fraction is slightly high, while the $B^0/B^+ \to D^{(*)-}\mu^+\nu X$ component is
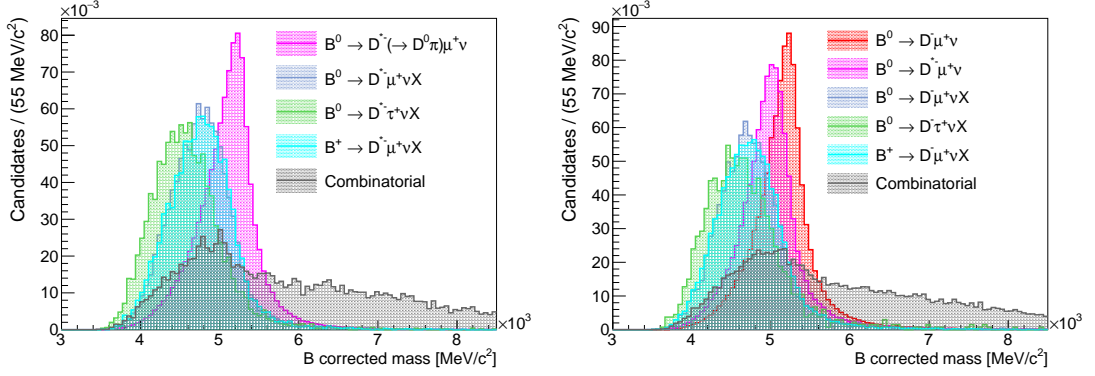
Figure 4.5 – Corrected B mass distributions of the components considered in the (left) $B^0 \to D^{*-}(\to \overline{D}^0(\to K^+\pi^-)\pi^-)\mu^+\nu X$ and (right) $B^0 \to D^-(\to K^+\pi^-\pi^-)\mu^+\nu X$ fits.

Component	D^0 fraction [%]	D^- fraction [%]
$B^0 \to D^-\mu^+\nu$	–	49.83 ± 0.51
$B^0 \to D^{*-}\mu^+\nu$	88.47 ± 0.22	32.02 ± 0.87
$B^0/B^+ \to D^{(*)-}\mu^+\nu X$	9.36 ± 0.43	15.26 ± 1.07
$B^0 \to D^{(*)-}\tau^+\nu X$	1.96 ± 0.27	0.67 ± 0.66
Combinatorial	0.21 ± 0.04	2.21 ± 0.09

Table 4.5 – Results of the fit to the corrected B mass distribution of the D^0 and D^- samples.

slightly low (about 3%); this might also be due to some mismodelling of the corrected mass shapes. However, as all of these decay modes have a real D^0, the effect of this mismodelling is small and will be taken into account in the systematics section.

4.4 Determination of $\Delta(D)'$

The difference between the decay widths of the D^0 and D^- mesons, $\Delta(D)'$, is measured through a fit to the ratio of D^0 to D^- signal yields as a function of the D meson decay time, t_D. The procedure is almost identical to that described in Section 3.5. A mass fit is performed in each decay-time bin and the ratio of these yields is fitted to determine $\Delta(D)'$. The effects of decay-time acceptance and resolution are studied with simulation samples and included when necessary.

4.4.1 Signal yields as function of decay time

The data sample is split into 20 subsamples according to the D meson decay time, such that the amount of D^- (D^0) events is large enough at low (high) decay times. The fits use a simple model with three components: the signal, all the physics backgrounds and the combinatorial background. Mass templates are added together with the fractions obtained from the time-integrated mass fit. The usual fit of Sect. 3.5.1 is performed and the D^0 and D^- yields are extracted in each decay-time bin. The detailed results are reported in Appendix A.4.
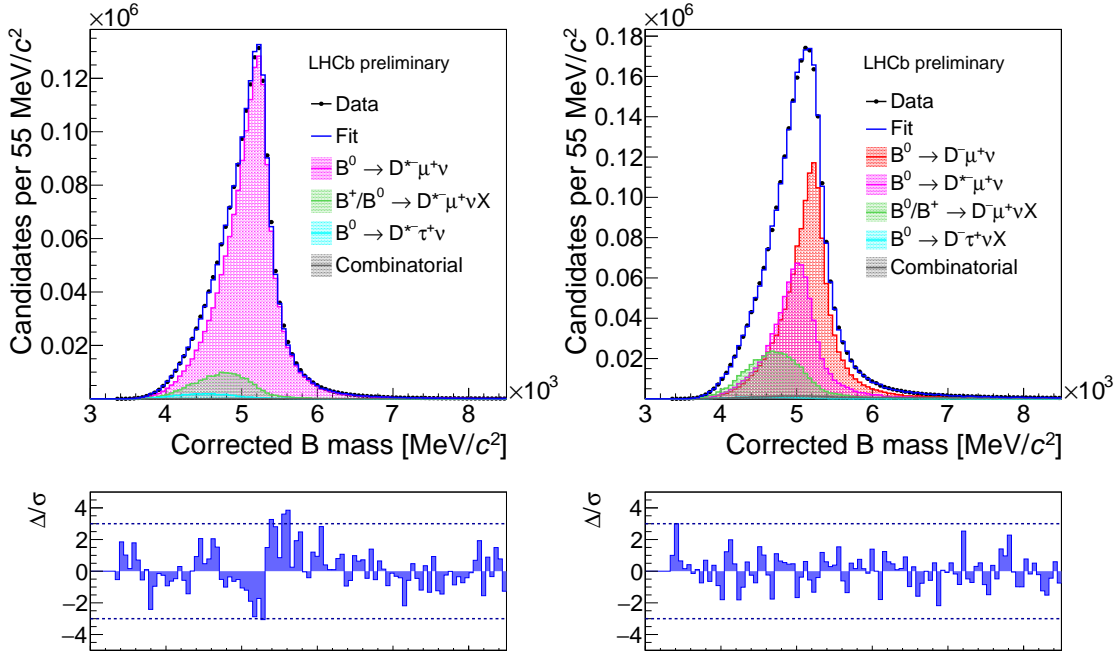
Figure 4.6 – Corrected B mass distributions of the (left) $B^0 \to D^{*-}(\to \overline{D}^0(\to K^+\pi^-)\pi^-)\mu^+\nu X$ and (right) $B^0 \to D^-(\to K^+\pi^-\pi^-)\mu^+\nu X$ samples with fit projections overlaid.

4.4.2 Relative time-acceptance correction

As the selection criteria have been chosen to reduce backgrounds and differences between the signal and reference decays, the decay-time acceptances for D^0 and D^- decays are almost identical, despite the fact that the $B^0 \to D^-(\to K^+\pi^-\pi^-)\mu^+\nu X$ signal is composed of two different decay channels ($B^0 \to D^-\mu^+\nu$ and $B^0 \to D^{*-}\mu^+\nu$), while the $B^0 \to D^{*-}(\to \overline{D}^0(\to K^+\pi^-)\pi^-)\mu^+\nu X$ signal contains only one. Figure 4.7 shows the ratio of the acceptances, as determined from simulation, with relative fractions between the two signal components measured in the mass fit for the D^- sample. A fit with a linear function $a + bt_D$ gives $a = 1.0008 \pm 0.0047$ and $b = -0.0009 \pm 0.0050$ ps^{-1} with $\chi^2/$ndf = 24.7/18 (probability of 13.3%); a fit with a constant gives $\chi^2/$ndf = 24.7/19 (probability of 17.0%). As the slope of the linear function is compatible with zero and there is no gain from using a linear ratio over a constant ratio, the ratio of time-acceptances can be neglected in the lifetime fit. Residual differences will be taken into account as systematic uncertainties.

4.4.3 Lifetime fit

The same binned least-squares fit explained in Sec. 3.5.3 is used to measure $\Delta(D)'$. In the denominator of the χ^2 of Eq.(3.9), Γ_d is fixed to the known value of the D^- lifetime, $\tau(D^-) = 1.040 \pm 0.007$ ps [19], while the width of the numerator, Γ_n, is written as $\Gamma_d + \Delta(D)'$ with $\Delta(D)'$ determined by the fit. The ratio of time acceptances is not included in the fit.

The decay-time resolution of both samples also enters in the pdf translating the time-evolution
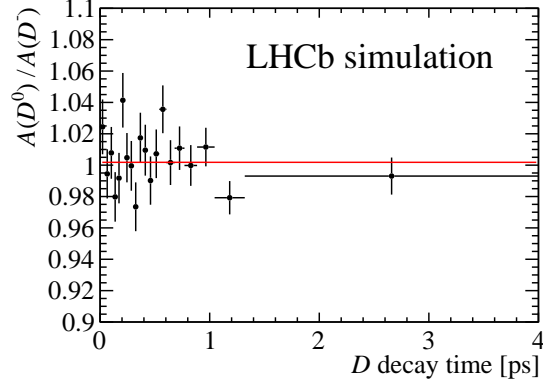
Figure 4.7 – Ratio of acceptances as a function of D decay time for D^0 over D^- in simulation.
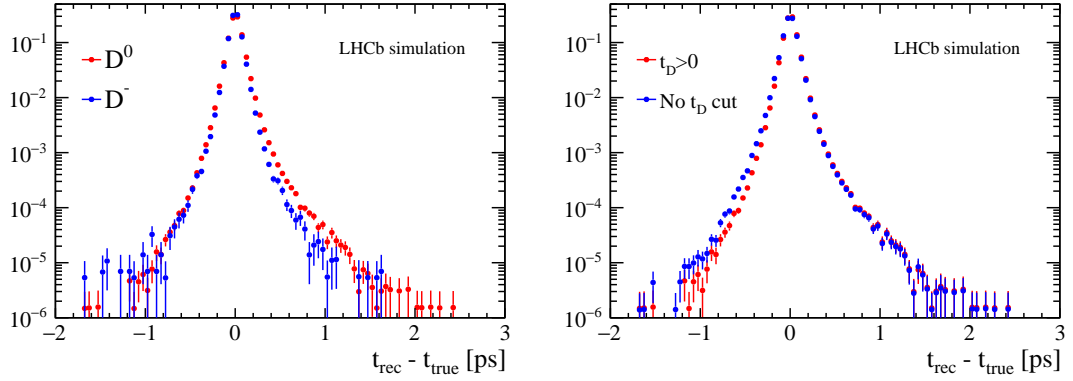
Figure 4.8 – Distributions of the difference between reconstructed and true D decay times for (left) the (red) D^0 and (blue) D^- samples after the full selection (right) the D^0 sample with (red) and without (blue) the $t_D > 0$ criteria applied (all other criteria are fulfilled). The distributions on the left are used to describe the D-decay-time resolution in the fit.

of the D mesons, see Eq. (3.11). In the lifetime fit, the decay-time resolution is represented by two separate histograms for D^0 and D^-, modelled from simulation, as shown in Figure 4.8 (left).

The distributions of the differences between reconstructed and true decay time have an RMS of 90 fs and 76 fs for the D^0 and D^- samples, respectively. This difference can be explained as the D^0 is built from only two tracks, while the D^-, reconstructed from three tracks, has a better-defined decay vertex. The D^0 distribution also shows an asymmetry with a longer tail for positive values of the decay-time difference. Figure 4.8 (right) shows that this asymmetry almost completely disappears if candidates with negative reconstructed decay time are added. Any remaining asymmetry on both D^0 and D^- distributions can be explained by the stripping criteria, $v_z(D) - v_z(B) > -2.5 \ (-1.0)$ mm (Tab. 4.1), which removes candidates being assigned a too negative decay time. This effect is less visible in the D^- sample, as the fraction of real signal decays with a negative reconstructed decay time is much lower (0.5% with respect to the events with $t_D > 0$; 7% for the D^0 sample). Uncertainties on these distributions are taken into account in the systematic studies.
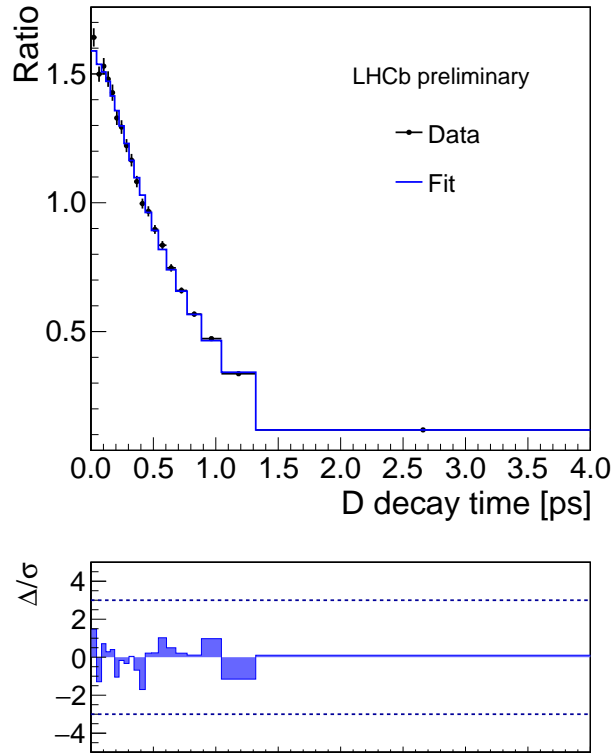
Figure 4.9 – Acceptance-corrected signal-yield ratio of D^0 over D^- as a function of D decay time with fit projection overlaid.

4.4.4   Results

The fit to the ratio of the D^0 and D^- signal yields in bins of D decay time yields

$$\Delta(D)' = 1.4644 \pm 0.0085\,\text{ps}^{-1}. \tag{4.3}$$

Figure 4.9 shows the yield-ratio distribution after acceptance correction with results of the time-fit overlaid. The fit quality is good, with $\chi^2/\text{ndf} = 12.8/18$ (probability 80%). After discussing systematic uncertainties, we determine the value of the D^0 lifetime in Section 4.6.

4.5   Systematic uncertainties and checks

Systematic uncertainty on $\Delta(D)'$ are computed as the absolute value of the difference between the $\Delta(D)'$ value obtained in the nominal analysis and the value obtained after modulating the parameters of the sources of systematic errors. We assess systematic uncertainties accounting for the following classes of effects: (i) size of the simulated samples; (ii) uncertainties associated with the decay-time acceptance; (iii) uncertainties associated with the decay-time resolution; (iv) mismodellings in the corrected B mass fits. Source (iv) impacts the determination of the sample composition and requires to go through all subsequent steps of the analysis, while only the time fit needs to be redone for sources (ii) and (iii). The systematic uncertainties

considered are listed in Tab. 4.6 and detailed in the following. The total systematic uncertainty is their sum in quadrature.

	$\sigma[\Delta(D)'] \, [\mathrm{ps}^{-1}]$
Simulated sample size (mass fit)	0.0074
Mass fit mismodellings	0.0021
Decay-time acceptance	0.0073
Decay-time resolution	0.0078
Total systematic	0.0132
Statistical	0.0043

Table 4.6 – Summary of the systematic and statistical uncertainties.

4.5.1   Size of simulation samples

The simulation samples used in this analysis are small compared to the data: about one third for the D^0 signal and less than a tenth for the D^- signal sample. This implies that a large part of the uncertainty computed in Sect. 4.4.4 is actually due to the statistics of the simulation samples. In order to separate these effects, we forbid any possible statistical oscillation of the mass templates in the time-integrated and time-dependent mass fits. The statistical error becomes $0.0043 \, \mathrm{ps}^{-1}$ instead of $0.0085 \, \mathrm{ps}^{-1}$. The systematic uncertainty due to the size of the simulated sample is equal to the difference in quadrature, $0.0074 \, \mathrm{ps}^{-1}$. This also decreases the statistical uncertainty on $\tau(D^0)$. Notice that we consider this uncertainty as a systematic one for this measurement, as it is particularly large, unlike the corresponding ones in the B_s^0 and D_s^- lifetime measurements, which are included in the statistical uncertainty.

4.5.2   Mass fit models

The model of the corrected B mass fit is supposed to be well-represented by simulation, as the form factors of the $B^0 \to D^{*-}\mu^+\nu$ decays are well-known. However, the mass fit of the D^0 sample in Sect. 4.3.2 is not satisfactory. This is most likely due to a non-perfect correction of a bug in generation, where decays were originally produced with the wrong form factors (see Table 4.3). As a simple correction, we build a mass model by simply shifting the $B^0 \to D^{*-}\mu^+\nu$ model by a few MeV/c^2. The fit is found to be optimal for a mass shift of +4 or +6 MeV/c^2, for which the fit probability reaches 2% instead of 2.4×10^{-6} for the default fit. This reduces the signal fraction by about 1%, but the time-dependence does not suffer much from this difference, leading to a corresponding systematic uncertainty of $0.0020 \, \mathrm{ps}^{-1}$.

The mass templates of $B^0 \to D^{(*)-}\mu^+\nu X$ and $B^+ \to D^{(*)-}\mu^+\nu X$ are merged together according to the fractions from the inclusive sample. As this sample is small, these relative fractions are not set precisely and we therefore allow for large variations of the order of 30%, modelling therefore uncertainties on the mass models of the physics backgrounds. A systematic uncertainty of $0.0005 \, \mathrm{ps}^{-1}$ is found.

The systematic uncertainty due to the mass fit models is the sum in quadrature of these two effects, leading to 0.0021 ps^{-1}.

4.5.3 Decay-time acceptance and resolution

The measurement of $\Delta(D)'$ aims to equalise the acceptances of the two decays with a very similar selection. The ratio is shown to be uniform as a function of decay time in simulation, but because of the low statistics of the simulation samples, this is not satisfactory to show how flat the ratio is. By adding the histogram of the ratio in the fit, the result changes slightly, leading to a small uncertainty of 0.0013 ps^{-1}. If the uncertainties on the ratio of the time-acceptances for each bin are added, the uncertainty on $\Delta(D)'$ goes from 0.0085 ps^{-1} to 0.0112 ps^{-1}, leading to an extra systematic uncertainty of 0.0073 ps^{-1}. This last uncertainty however also depends on the size of the simulation sample and can therefore easily be decreased with larger sets of simulated data.

As the decay-time resolution is larger than the width of some decay-time bins and is significantly different between the two samples, the result may be rather sensitive to small changes of these resolutions. As in Sect. 3.8.5, we evaluate the difference in a case where the resolution is scaled by a factor of 1.1 with respect to the default value. This leads to a systematic uncertainty of 0.0078 ps^{-1}.

4.6 Summary and outlook

We report on the feasibility of a measurement of the difference between the decay widths of the D^0 and D^- mesons, $\Delta(D)'$, using semileptonic $B^0 \to D^{*-}(\to \overline{D}^0(\to K^+\pi^-)\pi^-)\mu^+\nu X$ and $B^0 \to D^-(\to K^+\pi^-\pi^-)\mu^+\nu X$ decays partially reconstructed in the full data set collected in Run I by LHCb at $\sqrt{s} = 7$ and 8 TeV and corresponding to an integrated luminosity of 3 fb^{-1}. The result is found to be

$$\Delta(D)' = 1.4644 \pm 0.0043\,(\text{stat}) \pm 0.0132\,(\text{syst})\,\text{ps}^{-1}, \tag{4.4}$$

where most of the systematic uncertainties are due to the size of simulation samples and uncertainties on the decay-time resolutions. Using the world's average values of the D^0 and D^- lifetimes as input [19], a determination of $\Delta(D)'$ can be computed and is equal to $\Delta(D)'_{PDG} = 1.4769 \pm 0.0110\,\text{ps}^{-1}$, which is more precise than and compatible with our measurement. By using only the value of the D^- lifetime as input, the D^0 lifetime is determined to be

$$\tau(D^0) = 0.4122 \pm 0.0007\,(\text{stat}) \pm 0.0022\,(\text{syst}) \pm 0.0011\,(\tau_{D^-})\,\text{ps}, \tag{4.5}$$

where the last uncertainty is due to the uncertainty on the D^- lifetime. This result is compatible with the 15-years-old measurement by FOCUS [83], $0.4096 \pm 0.0011\,(\text{stat}) \pm 0.0015\,(\text{syst})$, and with the world's average value, $0.4101 \pm 0.0015\,\text{ps}$ [19].

An interesting result for cross-checking HQE predictions comes from the ratio of the D^- over

the D^0 lifetimes. We can write this ratio as

$$r = \frac{\tau(D^-)}{\tau(D^0)} = \frac{\Gamma(D^0)}{\Gamma(D^-)} = 1 + \frac{\Delta(D')}{\Gamma(D^-)} = 1 + \Delta(D')\tau(D^-). \tag{4.6}$$

By using the world's average values for the two lifetimes as input, the ratio is found to be $r_{PDG} = 2.5360 \pm 0.0194$ and is already known at the sub-percent level. However, this ratio can be measured more efficiently by using $\Delta(D')$ and $\tau(D^-)$ as inputs. With our result, we find $r = 2.5230 \pm 0.0177$, which is more precise than r_{PDG}.

With the data and sample statistics used in this analysis, a competitive measurement of $\Delta(D)'$ is not possible, while the measurement of the D^0 lifetime would anyway be limited by an external input. However, a measurement could be done with full Run II data, as an additional integrated luminosity of 5 fb^{-1} is expected to be recorded by the end of 2018. Furthermore, as these events are collected at a higher centre-of-mass energy, $\sqrt{s} = 13$ TeV, the cross-sections of the signal and reference decays are higher, resulting in larger data sets. The ratio of b-quark production cross-sections for 13 TeV over 7 TeV data was found to be $2.00 \pm 0.02 \pm 0.26$ [84] and so we can roughly expect twice more events per fb^{-1} in Run II. We consider thereafter Run II data only and not Run I + Run II. This amount of data would reduce the statistical uncertainty on $\Delta(D)'$ from 0.0043 ps^{-1} to 0.0023 ps^{-1}, considering the same selection efficiency as in this analysis.

Most importantly, the systematic uncertainties could be decreased by producing larger simulation samples. With simulation samples of the same size as the expected Run II data samples for both signal, reference and backgrounds channels in addition to the Run II data samples, the systematic uncertainty due to the simulated sample size for the mass fit would go from 0.0074 ps^{-1} to 0.0017 ps^{-1}, while the uncertainty on the ratio of the acceptances due to the samples statistics would decrease from 0.0073 ps^{-1} to 0.0018 ps^{-1}. The total systematic uncertainty of 0.0085 ps^{-1} would then be dominated by decay-time resolution uncertainties, which would be the next challenge to overcome. With these statistical and systematic uncertainties, the $\Delta(D)'$ result would be more precise than the estimation computed above. The uncertainty on the ratio r would fall from 0.0177 to 0.0137, paving the way for a measurement of r with a relative uncertainty of only 0.5%.

To conclude, this Run II scenario is being very optimistic, as it does not consider other challenges accompanying the additional statistics: creation of a new selection, need of more polished mass fits with possible additional small components which could be neglected here, challenge to get another flat ratio of time-acceptances, etc. A competitive D^0 lifetime would in this optimal case be possible, as the total uncertainty of $\tau(D^0)$ would be 0.0018 ps, to be compared with the average's value of 0.4101 ± 0.0015 ps. An optimisation of the time-resolution systematic uncertainty could therefore lead to a world-leading measurement of $\tau(D^0)$.

5 Conclusion

This thesis explores measurements of heavy-flavoured meson lifetimes in semimuonic B^0 and B_s^0 decays at the LHCb experiment. Unlike the other detectors at the LHC, LHCb was specifically built to perform precise measurements with heavy-hadron decays, by optimising on the pseudorapidity region for studying b and c hadrons. The thesis also presents a part of the research and development done on Silicon Photomultipliers for the new Scintillating Fibre Tracker, which will be installed in 2019 as a part of the LHCb Upgrade.

Lifetimes measurements are interesting as they allow to put constraints on parameters of effective QCD models, which would allow precise description of weak decays of hadrons. This is essential in the search for 'New Physics' by comparing experimental data with Standard Model predictions. In the method designed for this research, we determine lifetimes by measuring the differences between the decay widths of two mesons from semileptonic decay channels, partially reconstructed with the same final states. This allows to cancel systematic uncertainties when considering the ratios of time-dependent distributions between the signal and reference decays. The measurements are performed using proton-proton collisions at centre-of-mass energies of 7 and 8 TeV, collected in 2011 and 2012 by the LHCb experiment and corresponding to 3.0 fb^{-1} of integrated luminosity.

First, the difference between the decay widths of the B_s^0 and B^0 mesons, $\Delta(B)$, is computed by considering semileptonic $B_s^0 \to D_s^{(*)-}\mu^+\nu_\mu$ and $B^0 \to D^{(*)-}\mu^+\nu_\mu$ decays. Approximately 410 000 and 110 000 of such signal decays are partially reconstructed in the $K^+K^-\pi^-\mu^+$ final state. The result is found to be

$$\Delta(B) = -0.0115 \pm 0.0053\,(\text{stat}) \pm 0.0041\,(\text{syst})\,\text{ps}^{-1}. \tag{5.1}$$

Using the same decays, we also measure the width difference between the D_s^- and D^- mesons,

$$\Delta(D) = 1.0131 \pm 0.0117\,(\text{stat}) \pm 0.0065\,(\text{syst})\,\text{ps}^{-1}. \tag{5.2}$$

Applying the known B^0 and D^- lifetimes [19], we obtain a measurement of the flavour-specific

lifetime of the B_s^0 meson,

$$\tau_s^{\text{fs}} = 1.547 \pm 0.013\,(\text{stat}) \pm 0.010\,(\text{syst}) \pm 0.004\,(\tau_{B^0})\,\text{ps}, \tag{5.3}$$

and of the D_s^- lifetime,

$$\tau_{D_s^-} = 0.5064 \pm 0.0030\,(\text{stat}) \pm 0.0017\,(\text{syst}) \pm 0.0017\,(\tau_{D^-})\,\text{ps}, \tag{5.4}$$

where the last uncertainties are due to the limited knowledge of the B^0 and D^- lifetimes, respectively. The τ_s^{fs} result is consistent with, and more precise than, the previous most precise determinations and is consistent with the current world's average value, $1.516 \pm 0.014\,\text{ps}$ [19]. The determination of $\tau_{D_s^-}$ is consistent with, and more precise than, the world's best determination, $0.5074 \pm 0.0055\,(\text{stat}) \pm 0.0051\,(\text{syst})\,\text{ps}$ from the FOCUS collaboration [82], and the 2017 world's average value, $0.500 \pm 0.007\,\text{ps}$ [19].

The feasibility of a D^0 lifetime measurement is studied, by following the same method and measuring the difference between the decay widths of the D^0 and D^- mesons, $\Delta(D)'$. We consider the semileptonic $B^0 \to D^{(*)-}\mu^+\nu_\mu$ decays, with approximately 2.2×10^6 signal $D^{*-} \to \overline{D}^0(\to K^+\pi^-)\pi^-$ and 1.6×10^6 reference $D^{(*)-} \to K^+\pi^-\pi^-(X)$ decays. The final result is

$$\Delta(D)' = 1.4644 \pm 0.0043\,(\text{stat}) \pm 0.0132\,(\text{syst})\,\text{ps}^{-1}. \tag{5.5}$$

Using the D^- lifetime as input, we get an estimate of the D^0 lifetime,

$$\tau_{D^0} = 0.4122 \pm 0.0007\,(\text{stat}) \pm 0.0022\,(\text{syst}) \pm 0.0011\,(\tau_{D^-})\,\text{ps}. \tag{5.6}$$

This result is less precise than the world's average of $0.4101 \pm 0.0015\,\text{ps}$ and is dominated by the systematic error. This can be improved by increasing the statistics for the number of simulated events in the future. With Run II data, the systematic error on $\Delta(D)'$ could be reduced to $0.0085\,\text{ps}^{-1}$, and for the D^0 lifetime to 0.0014 ps.

All results are compatible with the SM predictions, and do not indicate evidence for 'New Physics' at the current level of precision.

A Appendix

A.1 Correlation matrices

We report here the correlation matrices of the fits of Sec. 3.4 and 4.3.2.

	f_0	f_1	f_2	f_3	f_4
f_0	1	−0.8869	0.5690	−0.3230	−0.2091
f_1		1	−0.8459	0.5743	0.01174
f_2			1	−0.8624	−0.06785
f_3				1	−0.03203
f_4					1

Table A.1 – Correlation matrix of the fit of the B_s^0 sample of Sect. 3.4. The free parameters of the fit are the fraction of the components: $f_0 = f(B_s^0 \to D_s^- \mu^+ \nu)$, $f_1 = f(B_s^0 \to D_s^{*-} \mu^+ \nu)$, $f_2 = f(\text{phys. bkg. 1})$, $f_3 = f(\text{phys. bkg 2})$, and $f_4 = 1 - \sum_{i=0}^{3} f_i = f(\text{combinatorial})$.

	f_0	f_1	f_2	f_3
f_0	1	−0.8404	0.4421	−0.3252
f_1		1	−0.7505	−0.0070
f_2			1	−0.2269
f_3				1

Table A.2 – Correlation matrix of the fit of the B^0 ($K^+ K^- \pi^-$) sample of Sect. 3.4. The free parameters of the fit are the fraction of the components: $f_0 = f(B^0 \to D^- \mu^+ \nu)$, $f_1 = f(B^0 \to D^{*-} \mu^+ \nu)$, $f_2 = f(B^0/B^+ \to D^- \mu^+ \nu X)$, and $f_3 = 1 - \sum_{i=0}^{2} f_i = f(\text{combinatorial})$.

	f_0	f_1	f_2	f_3	f_4
f_0	1	−0.8508	0.3986	−0.2914	−0.0465
f_1		1	−0.7648	0.6026	−0.1217
f_2			1	−0.9520	0.1901
f_3				1	−0.2116
f_4					1

Table A.3 – Correlation matrix of the fit of the B^0 ($K^+\pi^-\pi^-$) sample of Sect. 3.4. The free parameters of the fit are the fraction of the components: $f_0 = f(B^0 \to D^-\mu^+\nu)$, $f_1 = f(B^0 \to D^{*-}\mu^+\nu)$, $f_2 = f(B^0/B^+ \to D^-\mu^+\nu X)$, $f_2 = f(B^0 \to D^-\tau^+\nu X)$, and $f_4 = 1 - \sum_{i=0}^{3} f_i = f$(combinatorial).

	f_0	f_1	f_2	f_3
f_0	1	−0.8421	0.5375	−0.2256
f_1		1	−0.8999	0.0866
f_2			1	−0.1088
f_3				1

Table A.4 – Correlation matrix of the fit of the D^0 sample of Sect. 4.3.2. The free parameters of the fit are the fraction of the components: $f_0 = f(B^0 \to D^{*-}\mu^+\nu)$, $f_1 = f(B^0/B^+ \to D^{*-}\mu^+\nu X)$, $f_2 = f(B^0 \to D^{*-}\tau^+\nu X)$, and $f_3 = 1 - \sum_{i=0}^{2} f_i = f$(combinatorial).

	f_0	f_1	f_2	f_3	f_4
f_0	1	−0.8521	0.4023	−0.2902	−0.0459
f_1		1	−0.7714	0.6104	−0.1730
f_2			1	−0.9498	0.2667
f_3				1	−0.3065
f_4					1

Table A.5 – Correlation matrix of the fit of the D^- sample of Sect. 4.3.2. The free parameters of the fit are the fraction of the components: $f_0 = f(B^0 \to D^-\mu^+\nu)$, $f_1 = f(B^0 \to D^{*-}\mu^+\nu)$, $f_2 = f(B^0/B^+ \to D^-\mu^+\nu X)$, $f_2 = f(B^0 \to D^-\tau^+\nu X)$, and $f_4 = 1 - \sum_{i=0}^{3} f_i = f$(combinatorial).

A.2 Mass fit in bins of decay time for the $\Delta(D, B)$ measurement

Details of the mass fits in bins of the decay time of Sec. 3.6.3 and 3.6.5 are presented here.

For the $\Delta(B)$ measurement, the yields in bins of the B corrected decay time of each component are reported in a Tabs. A.6, A.7 and A.8 for the B_s^0, B^0 ($K^+K^-\pi^-$), and B^0 ($K^+\pi^-\pi^-$) samples, respectively. The fit projections are shown in Figs. A.1–A.6. Figure A.7 shows the decay-time distributions of the components of the B_s^0 and B^0 samples as found from these mass fits. The distributions for the B^0 signal and physics background are consistent with those expected from simulation, yielding χ^2/bins of 17.2/20 (probability 64%) and 26.7/20 (probability 14%), respectively.

For the $\Delta(D)$ measurement, the yields in bins of the D decay time of each component are reported in a Tabs. A.9, A.10 and A.11 for the B_s^0, B^0 ($K^+K^-\pi^-$), and B^0 ($K^+\pi^-\pi^-$) samples, respectively. The fit projections are shown in Figs. A.8–A.13. Figure A.14 shows the decay-time distributions of the components of the B_s^0 and B^0 samples determined by these fits. The distributions for the B^0 signal and physics background are consistent with those expected from simulation, yielding χ^2/bins of 33.6/20 (probability 3%) and 21.6/20 (probability 36%), respectively.

Time [ps]	Signal	Physics bkg	Combinatorial
0.00-0.47	45978 ± 1959	6774 ± 1516	15162 ± 929
0.47-0.63	46234 ± 1247	4275 ± 956	6746 ± 608
0.63-0.76	41465 ± 965	4481 ± 764	3567 ± 411
0.76-0.89	42974 ± 971	4613 ± 752	3851 ± 450
0.89-1.02	44146 ± 954	4292 ± 730	3355 ± 461
1.02-1.15	43642 ± 905	4044 ± 722	2662 ± 408
1.15-1.28	42343 ± 771	4166 ± 577	2310 ± 389
1.28-1.42	44104 ± 792	4538 ± 586	2476 ± 390
1.42-1.57	44723 ± 742	4099 ± 549	2179 ± 375
1.57-1.73	44744 ± 761	3599 ± 506	2341 ± 499
1.73-1.90	45023 ± 829	3041 ± 570	2658 ± 548
1.90-2.09	44358 ± 729	3865 ± 527	1552 ± 406
2.09-2.30	44452 ± 668	4100 ± 486	911 ± 315
2.30-2.54	41821 ± 1189	4249 ± 591	3180 ± 1235
2.54-2.82	44040 ± 736	4219 ± 514	1271 ± 486
2.82-3.16	44460 ± 759	3193 ± 497	1016 ± 674
3.16-3.60	44662 ± 803	3648 ± 517	1644 ± 806
3.60-4.21	42054 ± 1048	2944 ± 589	3451 ± 1295
4.21-5.25	42877 ± 724	3973 ± 493	1583 ± 680
5.25-12.00	43863 ± 843	3752 ± 473	1362 ± 865

Table A.6 – Yields (weighted) of the components of the B_s^0 mass fit in bins of corrected decay time.

Time [ps]	Signal	Physics bkg	Combinatorial
0.00-0.47	6157 ± 343	1057 ± 280	2153 ± 142
0.47-0.63	5477 ± 221	1408 ± 185	905 ± 93
0.63-0.76	5304 ± 176	966 ± 147	655 ± 70
0.76-0.89	5447 ± 162	1070 ± 133	555 ± 67
0.89-1.02	5572 ± 153	950 ± 125	513 ± 66
1.02-1.15	5453 ± 149	932 ± 114	514 ± 71
1.15-1.28	5413 ± 142	826 ± 108	427 ± 71
1.28-1.42	5607 ± 139	846 ± 106	424 ± 76
1.42-1.57	5637 ± 142	1082 ± 106	379 ± 79
1.57-1.73	5610 ± 149	960 ± 105	420 ± 107
1.73-1.90	5345 ± 142	1080 ± 105	415 ± 93
1.90-2.09	5506 ± 140	1031 ± 108	478 ± 122
2.09-2.30	5604 ± 145	884 ± 101	417 ± 107
2.30-2.54	5347 ± 150	846 ± 107	526 ± 150
2.54-2.82	5517 ± 150	940 ± 106	386 ± 133
2.82-3.16	5285 ± 158	1001 ± 116	423 ± 182
3.16-3.60	5400 ± 146	930 ± 123	521 ± 177
3.60-4.21	5433 ± 170	943 ± 104	336 ± 192
4.21-5.25	5036 ± 157	1031 ± 108	496 ± 180
5.25-12.00	5215 ± 128	1178 ± 92	101 ± 108

Table A.7 – Yields of the components of the B^0 ($K^+ K^- \pi^-$) mass fit in bins of corrected decay time.

Time [ps]	Signal	Physics bkg	Combinatorial
0.00-0.47	138192 ± 4578	27945 ± 4212	29056 ± 1200
0.47-0.63	131473 ± 2951	26082 ± 2877	6672 ± 461
0.63-0.76	118452 ± 2320	19859 ± 2264	3455 ± 316
0.76-0.89	119580 ± 1985	21195 ± 1929	2949 ± 323
0.89-1.02	112507 ± 1994	25790 ± 1941	1895 ± 264
1.02-1.15	108762 ± 1797	24030 ± 1748	1277 ± 251
1.15-1.28	105365 ± 1748	21331 ± 1719	1215 ± 176
1.28-1.42	103790 ± 1767	24566 ± 1726	633 ± 287
1.42-1.57	107240 ± 1553	20046 ± 1517	1412 ± 194
1.57-1.73	102487 ± 1442	22447 ± 1419	916 ± 262
1.73-1.90	98966 ± 1451	22993 ± 1405	396 ± 276
1.90-2.09	97690 ± 1415	23036 ± 1383	1027 ± 215
2.09-2.30	96332 ± 1314	22488 ± 1286	992 ± 215
2.30-2.54	98574 ± 1306	20353 ± 1266	48 ± 422
2.54-2.82	95186 ± 1295	21605 ± 1243	641 ± 438
2.82-3.16	93960 ± 1331	21673 ± 1302	1461 ± 381
3.16-3.60	97102 ± 1318	19642 ± 1324	286 ± 632
3.60-4.21	94353 ± 1327	22501 ± 1565	-1880 ± 1386
4.21-5.25	91705 ± 1353	23372 ± 1412	-646 ± 1221
5.25-12.00	93343 ± 1321	21701 ± 1410	-181 ± 1042

Table A.8 – Yields of the components of the B^0 ($K^+ \pi^- \pi^-$) mass fit in bins of corrected decay time.

Time [ps]	Signal	Physics bkg	Combinatorial
0.10-0.14	30292 ± 323	2436 ± 228	1822 ± 257
0.14-0.20	33460 ± 325	2956 ± 237	1493 ± 231
0.20-0.24	30541 ± 324	3229 ± 229	1460 ± 236
0.24-0.30	31946 ± 313	2799 ± 223	1695 ± 207
0.30-0.35	29497 ± 297	2012 ± 205	1620 ± 191
0.35-0.41	26157 ± 292	1968 ± 198	1645 ± 182
0.41-0.47	25230 ± 298	1996 ± 205	1914 ± 198
0.47-0.54	24627 ± 292	2045 ± 200	1678 ± 189
0.54-0.60	23452 ± 278	2186 ± 200	1497 ± 156
0.60-0.68	21547 ± 264	1813 ± 188	1359 ± 140
0.68-0.76	19482 ± 255	1615 ± 170	1736 ± 167
0.76-0.84	18065 ± 237	1257 ± 170	1299 ± 123
0.84-0.94	16401 ± 223	1336 ± 156	1212 ± 121
0.94-1.04	14344 ± 210	1143 ± 150	1042 ± 113
1.04-1.16	13940 ± 198	1090 ± 146	897 ± 89
1.16-1.29	11307 ± 188	1029 ± 140	969 ± 94
1.29-1.44	9992 ± 172	505 ± 123	933 ± 89
1.44-1.63	9016 ± 174	651 ± 125	870 ± 91
1.63-1.95	8715 ± 174	870 ± 132	915 ± 86
1.95-4.00	9036 ± 173	729 ± 129	1185 ± 79

Table A.9 – Yields of the components of the B_s^0 mass fit in bins of D decay time.

Time [ps]	Signal	Physics bkg	Combinatorial
0.10-0.14	4506 ± 165	719 ± 118	919 ± 170
0.14-0.20	4776 ± 167	679 ± 138	1112 ± 192
0.20-0.24	4793 ± 178	569 ± 120	961 ± 196
0.24-0.30	5091 ± 160	765 ± 113	807 ± 153
0.30-0.35	4664 ± 173	853 ± 108	891 ± 163
0.35-0.41	4368 ± 159	955 ± 108	746 ± 138
0.41-0.47	4760 ± 164	752 ± 102	722 ± 135
0.47-0.54	4848 ± 162	768 ± 107	823 ± 137
0.54-0.60	5031 ± 149	899 ± 106	591 ± 118
0.60-0.68	4735 ± 140	1017 ± 107	577 ± 93
0.68-0.76	4601 ± 157	887 ± 104	731 ± 117
0.76-0.84	4664 ± 140	898 ± 105	566 ± 83
0.84-0.94	4802 ± 140	782 ± 95	499 ± 88
0.94-1.04	4456 ± 136	829 ± 99	551 ± 87
1.04-1.16	5044 ± 135	728 ± 101	508 ± 78
1.16-1.29	4551 ± 131	966 ± 98	414 ± 71
1.29-1.44	4911 ± 130	726 ± 95	406 ± 70
1.44-1.63	4897 ± 133	1015 ± 106	323 ± 55
1.63-1.95	6472 ± 151	1162 ± 119	460 ± 69
1.95-4.00	13882 ± 221	2850 ± 180	1056 ± 80

Table A.10 – Yields of the components of the B^0 $(K^+K^-\pi^-)$ mass fit in bins of D decay time.

Time [ps]	Signal	Physics bkg	Combinatorial
0.10-0.14	79099 ± 1383	19736 ± 1369	3122 ± 639
0.14-0.20	88158 ± 1572	21311 ± 1510	3199 ± 509
0.20-0.24	87249 ± 1464	20079 ± 1391	3221 ± 560
0.24-0.30	91924 ± 1594	21601 ± 1533	3663 ± 424
0.30-0.35	89676 ± 1521	19467 ± 1471	3428 ± 357
0.35-0.41	86340 ± 1433	18263 ± 1381	2668 ± 321
0.41-0.47	91505 ± 1450	17714 ± 1369	2681 ± 399
0.47-0.54	92911 ± 1494	18583 ± 1439	3225 ± 355
0.54-0.60	92856 ± 1565	20680 ± 1490	2872 ± 371
0.60-0.68	92402 ± 1567	21516 ± 1514	3041 ± 351
0.68-0.76	92236 ± 1543	20507 ± 1467	2965 ± 333
0.76-0.84	92067 ± 1551	18330 ± 1473	2866 ± 354
0.84-0.94	95082 ± 1573	17964 ± 1514	3572 ± 324
0.94-1.04	87605 ± 1651	21339 ± 1603	2522 ± 369
1.04-1.16	98576 ± 1599	18601 ± 1521	2814 ± 358
1.16-1.29	92143 ± 1580	19635 ± 1529	2830 ± 313
1.29-1.44	92634 ± 1603	19417 ± 1549	2915 ± 305
1.44-1.63	97711 ± 1578	20668 ± 1508	3841 ± 318
1.63-1.95	130883 ± 1868	25666 ± 1798	3543 ± 372
1.95-4.00	286161 ± 2776	59570 ± 2661	9713 ± 612

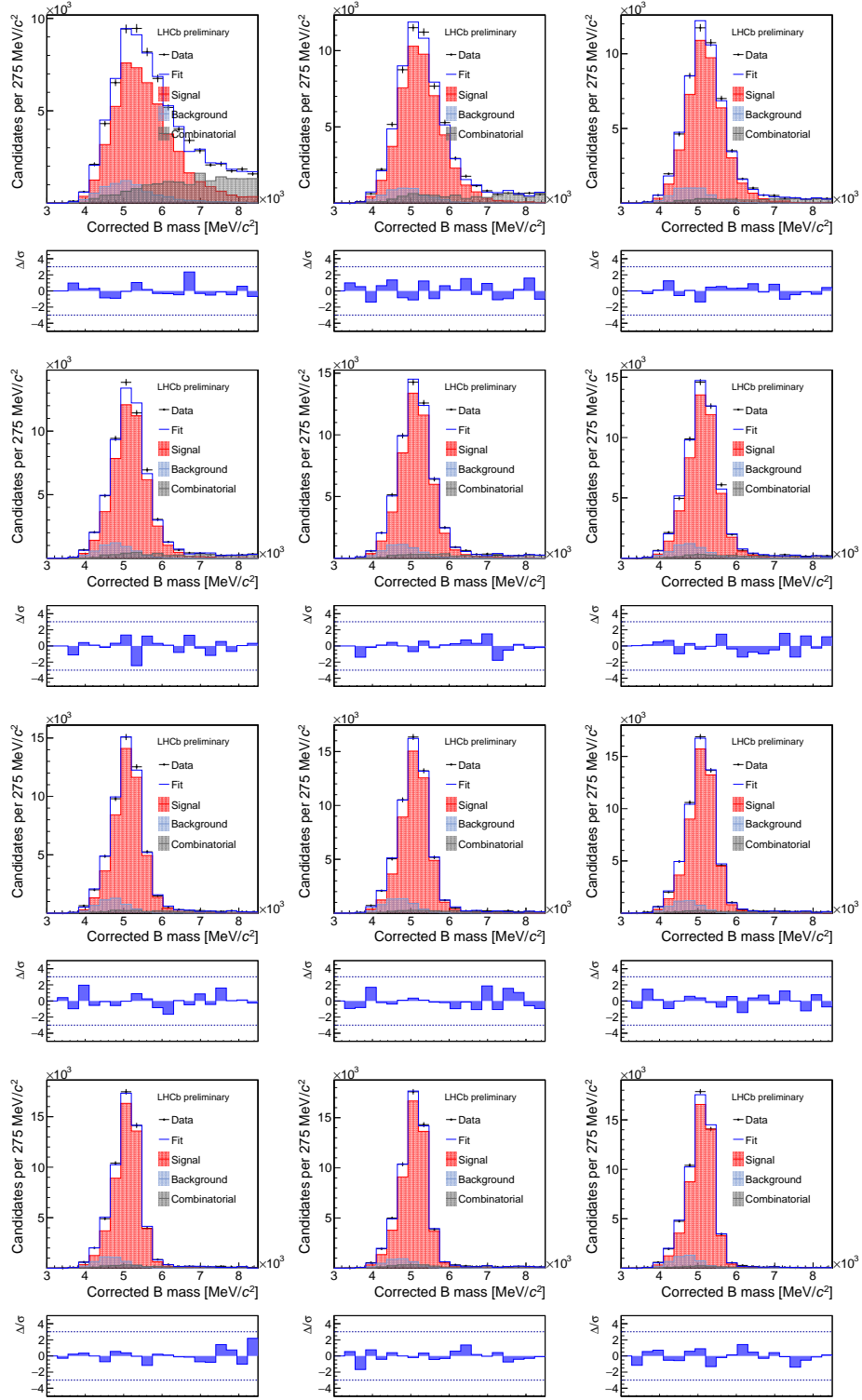Table A.11 – Yields of the components of the B^0 ($K^+\pi^-\pi^-$) mass fit in bins of D decay time.

Figure A.1 – Fits of the $K^+ K^- \pi^- \mu^+$ corrected mass for the B_s^0 sample in bins of corrected decay time (12 first bins).
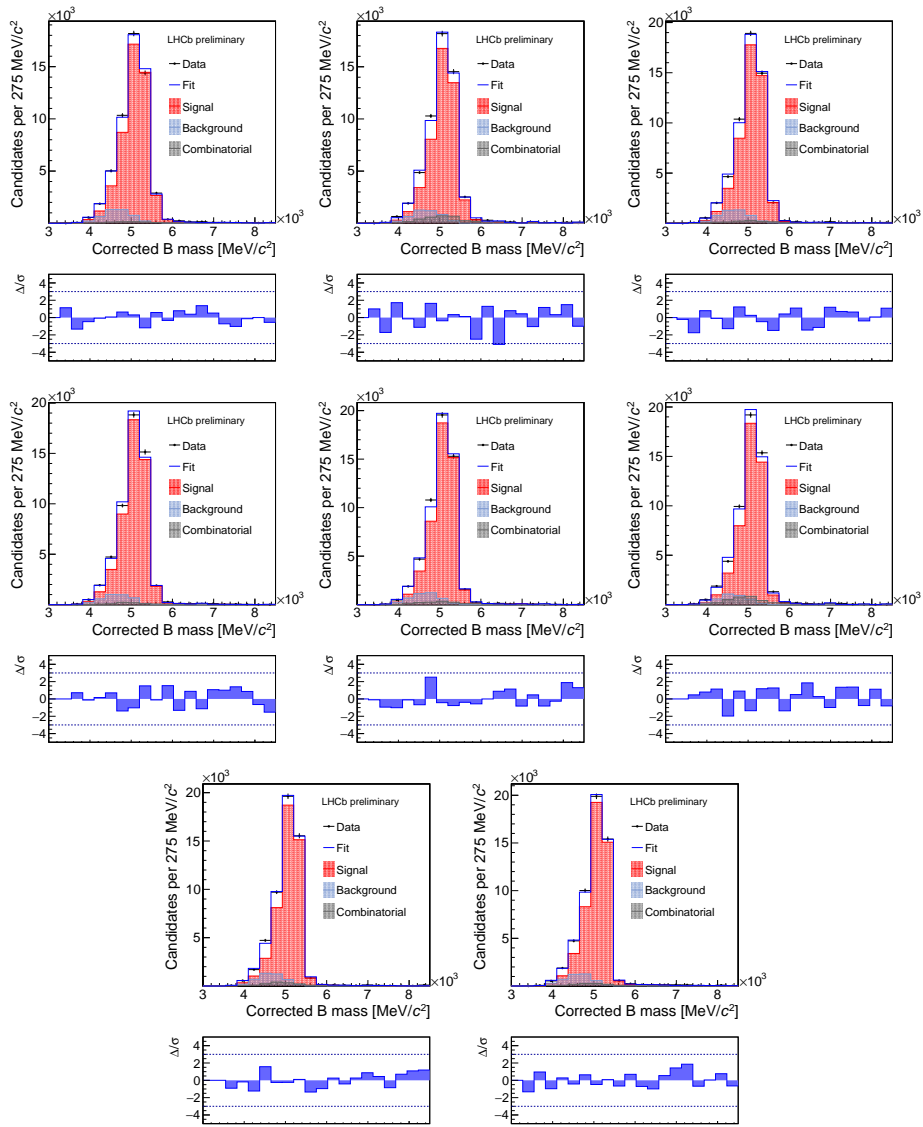
Figure A.2 – Fits of the $K^+K^-\pi^-\mu^+$ corrected mass for the B_s^0 sample in bins of corrected decay time (8 last bins).
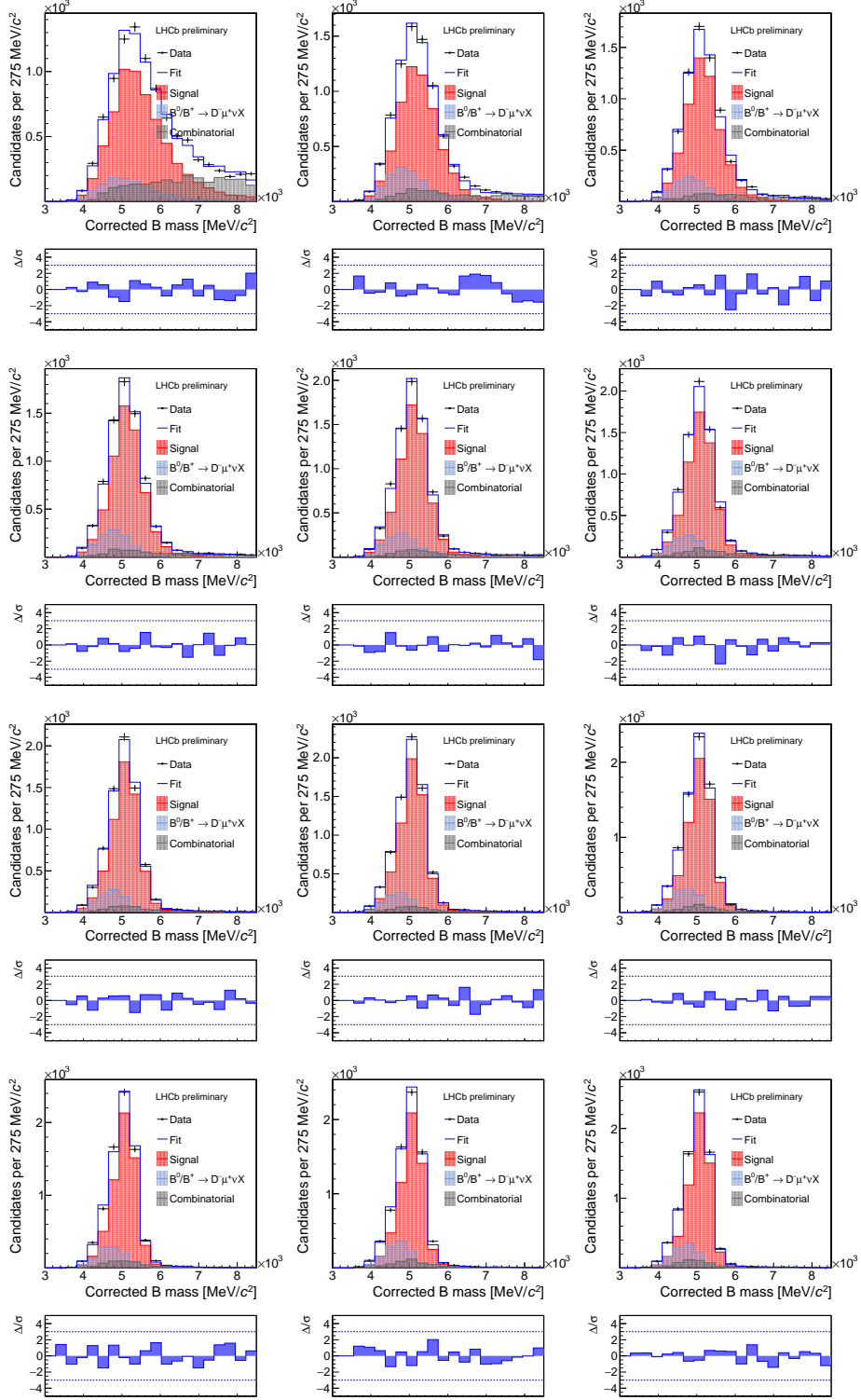
Figure A.3 – Fits of the $K^+ K^- \pi^- \mu^+$ corrected mass for the B^0 ($K^+ K^- \pi^-$) sample in bins of corrected decay time (12 first bins).

Figure A.4 – Fits of the $K^+K^-\pi^-\mu^+$ corrected mass for the B^0 ($K^+K^-\pi^-$) sample in bins of corrected decay time (8 last bins).

Figure A.5 – Fits of the $K^+\pi^-\pi^-\mu^+$ corrected mass for the B^0 ($K^+\pi^-\pi^-$) sample in bins of corrected decay time (12 first bins).
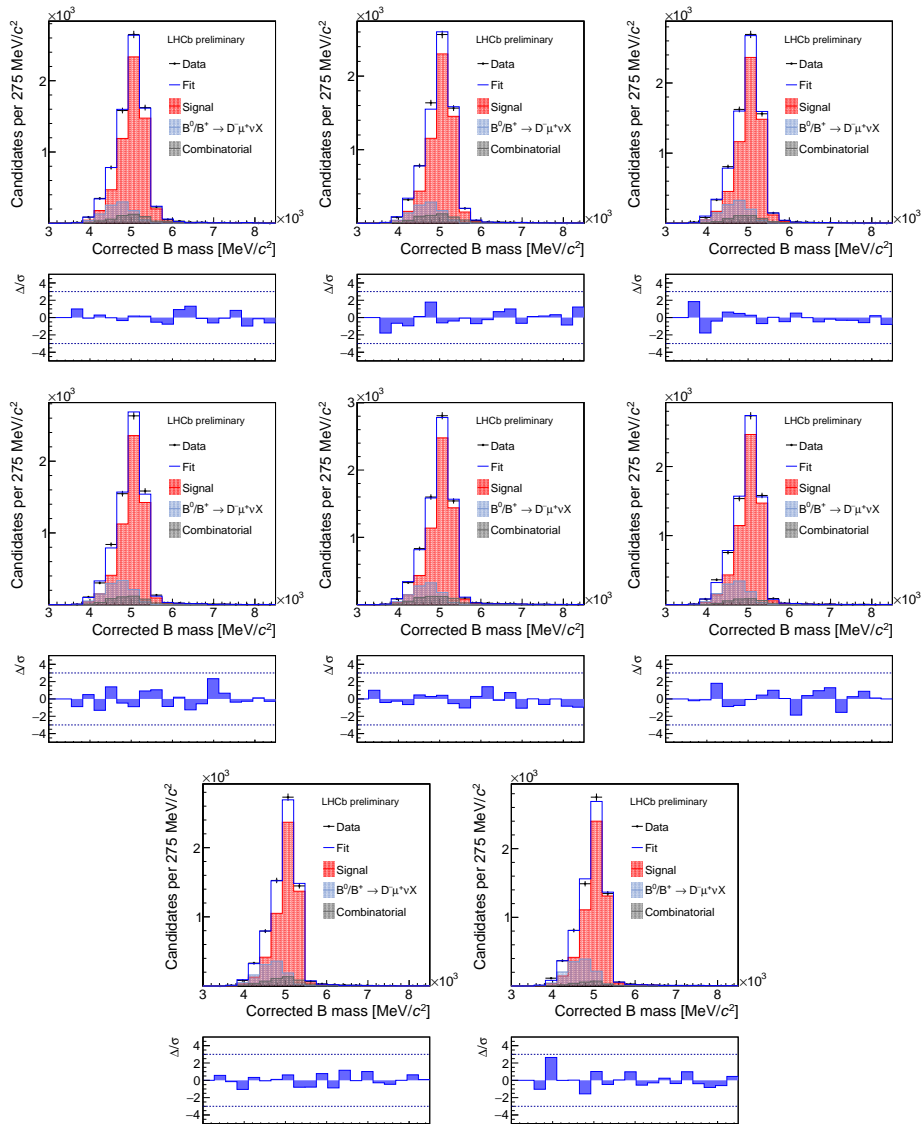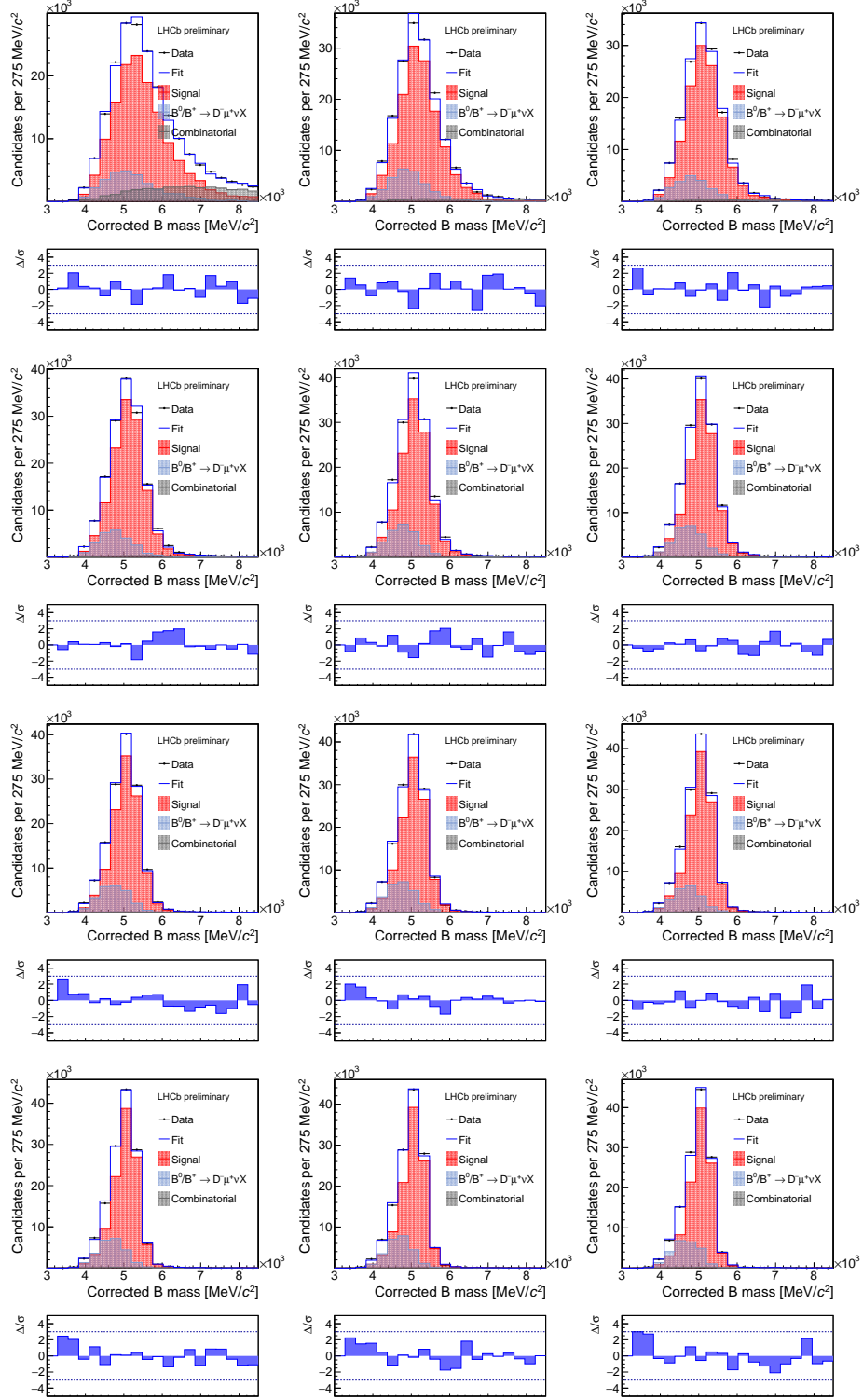
Figure A.6 – Fits of the $K^+\pi^-\pi^-\mu^+$ corrected mass for the B^0 ($K^+\pi^-\pi^-$) sample in bins of corrected decay time (8 last bins).
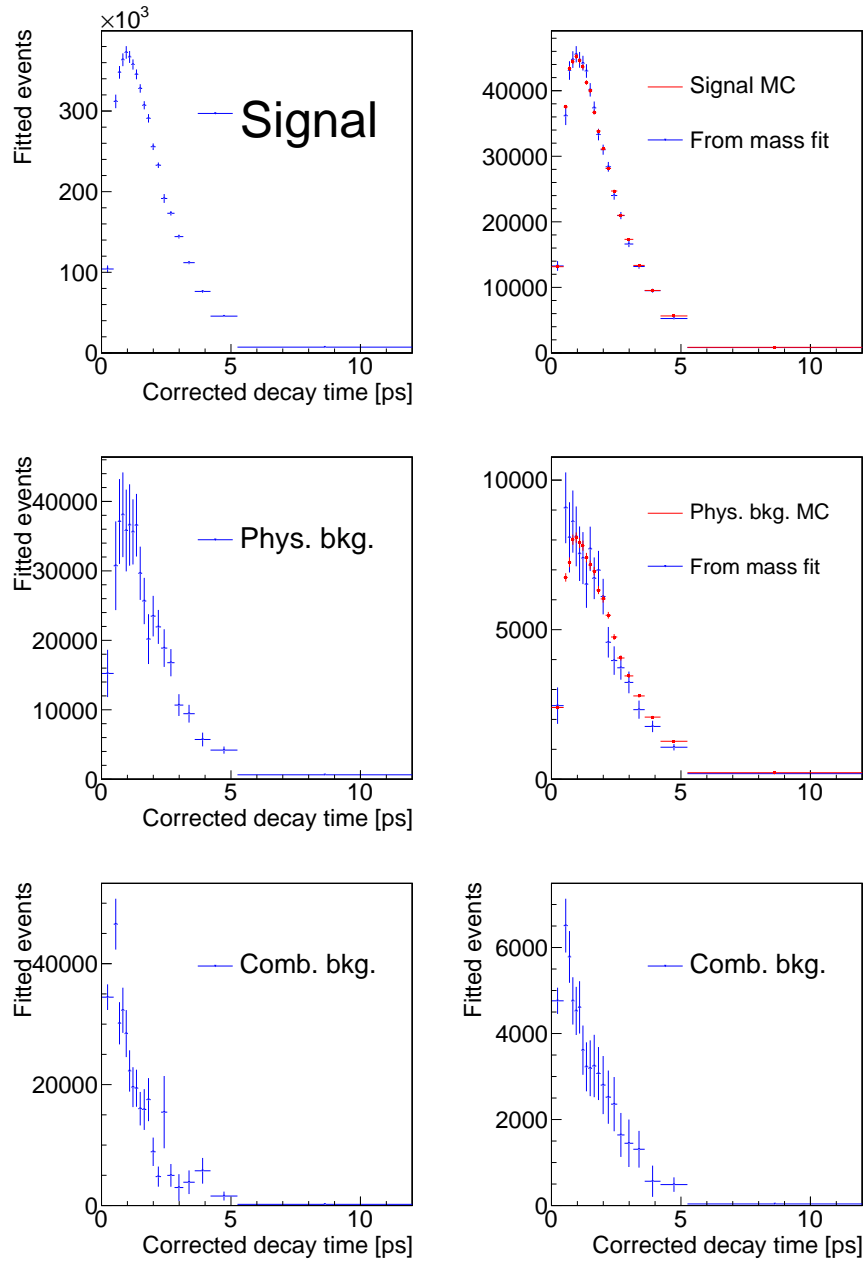
Figure A.7 – Corrected-decay-time distributions of the components of the (left column) B_s^0 and (right column) B^0 samples as found from the mass fit in bins of decay time: first row, the signal; second row, physics backgrounds; third row, combinatorial background. We compare the distributions of the B^0 signal and physics background with the ones expected from simulations.
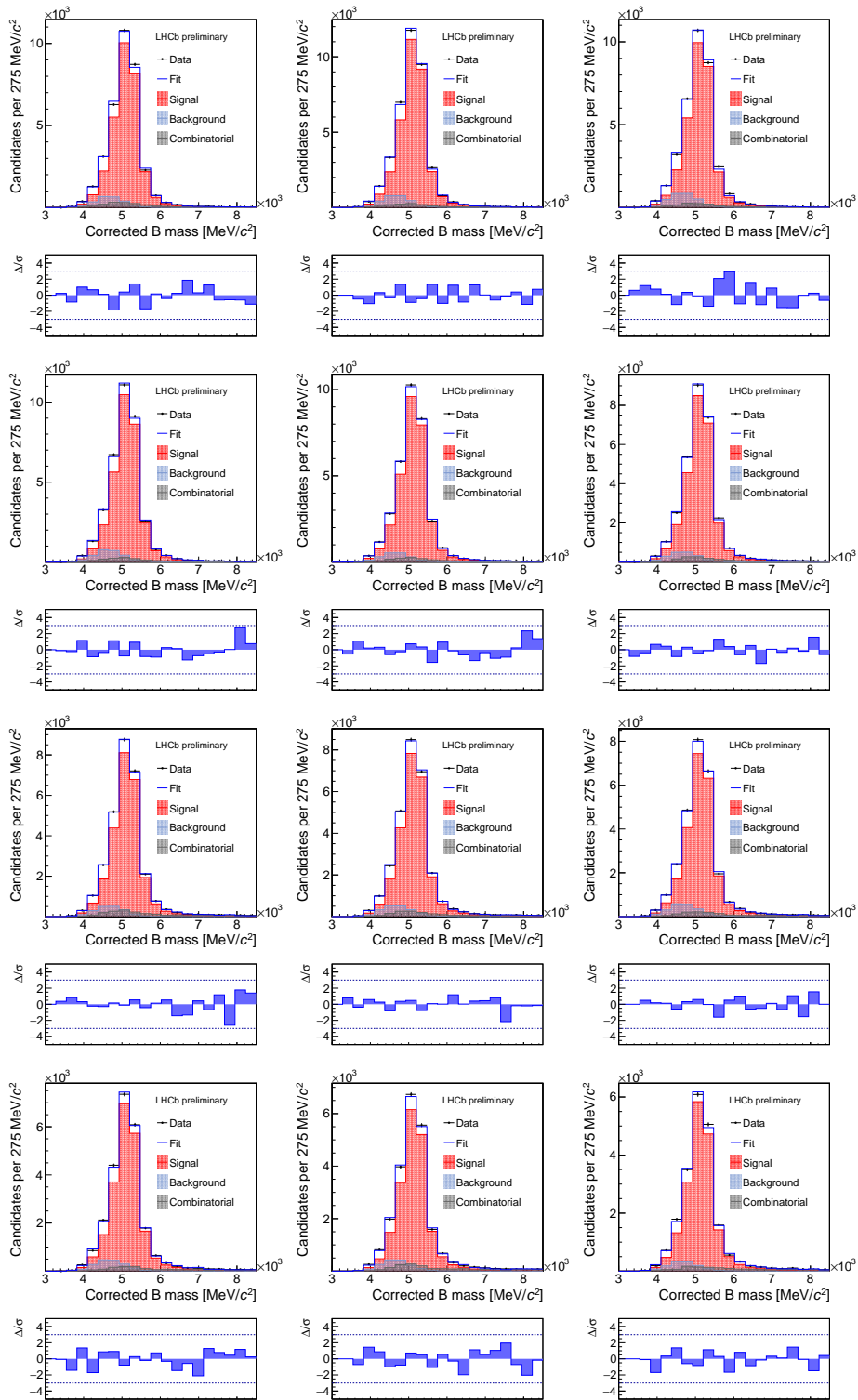
Figure A.8 – Fits of the $K^+K^-\pi^-\mu^+$ corrected mass for the B_s^0 sample in bins of D decay time (12 first bins).
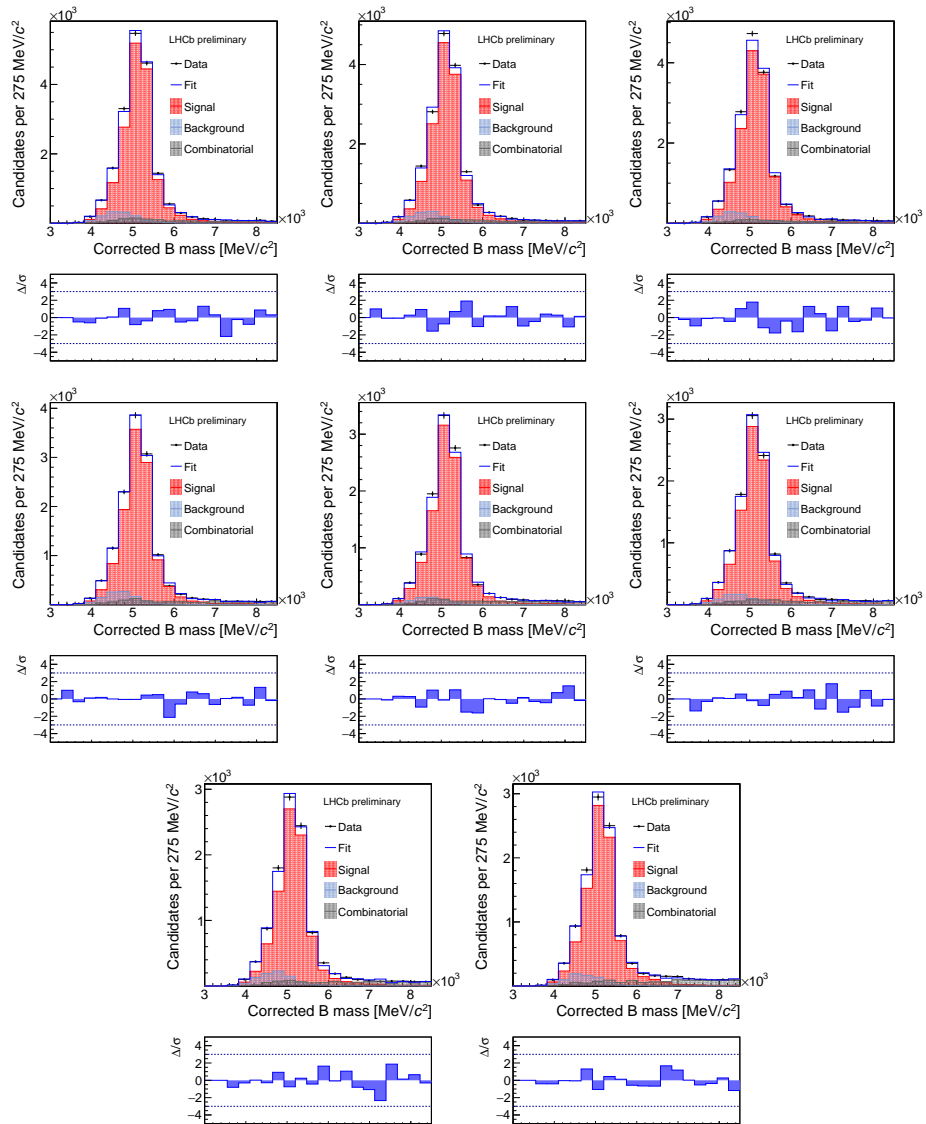
Figure A.9 – Fits of the $K^+ K^- \pi^- \mu^+$ corrected mass for the B_s^0 sample in bins of D decay time (8 last bins).
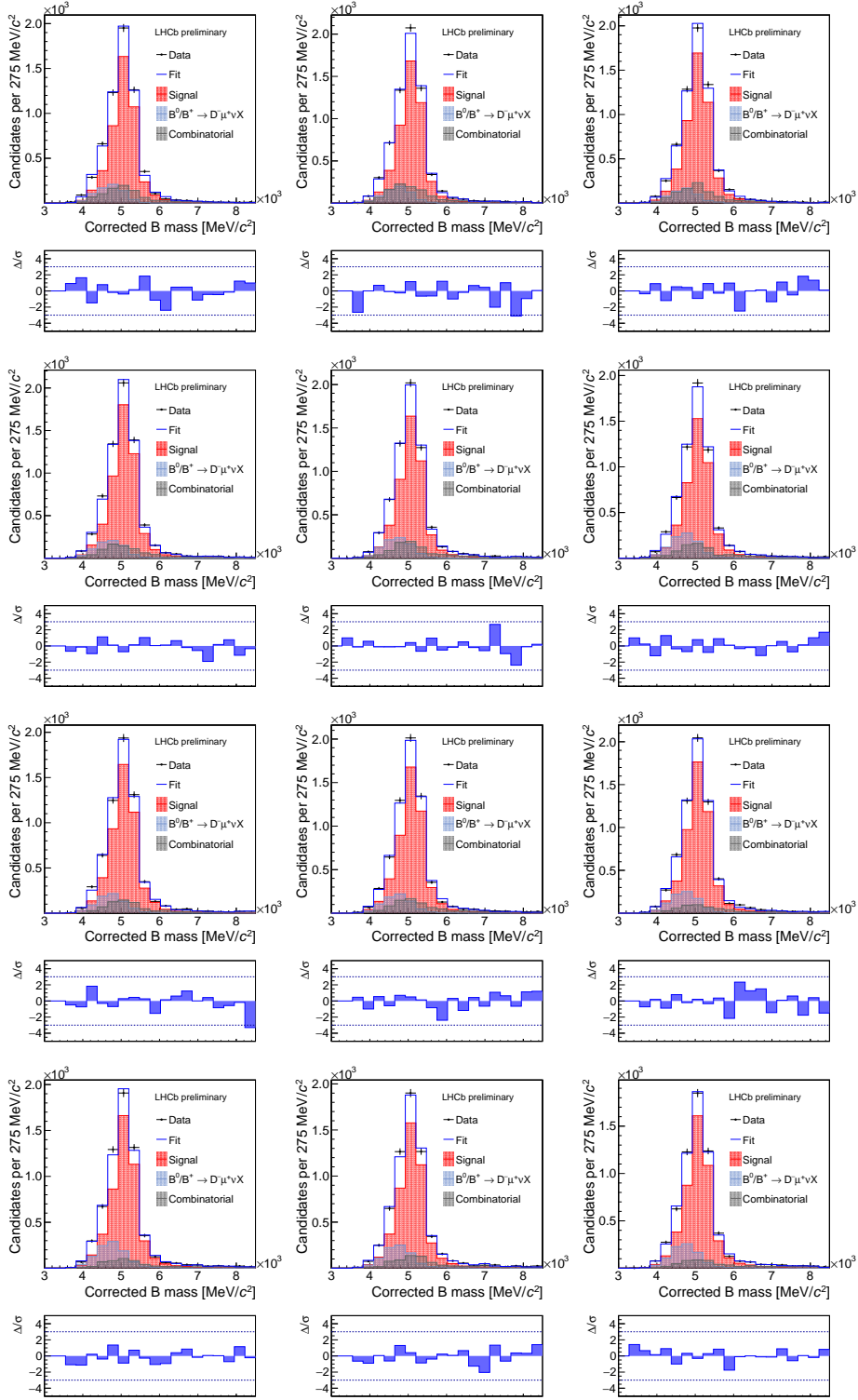
Figure A.10 – Fits of the $K^+K^-\pi^-\mu^+$ corrected mass for the B^0 ($K^+K^-\pi^-$) sample in bins of D decay time (12 first bins).

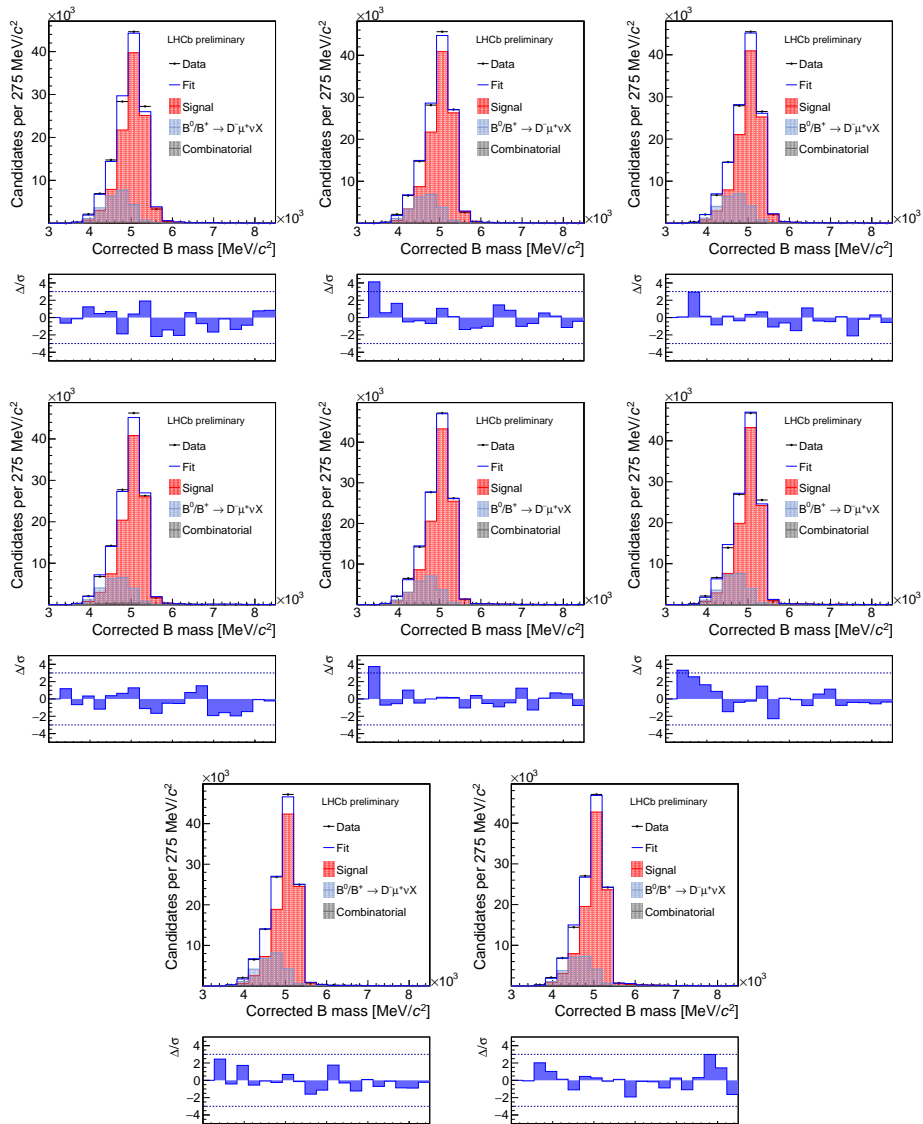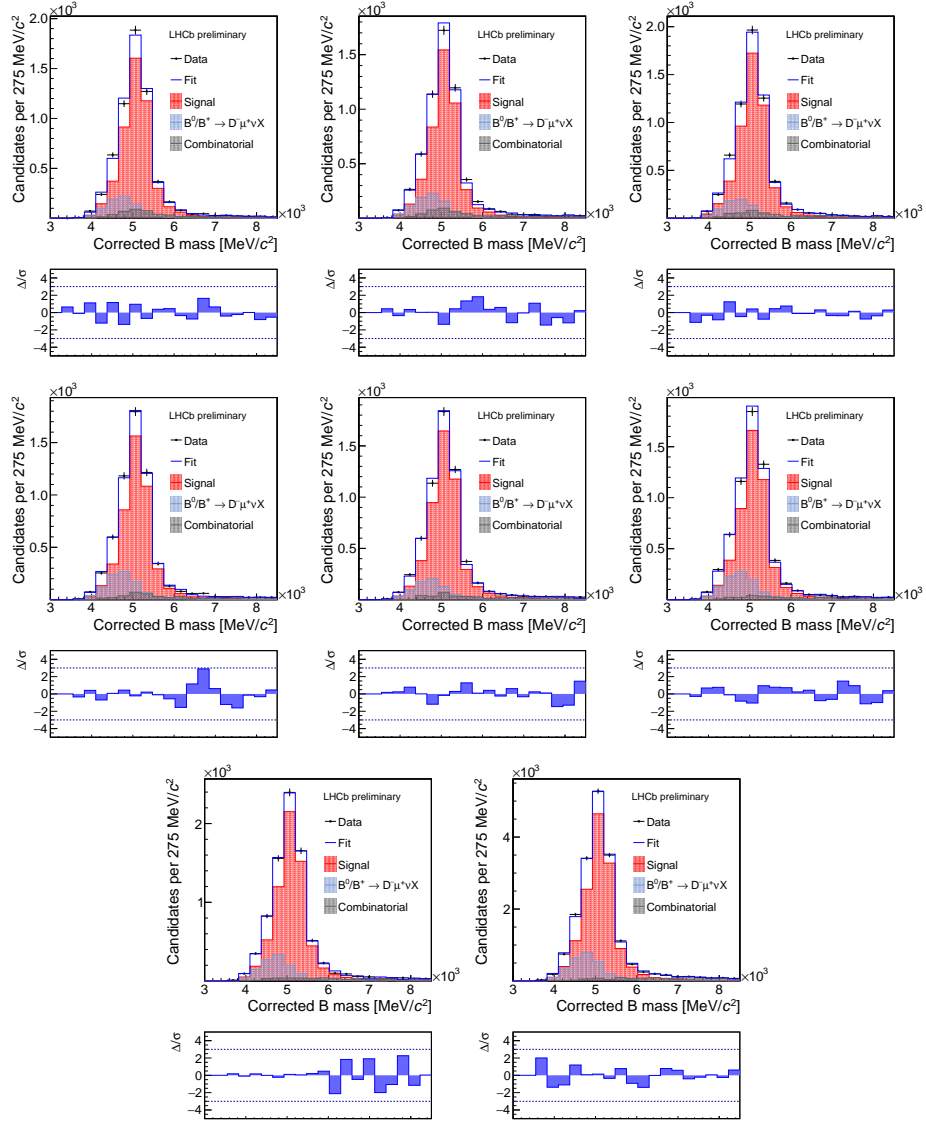Figure A.11 – Fits of the $K^+K^-\pi^-\mu^+$ corrected mass for the B^0 ($K^+K^-\pi^-$) sample in bins of D decay time (8 last bins).
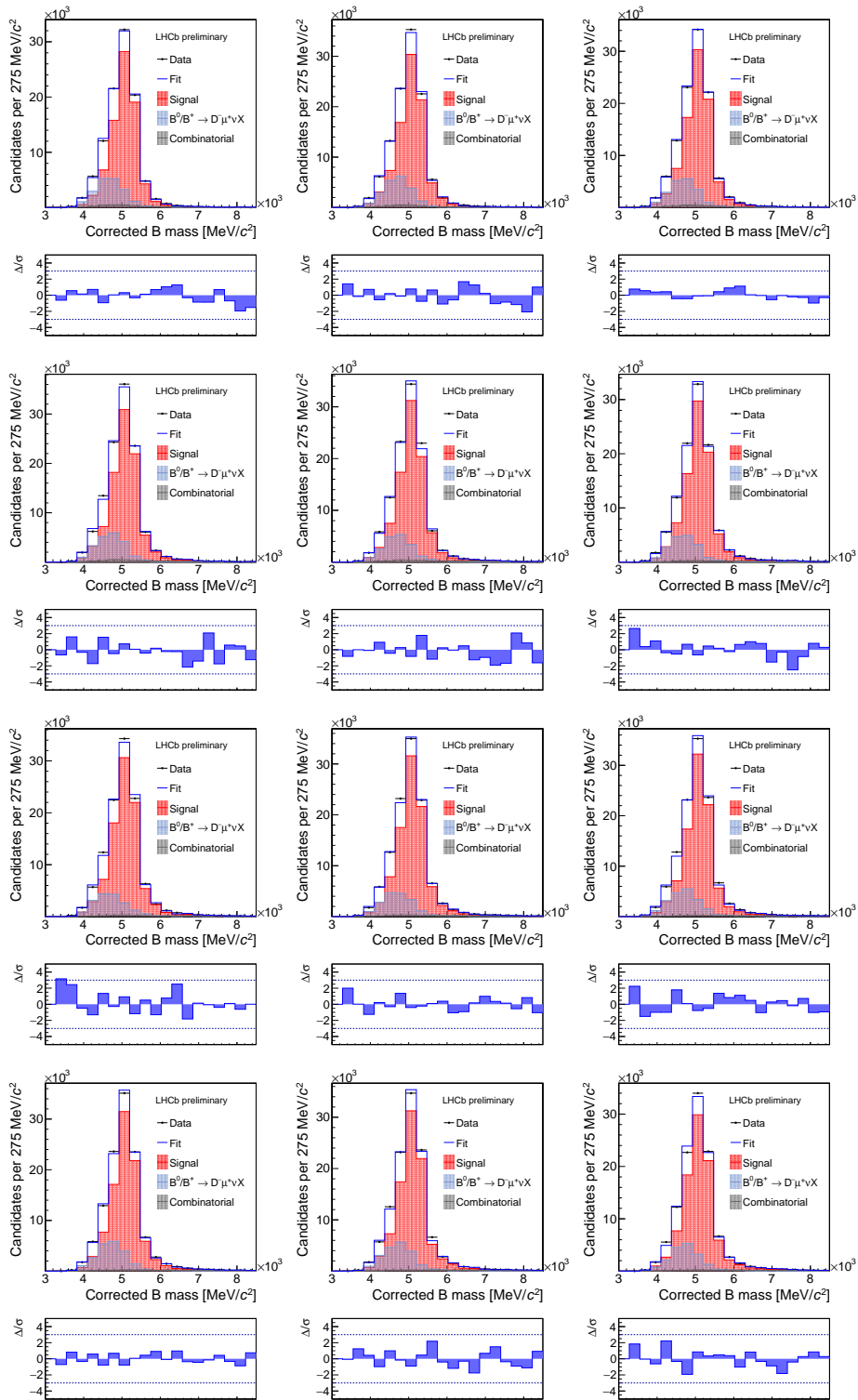
Figure A.12 – Fits of the $K^+\pi^-\pi^-\mu^+$ corrected mass for the B^0 ($K^+\pi^-\pi^-$) sample in bins of D decay time (12 first bins).
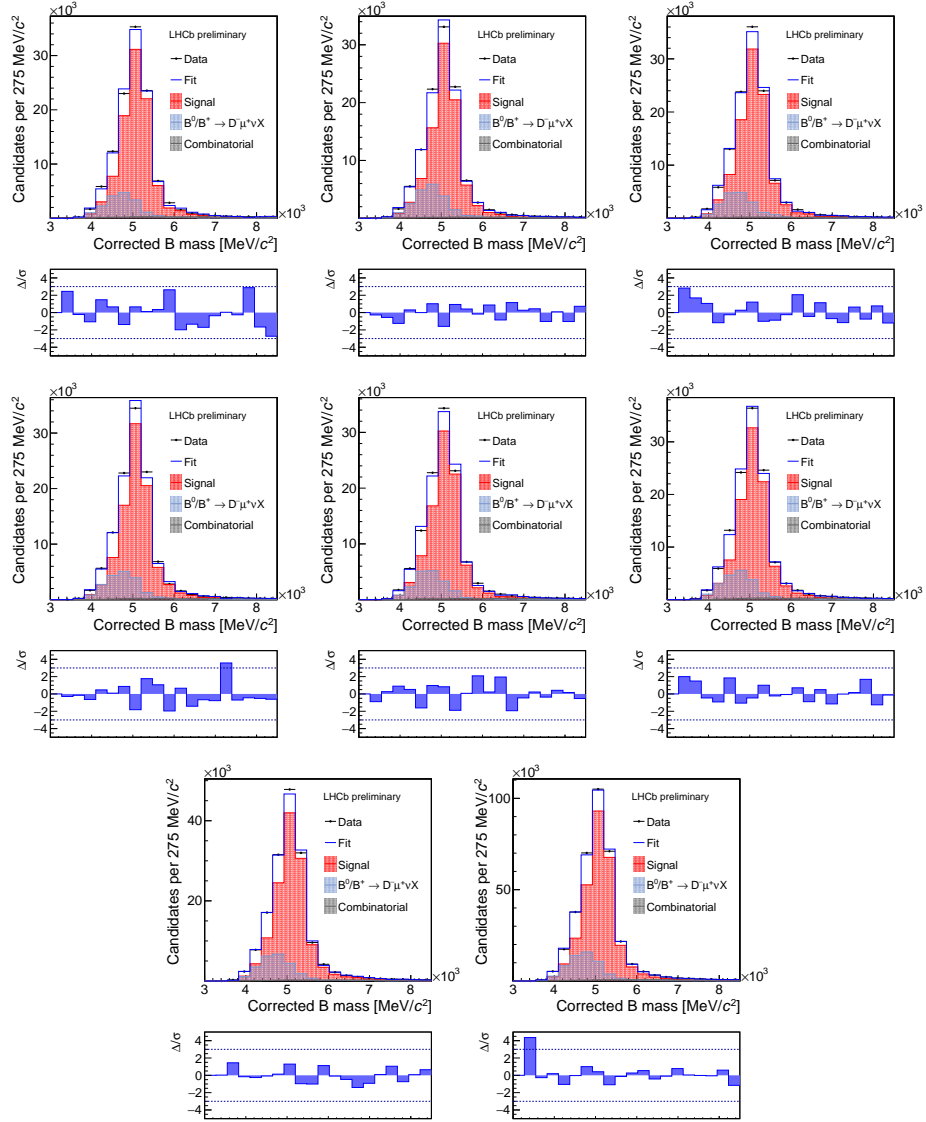
Figure A.13 – Fits of the $K^+\pi^-\pi^-\mu^+$ corrected mass for the B^0 ($K^+\pi^-\pi^-$) sample in bins of D decay time (8 last bins).
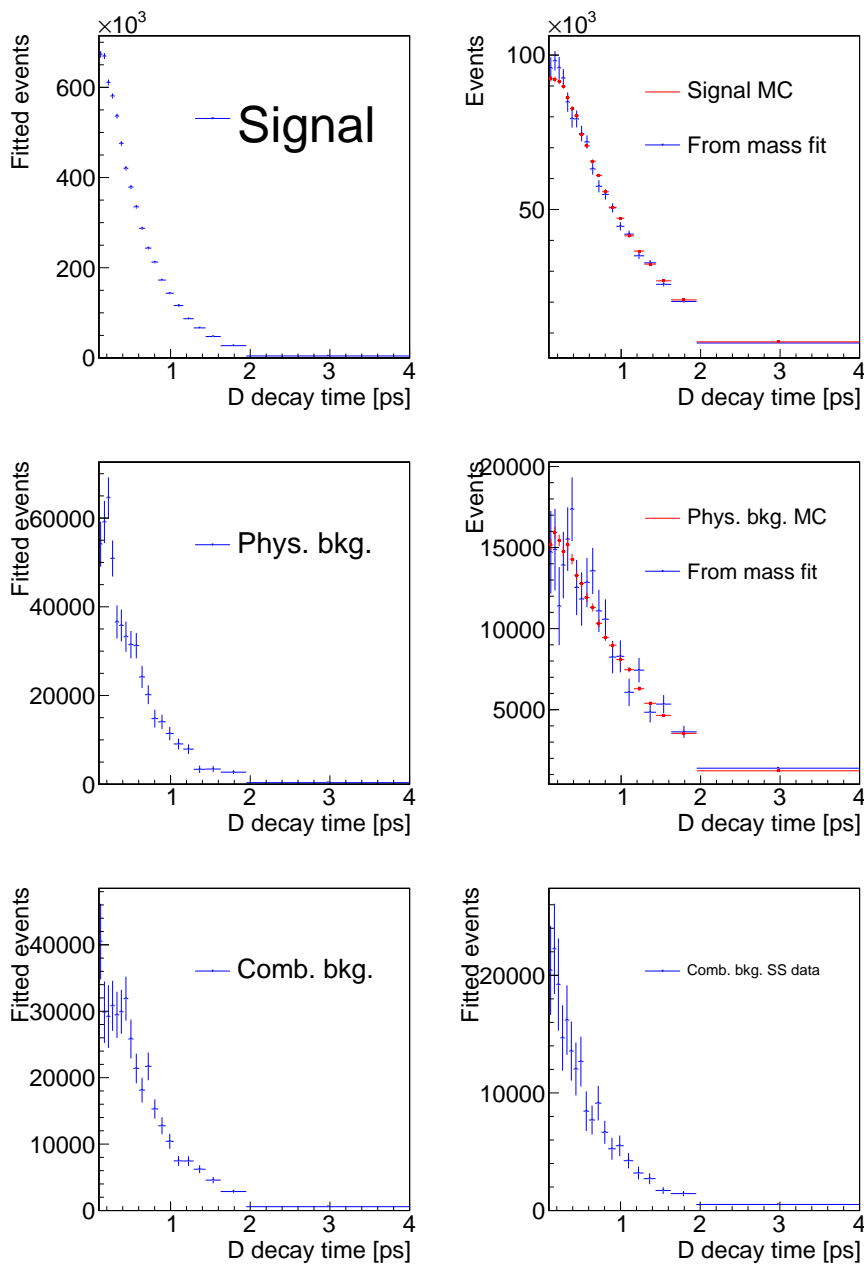
Figure A.14 – D-decay-time distributions of the components of the (left panels) B_s^0 and (right panels) B^0 samples for (first row) signal, (second row) physics backgrounds, and (third row) combinatorics, as determined from the mass fit in bins of D decay time. The distributions of the B^0 signal and physics background are compared with the ones expected from simulations (in red).

A.3 Sample composition of the weighted B_s^0 sample

The results of the fit of the sample composition of the B_s^0 data set after the reweighting of the D_s^+ candidates decay time (Sect. 3.6.2) are reported in Tab. A.12. The signal fractions present values consistent with the results obtained in Tab. 3.9. In Fig. A.15 we report the corrected B mass distribution of the B_s^0 weighted sample with fit projections overlaid.

Component	Fit fraction [%]
$B_s^0 \to D_s^- \mu^+ \nu$	29.30 ± 0.75
$B_s^0 \to D_s^{*-} \mu^+ \nu$	56.17 ± 1.32
$B_s^0 \to D_{(s)}^{(**)}(D_s)X$	3.99 ± 1.04
$B_s^0 \to D_s(K\mu\nu)(\tau\nu)$	3.66 ± 0.39
Combinatorial	6.87 ± 0.23

Table A.12 – Results of the fit to the corrected B mass distribution of the B_s^0 sample after the reweighting of the D_s^+ candidates decay time (Sect. 3.6.2).
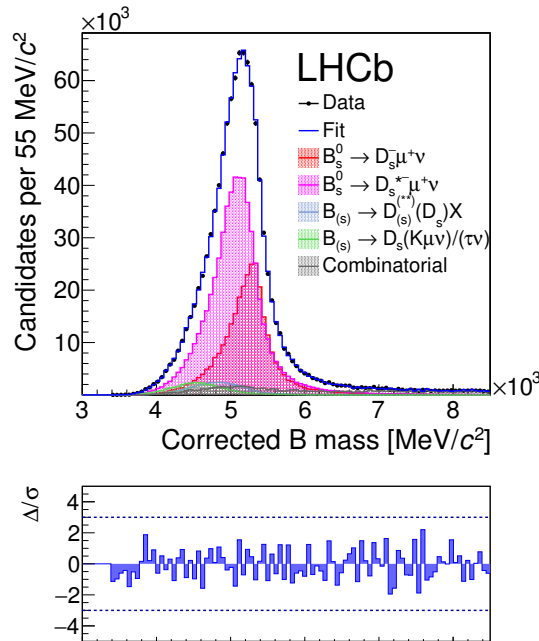
Figure A.15 – Distribution of the corrected B mass distribution of the B_s^0 sample after the reweighting of the D_s^+ candidates decay time, with fit projections overlaid.

A.4   Mass fit in bins of decay time for the $\Delta(D')$ measurement

Details of the mass fits in bins of the decay time of Sec. 4.3.2 are presented here.

The yields in bins of the D decay time of each component are reported in a Tabs. A.13 and A.14 for the D^0 and D^- samples, respectively. The fit projections are shown in Figs. A.16–A.19. For each decay time bin, the fit quality is satisfactory. In some bins of the D^0 sample, the combinatorial yield is negative, but compatible with zero within two standard deviations.

| Time [ps]	Signal	Physics bkg	Combinatorial
0.000-0.045	97296 ± 829	13566 ± 772	-725 ± 391
0.045-0.085	106240 ± 843	13715 ± 801	294 ± 288
0.085-0.120	98698 ± 848	11811 ± 774	-568 ± 308
0.120-0.155	95894 ± 843	12588 ± 763	-264 ± 339
0.155-0.190	91505 ± 831	11835 ± 770	101 ± 208
0.190-0.225	85553 ± 820	11670 ± 766	170 ± 193
0.225-0.265	91748 ± 825	11597 ± 761	-6 ± 357
0.265-0.305	83173 ± 823	11846 ± 756	-128 ± 316
0.305-0.345	77938 ± 769	9114 ± 697	277 ± 262
0.345-0.390	78330 ± 776	10146 ± 698	263 ± 231
0.390-0.435	71298 ± 720	9016 ± 663	359 ± 167
0.435-0.485	70406 ± 781	9125 ± 717	89 ± 205
0.485-0.540	69042 ± 712	8513 ± 652	-2 ± 162
0.540-0.605	69949 ± 692	8942 ± 633	425 ± 158
0.605-0.680	68126 ± 748	8730 ± 684	279 ± 163
0.680-0.770	67228 ± 723	8734 ± 660	299 ± 163
0.770-0.885	67467 ± 705	7851 ± 643	400 ± 155
0.885-1.045	66722 ± 685	7402 ± 624	601 ± 141
1.045-1.320	66195 ± 681	8688 ± 620	514 ± 138
1.320-4.000	66025 ± 717	8505 ± 660	951 ± 131

Table A.13 – Yields of the components of the D^0 sample mass fit in bins of D decay time.

Time [ps]	Signal	Physics bkg	Combinatorial
0.000-0.045	59263 ± 1179	14959 ± 1201	5427 ± 796
0.045-0.085	70867 ± 1282	12567 ± 1283	4637 ± 699
0.085-0.120	64505 ± 1217	15404 ± 1144	2645 ± 748
0.120-0.155	64794 ± 1192	15146 ± 1161	3025 ± 604
0.155-0.190	64112 ± 1296	14558 ± 1240	2638 ± 468
0.190-0.225	64375 ± 1171	12946 ± 1153	2353 ± 441
0.225-0.265	70913 ± 1305	15098 ± 1211	2349 ± 484
0.265-0.305	68076 ± 1239	14418 ± 1209	2410 ± 377
0.305-0.345	66884 ± 1230	12473 ± 1179	2493 ± 368
0.345-0.390	72385 ± 1301	13284 ± 1204	2068 ± 437
0.390-0.435	71527 ± 1183	11690 ± 1119	1152 ± 469
0.435-0.485	72836 ± 1250	14073 ± 1187	3085 ± 397
0.485-0.540	77024 ± 1239	13804 ± 1188	2358 ± 315
0.540-0.605	83754 ± 1392	17714 ± 1302	2575 ± 432
0.605-0.680	91184 ± 1447	18733 ± 1392	2355 ± 373
0.680-0.770	101953 ± 1469	19317 ± 1382	2475 ± 400
0.770-0.885	118859 ± 1672	20543 ± 1559	2837 ± 448
0.885-1.045	141190 ± 1826	27839 ± 1749	3495 ± 514
1.045-1.320	196780 ± 2098	37383 ± 1995	3766 ± 534
1.320-4.000	557886 ± 3550	101179 ± 3367	14245 ± 862

Table A.14 – Yields of the components of the D^- sample mass fit in bins of D decay time.

Appendix A. Appendix

Figure A.16 – Fits of the $K^+K^-\pi^-\mu^+$ corrected mass for the D^0 sample in bins of D decay time (12 first bins).

Figure A.17 – Fits of the $K^+K^-\pi^-\mu^+$ corrected mass for the D^0 sample in bins of D decay time (8 last bins).
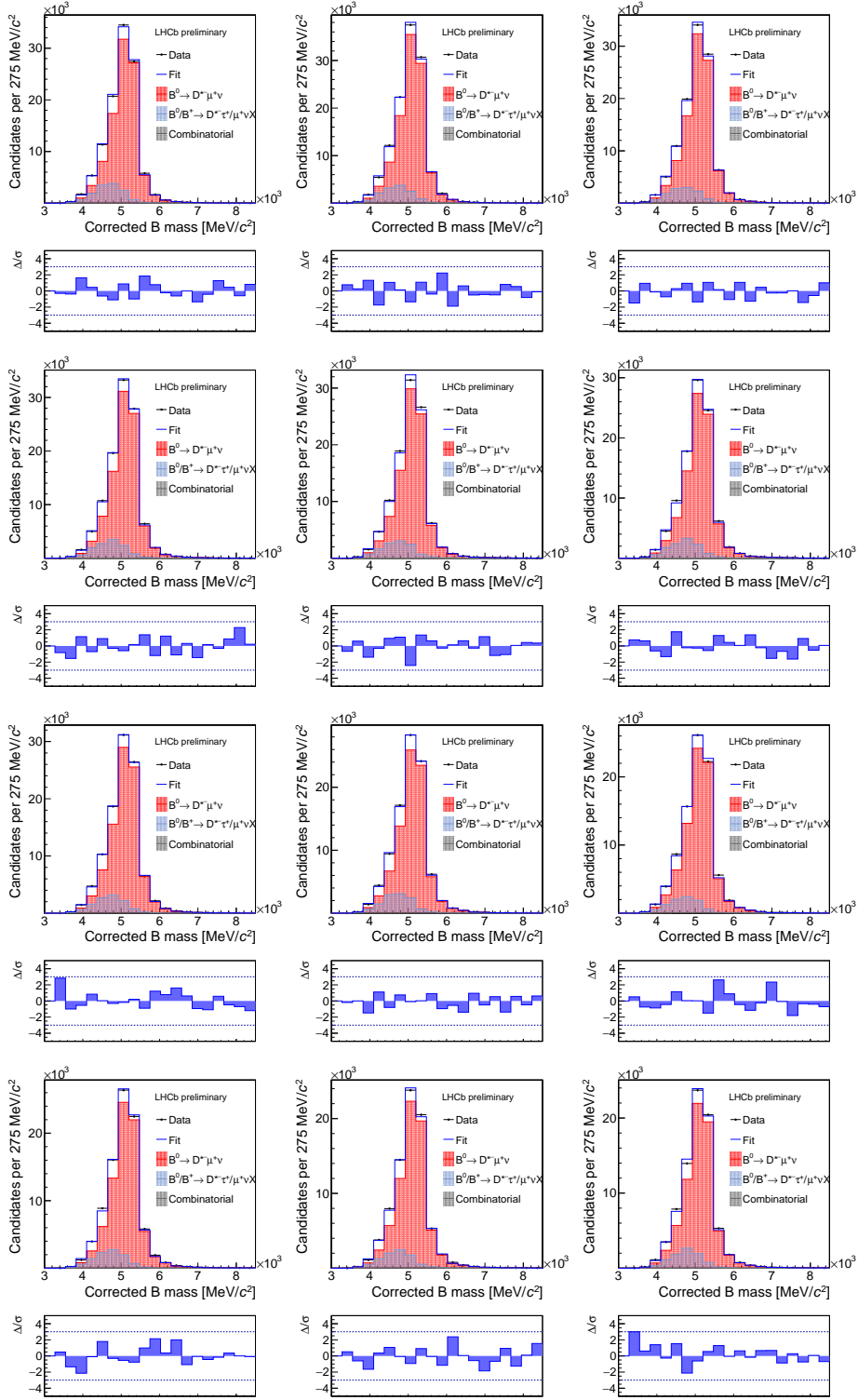
Figure A.18 – Fits of the $K^+\pi^-\pi^-\mu^+$ corrected mass for the D^- sample in bins of D decay time (12 first bins).
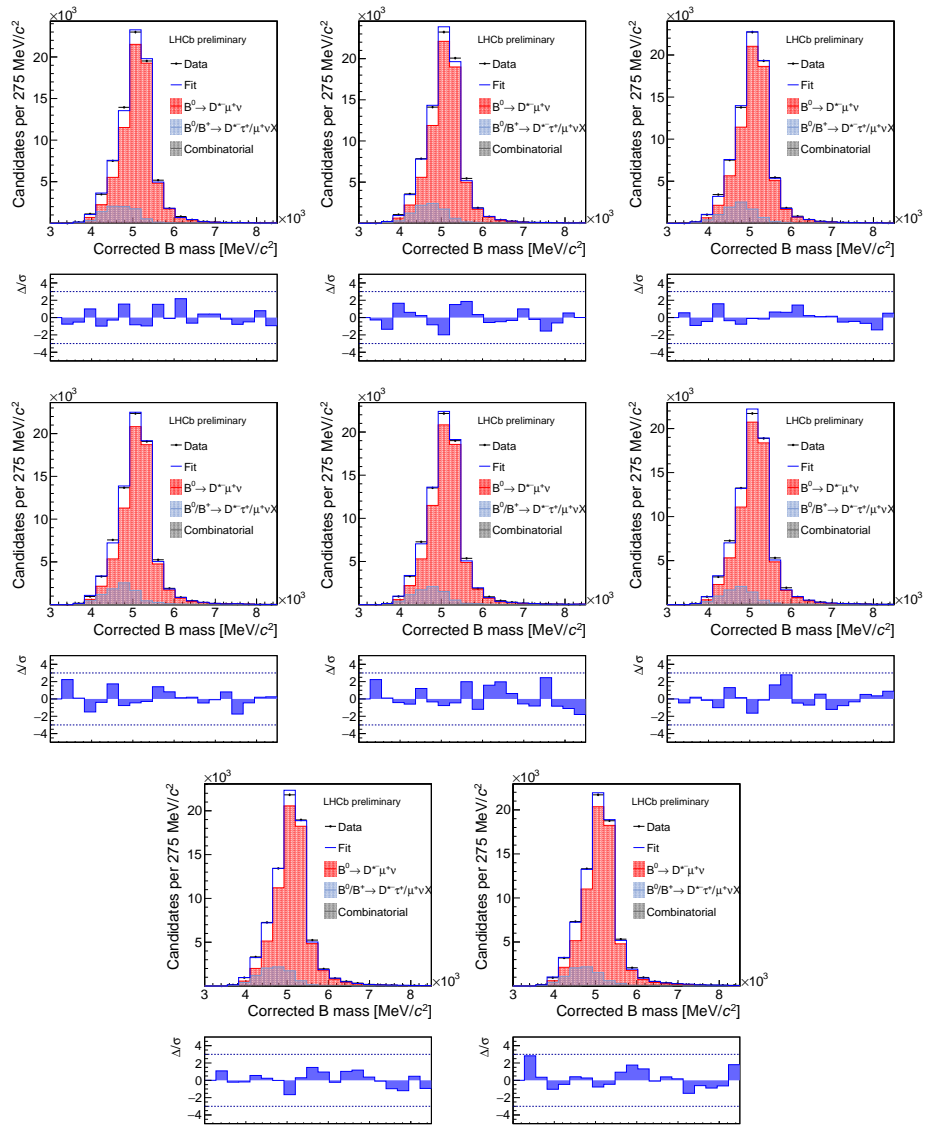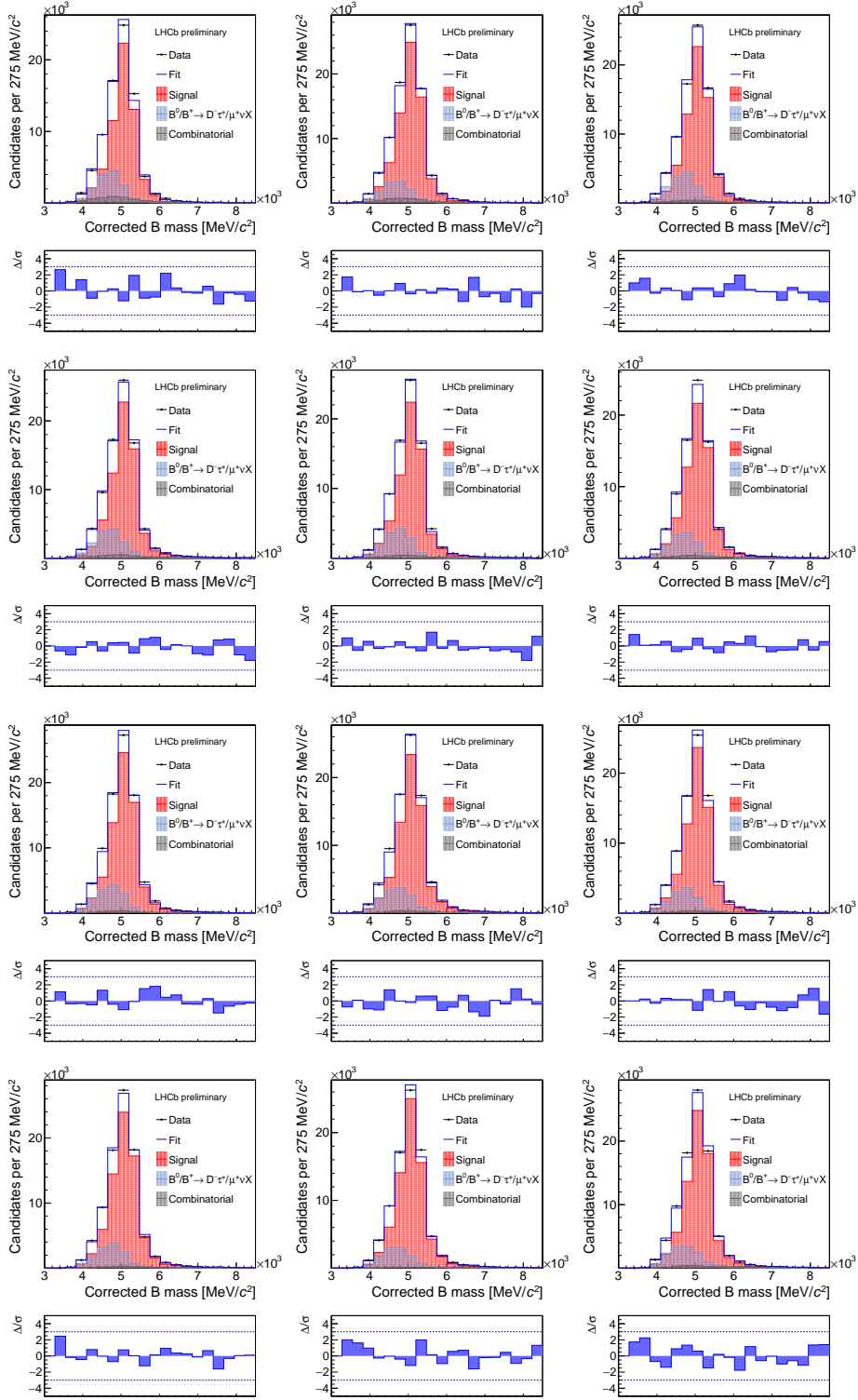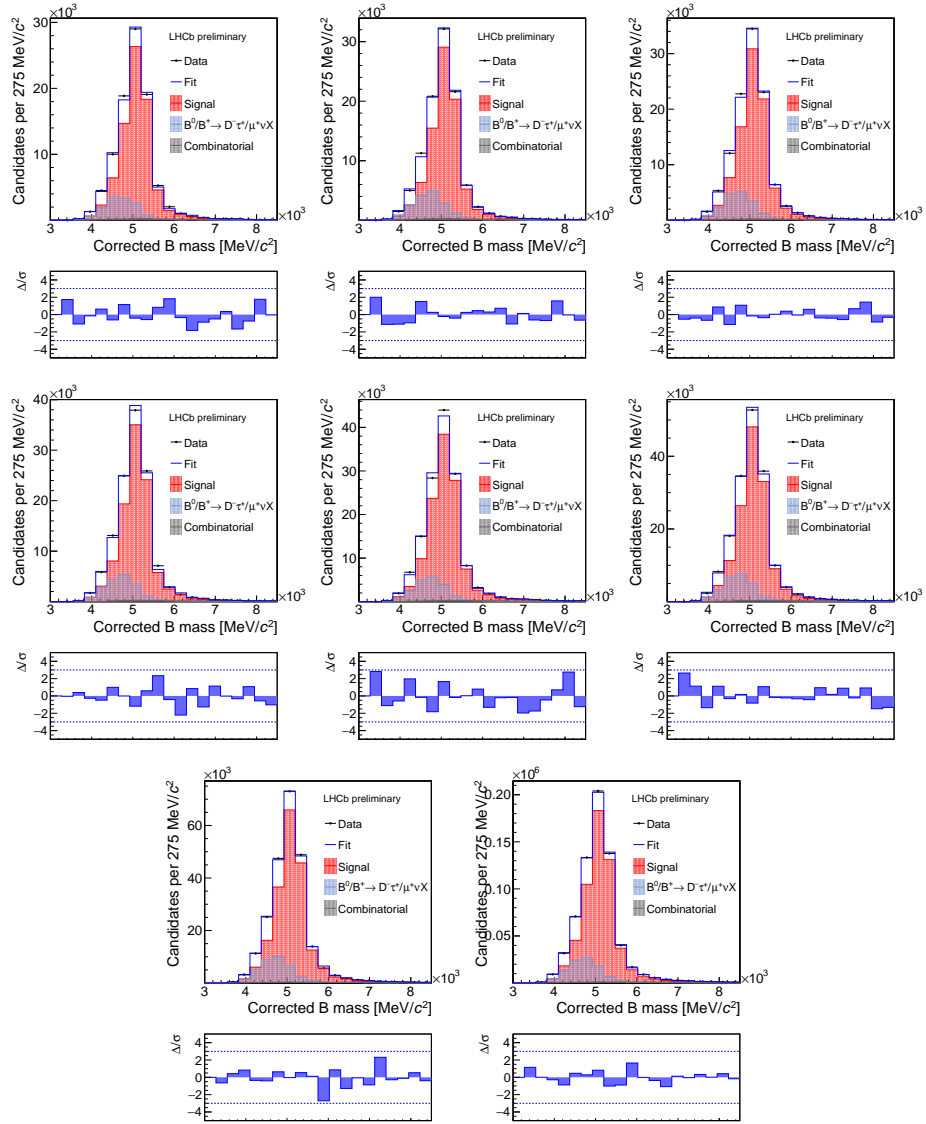
Figure A.19 – Fits of the $K^+\pi^-\pi^-\mu^+$ corrected mass for the D^- sample in bins of D decay time (8 last bins).

Bibliography

[1] LHCb collaboration, R. Aaij *et al.*, *Measurement of B_s^0 and D_s^- meson lifetimes*, Phys. Rev. Lett. **119** (2017) 101801, `arXiv:1705.03475`.

[2] S. L. Glashow, *Partial-symmetries of weak interactions*, Nuclear Physics **22** (1961), no. 4 579 .

[3] S. Weinberg, *A model of leptons*, Phys. Rev. Lett. **19** (1967) 1264.

[4] Belle collaboration, S. K. Choi *et al.*, *Observation of a narrow charmonium-like state in exclusive $B^\pm \to K^\pm \pi^+ \pi^- J/\psi$ decays*, Phys. Rev. Lett. **91** (2003) 262001, `arXiv:hep-ex/0309032`.

[5] LHCb collaboration, R. Aaij *et al.*, *Observation of the resonant character of the $Z(4430)^-$ state*, Phys. Rev. Lett. **112** (2014) 222002, `arXiv:1404.1903`.

[6] LHCb collaboration, R. Aaij *et al.*, *Observation of $J/\psi\, p$ resonances consistent with pentaquark states in $\Lambda_b^0 \to J/\psi\, pK^-$ decays*, Phys. Rev. Lett. **115** (2015) 072001, `arXiv:1507.03414`.

[7] *Standard Model of elementary particles*, https://commons.wikimedia.org/wiki/File: Standard_Model_of_Elementary_Particles.svg. On Wikipedia Commons, accessed on 2018.03.01.

[8] C. Rovelli, *Notes for a brief history of quantum gravity*, in *Recent developments in theoretical and experimental general relativity, gravitation and relativistic field theories. Proceedings, 9th Marcel Grossmann Meeting, MG'9, Rome, Italy, July 2-8, 2000. Pts. A-C*, pp. 742–768, 2000. `arXiv:gr-qc/0006061`.

[9] A. Klein and B. W. Lee, *Does spontaneous breakdown of symmetry imply zero-mass particles?*, Phys. Rev. Lett. **12** (1964) 266.

[10] P. W. Higgs, *Broken symmetries, massless particles and gauge fields*, Phys. Lett. **12** (1964), no. 2 132 .

[11] F. Englert and R. Brout, *Broken symmetry and the mass of gauge vector mesons*, Phys. Rev. Lett. **13** (1964) 321.

Bibliography

[12] ATLAS collaboration, G. Aad *et al.*, *Observation of a new particle in the search for the Standard Model Higgs boson with the ATLAS detector at the LHC*, Phys. Lett. **B716** (2012) 1, `arXiv:1207.7214`.

[13] CMS collaboration, S. Chatrchyan *et al.*, *Observation of a new boson at a mass of 125 GeV with the CMS experiment at the LHC*, Phys. Lett. **B716** (2012) 30, `arXiv:1207.7235`.

[14] J. Schechter and J. W. F. Valle, *Neutrino masses in SU(2) $\otimes$ U(1) theories*, Phys. Rev. D **22** (1980) 2227.

[15] M. Antonelli *et al.*, *Flavor Physics in the Quark Sector*, Phys. Rept. **494** (2010) 197, `arXiv:0907.5386`.

[16] B^0–$\overline{B}^0$ *mixing*, in Ref. [19].

[17] D^0–$\overline{D}^0$ *mixing*, in Ref. [19].

[18] T. Gershon, $\Delta\Gamma_d$*: A forgotten null test of the Standard Model*, J. Phys. **G38** (2011) 015007, `arXiv:1007.5135`.

[19] Particle Data Group, C. Patrignani *et al.*, *Review of particle physics*, Chin. Phys. **C40** (2016) 100001, and 2017 update.

[20] A. Lenz, *Lifetimes and heavy quark expansion*, Int. J. Mod. Phys. **A30** (2015), no. 10 1543005, `arXiv:1405.3601`.

[21] M. Neubert, *Heavy quark effective theory*, Subnucl. Ser. **34** (1997) 98, `arXiv:hep-ph/9610266`.

[22] F. J. Hasert *et al.*, *Search for elastic muon-neutrino electron scattering*, Phys. Lett. **B46** (1973), no. 1 121 .

[23] F. J. Hasert *et al.*, *Observation of neutrino-like interactions without muon or electron in the Gargamelle neutrino experiment*, Phys. Lett. **B46** (1973), no. 1 138 .

[24] UA1, G. Arnison *et al.*, *Experimental observation of isolated large transverse energy electrons with associated missing energy at $\sqrt{s}$ = 540 GeV*, Phys. Lett. **B122** (1983) 103.

[25] UA1, G. Arnison *et al.*, *Experimental observation of lepton pairs of invariant mass around 95 GeV/c^2 at the CERN SPS collider*, Phys. Lett. **B126** (1983) 398.

[26] UA2, P. Bagnaia *et al.*, *Evidence for $Z^0 \rightarrow e^+ e^-$ at the CERN $\overline{p}p$ collider*, Phys. Lett. **B129** (1983) 130.

[27] UA2, M. Banner *et al.*, *Observation of single isolated electrons of high transverse momentum in events with missing transverse energy at the CERN $\overline{p}p$ collider*, Phys. Lett. **B122** (1983) 476.

[28] ALEPH collaboration, D. DeCamp *et al.*, *Determination of the number of light neutrino species*, Phys. Lett. **B231** (1989) 519 .

[29] DELPHI collaboration, P. Aarnio *et al.*, *Measurement of the mass and width of the Z^0 particle from multi-hadronic final states produced in $e^+ e^-$ annihilations*, Phys. Lett. **B231** (1989) 539.

[30] L3 collaboration, B. Adeva *et al.*, *A determination of the properties of the neutral intermediate vector boson Z^0*, Phys. Lett. **B231** (1989) 509.

[31] OPAL collaboration, M. Z. Akrawy *et al.*, *Measurement of the Z^0 mass and width with the OPAL detector at LEP*, Phys. Lett. **B231** (1989) 530.

[32] G. Apollinari *et al.*, *High-Luminosity Large Hadron Collider (HL-LHC): Preliminary Design Report*, CERN Yellow Reports: Monographs, CERN, Geneva, 2015.

[33] E. Mobs, *The CERN accelerator complex. Complexe des accélérateurs du CERN*, https://cds. cern. ch/record/2197559 (2016).

[34] LHCb collaboration, A. A. Alves Jr. *et al.*, *The LHCb detector at the LHC*, JINST **3** (2008) S08005.

[35] *"Grand Unification" of data taking*, http://lhcb-public.web.cern.ch/lhcb-public/ Welcome.html#End2017. On the LHCb public website, accessed on 2018.03.01.

[36] LHCb collaboration, *LHCb VELO (VErtex LOcator): Technical Design Report*, CERN-LHCC-2001-011. LHCb-TDR-005.

[37] R. Aaij *et al.*, *Performance of the LHCb Vertex Locator*, JINST **9** (2014) P09007, arXiv:1405.7808.

[38] LHCb collaboration, *LHCb reoptimized detector design and performance: Technical Design Report*, CERN-LHCC-2003-030. LHCb-TDR-009.

[39] LHCb collaboration, *LHCb inner tracker: Technical Design Report*, CERN-LHCC-2002-029. LHCb-TDR-008.

[40] LHCb collaboration, *LHCb outer tracker: Technical Design Report*, CERN-LHCC-2001-024. LHCb-TDR-006.

[41] R. Arink *et al.*, *Performance of the LHCb Outer Tracker*, JINST **9** (2014) P01002, arXiv:1311.3893.

[42] LHCb collaboration, *LHCb RICH: Technical Design Report*, CERN-LHCC-2000-037. LHCb-TDR-003.

[43] M. Adinolfi *et al.*, *Performance of the LHCb RICH detector at the LHC*, Eur. Phys. J. **C73** (2013) 2431, arXiv:1211.6759.

[44] LHCb collaboration, *LHCb calorimeters: Technical Design Report*, CERN-LHCC-2000-036. LHCb-TDR-002.

[45] LHCb collaboration, *LHCb muon system: Technical Design Report*, CERN-LHCC-2001-010. LHCb-TDR-004.

[46] F. Archilli *et al.*, *Performance of the muon identification at LHCb*, JINST **8** (2013) P10020, `arXiv:1306.0249`.

[47] G. Dujany and B. Storaci, *Real-time alignment and calibration of the LHCb detector in Run II*, No. LHCb-PROC-2015-011, 2015.

[48] LHCb collaboration, A. Contu, *Status and prospects for the LHCb upgrade*, in *Proceedings, 6th International Workshop on Charm Physics (Charm 2013): Manchester, UK*, 2013. `arXiv:1311.3496`.

[49] M. Clemencic *et al.*, *The LHCb simulation application, Gauss: Design, evolution and experience*, J. Phys. Conf. Ser. **331** (2011) 032023.

[50] T. Sjöstrand, S. Mrenna, and P. Skands, *A brief introduction to PYTHIA 8.1*, Comput. Phys. Commun. **178** (2008) 852, `arXiv:0710.3820`.

[51] T. Sjöstrand, S. Mrenna, and P. Skands, *PYTHIA 6.4 physics and manual*, JHEP **05** (2006) 026, `arXiv:hep-ph/0603175`.

[52] D. J. Lange, *The EvtGen particle decay simulation package*, Nucl. Instrum. Meth. **A462** (2001) 152.

[53] P. Golonka and Z. Was, *PHOTOS Monte Carlo: A precision tool for QED corrections in Z and W decays*, Eur. Phys. J. **C45** (2006) 97, `arXiv:hep-ph/0506026`.

[54] Geant4 collaboration, S. Agostinelli *et al.*, *Geant4: A simulation toolkit*, Nucl. Instrum. Meth. **A506** (2003) 250.

[55] Geant4 collaboration, J. Allison *et al.*, *Geant4 developments and applications*, IEEE Trans. Nucl. Sci. **53** (2006) 270.

[56] *The BOOLE project*, http://lhcb-release-area.web.cern.ch/LHCb-release-area/DOC/boole/.

[57] *The BRUNEL project*, http://lhcb-release-area.web.cern.ch/LHCb-release-area/DOC/brunel/.

[58] *The MOORE project*, http://lhcb-release-area.web.cern.ch/LHCb-release-area/DOC/moore/.

[59] *The DAVINCI project*, http://lhcb-release-area.web.cern.ch/LHCb-release-area/DOC/davinci/.

[60] LHCb collaboration, *LHCb Tracker Upgrade Technical Design Report*, CERN-LHCC-2014-001. LHCb-TDR-015.

[61] LHCb collaboration, *Framework TDR for the LHCb Upgrade: Technical Design Report*, CERN-LHCC-2012-007. LHCb-TDR-012.

[62] LHCb collaboration, *LHCb VELO Upgrade Technical Design Report*, CERN-LHCC-2013-021. LHCb-TDR-013.

[63] LHCb collaboration, *LHCb PID Upgrade Technical Design Report*, CERN-LHCC-2013-022. LHCb-TDR-014.

[64] LHCb collaboration, *LHCb Trigger and Online Technical Design Report*, CERN-LHCC-2014-016. LHCb-TDR-016.

[65] LHCb collaboration, *Expression of Interest for a Phase-II LHCb Upgrade: Opportunities in flavour physics, and beyond, in the HL-LHC era*, CERN-LHCC-2017-003.

[66] Kuonen, A. *et al.*, *Characterisation of the Hamamatsu MPPC multichannel array for the LHCb SciFi Tracker v.11.2016*, LPHE-2017-001 and other publication in preparation.

[67] D0 collaboration, V. M. Abazov *et al.*, *Measurement of the B_s^0 lifetime in the flavor-specific decay channel $B_s^0 \to D_s^- \mu^+ \nu X$*, Phys. Rev. Lett. **114** (2015) 062001, arXiv:1410.1568.

[68] LHCb collaboration, R. Aaij *et al.*, *Measurement of the $\overline{B}_s^0$ meson lifetime in $D_s^+ \pi^-$ decays*, Phys. Rev. Lett. **113** (2014) 172001, arXiv:1407.5873.

[69] K. Kodama *et al.*, *Measurement of the relative branching fraction $\Gamma(D^0 \to K\mu\nu)/\Gamma(D^0 \to \mu X)$*, Phys. Rev. Lett. **66** (1991) 1819.

[70] A. Puig, *The LHCb trigger in 2011 and 2012*, LHCb-PUB-2014-046.

[71] LHCb collaboration, R. Aaij *et al.*, *Measurement of b hadron production fractions in 7 TeV pp collisions*, Phys. Rev. **D85** (2012) 032008, arXiv:1111.2357.

[72] LHCb collaboration, R. Aaij *et al.*, *Measurement of the fragmentation fraction ratio f_s/f_d and its dependence on B meson kinematics*, JHEP **04** (2013) 001, arXiv:1301.5286, f_s/f_d value updated in LHCb-CONF-2013-011.

[73] LHCb collaboration, R. Aaij *et al.*, *Measurement of the semileptonic CP asymmetry in B^0–$\overline{B}^0$ mixing*, Phys. Rev. Lett. **114** (2015) 041601, arXiv:1409.8586.

[74] LHCb collaboration, R. Aaij *et al.*, *A precise measurement of the B^0 meson oscillation frequency*, Eur. Phys. J. **C76** (2016) 412, arXiv:1604.03475.

[75] LHCb collaboration, R. Aaij *et al.*, *Neural-network-based same side kaon tagging algorithm calibrated with $B_s^0 \to D_s^- \pi^+$ and $B_{s2}^*(5840)^0 \to B^+ K^-$ decays*, JINST **11** (2016) P05010, arXiv:1602.07252.

[76] LHCb collaboration, R. Aaij *et al.*, *Observation of the decay $B_c^+ \to B_s^0 \pi^+$*, Phys. Rev. Lett. **111** (2013) 181801, arXiv:1308.4544.

[77] Aaij, R. *et al.*, *Flavour tagged time-dependent angular analysis of $B_s^0 \to J/\psi K^+ K^-$ decays in the low $K^+ K^-$ mass range*, LHCb-ANA-2014-039.

[78] Marino, P. and Morello, M. J. and Punzi, G., *Measurement of time-dependent CP-violating asymmetries in $D^0 \to K^+ K^-$ and $D^0 \to \pi^+ \pi^-$ decays*, LHCb-ANA-2016-010.

[79] LHCb collaboration, R. Aaij *et al.*, *Effective lifetime measurements in the $B_s^0 \to K^+ K^-$, $B^0 \to K^+ \pi^-$ and $B_s^0 \to \pi^+ K^-$ decays*, Phys. Lett. **B736** (2014) 446, arXiv:1406.7204.

Bibliography

[80] Heavy Flavor Averaging Group, Y. Amhis *et al.*, *Averages of b-hadron, c-hadron, and τ-lepton properties as of summer 2016*, Eur. Phys. J. **C77** (2017), no. 12 895, `arXiv:1612.07233`, updated results and plots available at `http://www.slac.stanford.edu/xorg/hflav/`.

[81] M. Artuso, G. Borissov, and A. Lenz, *CP violation in the B_s^0 system*, Rev. Mod. Phys. **88** (2016), no. 4 045002, `arXiv:1511.09466`, Eq. 89.

[82] FOCUS collaboration, J. M. Link *et al.*, *A measurement of the D_s^+ lifetime*, Phys. Rev. Lett. **95** (2005) 052003, `arXiv:hep-ex/0504056`.

[83] FOCUS collaboration, J. M. Link *et al.*, *New measurements of the D^0 and D^+ lifetimes*, Phys. Lett. **B537** (2002) 192, `arXiv:hep-ex/0203037`.

[84] LHCb collaboration, R. Aaij *et al.*, *Measurement of the b-quark production cross-section in 7 and 13 TeV pp collisions*, Phys. Rev. Lett. **118** (2017) 052002, `arXiv:1612.05140`, [Erratum: Phys. Rev. Lett. 119, no.16, 169901(2017)].

Brice Maurin

Av. de Valmont 14
1010 Lausanne
✆ *079 712 67 92*
✉ *brice.maurin@alumni.epfl.ch*
16.10.1990, Swiss citizen

Education

2014 – 2018 **Ph.D. in Physics**, *EPFL, École Polytechnique Fédérale de Lausanne*, Thesis in particle physics under the supervision of Prof. T. Nakada.
Title: *Measurement of lifetimes for heavy flavour mesons using semileptonic decays at LHCb.*

2012 – 2014 **Master of Science MSc in Physics**, *EPFL, École Polytechnique Fédérale de Lausanne*, Master thesis in particle physics.
Studies on the LHCb trigger and lifetime measurements.

2009 – 2012 **Bachelor of Science BSc in Physics**, *EPFL, École Polytechnique Fédérale de Lausanne.*

2006 – 2009 **High school degree (Maturité Gymnasiale)**, *Lycée Denis-de-Rougemont*, Neuchâtel.
Diploma in physics and applied mathematics, bilingual French/English, with Mention.

Experience

2014 – 2018 **Ph.D. student**, *EPFL, École Polytechnique Fédérale de Lausanne.*
– Worked on a full analysis which allowed improvements upon previous determinations of lifetimes measurements. Results are published in a major journal (PRL).
– Did R&D and characterisation of SiPM detectors for the future upgrade of the LHCb detector.
– Taught physics to Bachelor and Master students and worked on exam corrections (7 semesters).

2011 – 2013 **Student Assistant**, *EPFL, École Polytechnique Fédérale de Lausanne.*
– Tutored students in general physics and laboratory work
– Wrote documentation for statistical physics course.

2013 **Support Worker**, *Philip Morris Products SA*, Neuchâtel, Summer Job.
Did studies on different filling and capping technologies for small containers.

Since 2003 **Private tutor**.
In mathematics and physics, university level and below.

Associations

2017 – Present **Secretary**, *Swiss Federation of Mathematical Games*, Switzerland.
Organisation of the yearly championship of mathematical games in Switzerland (12000 participants).

2012 – 2017 **Event Manager**, *PolyJapan*, EPFL, Lausanne, Switzerland.
Organisation of events on Japanese culture. In charge of the VIPs, performers, exhibitors and screenings for Japan Impact (8000 visitors).

2009 – 2013 **Member of the association, treasurer (2011–2012), Vice-President (2012–2013)**, *Les Irrotationnels*, EPFL, Lausanne, Switzerland.
Association of the physics students of EPFL. Organisation of events and conferences for other students.

2007– 2010 **Active member**, *Young Parliament of Neuchâtel*, Neuchâtel, Switzerland.
Development of projects in the canton of Neuchâtel.

Computer Skills

Languages	C/C++, Python, Visual Basic, HTML
Analysis	Matlab, CERN tools (ROOT, Roofit, MINUIT)
Systems	Linux (Ubuntu, Fedora), Windows
Software	Office, LibreOffice, LaTeX

Schools and conferences

PSI Zuoz summer school 2016 - Exothiggs, *Zuoz, Switzerland*, August 2016.

SPS - ÖPG 2017, *Geneva, Switzerland*, August 2017.
– Talk titled: *Semileptonic decays at LHCb.*

LLWI 2017, *Lake Louise, Canada*, February 2017.
– Talk titled: *Semileptonic B decays at LHCb.*

CHIPP/SPS 2016, *Lugano, Switzerland*, August 2016.
– Talk titled: B_s^0 *lifetime measurement using semileptonic decays at the LHCb experiment.*

Scientific publications

Co-author for over 160 publications as part of the LHCb collaboration. Full list: `bit.do/bricehep`

LHCb collaboration, R. Aaij *et al.*, *Measurement of B_s^0 and D_s^- meson lifetimes*, Phys. Rev. Letter. **119** (2017), 101801, arXiv:1705.03475.

Languages

French	**Native language**
English	**C1$^+$ level, Cambridge First Certificate**
German	**B1 level**

Interests

Japanese culture, fantastic literature, recreational mathematics.